

C

Internal Report
DESY F35D-97-12
November 1997

Grat ausgeben



Inelastic Photoproduction of J/ψ Mesons at HERA

by

L.-W. Hung

Eigentum der	DESY	Bibliothek
Property of		library
Zugang:	19. JAN. 1998	
Accessions:		
Leihfrist:	7	Tage
Loan period:		days

DESY behält sich alle Rechte für den Fall der Schutzrechtserteilung und für die wirtschaftliche Verwertung der in diesem Bericht enthaltenen Informationen vor.

DESY reserves all rights for commercial use of information included in this report, especially in case of filing application for or grant of patents.

**"Die Verantwortung für den Inhalt dieses
Internen Berichtes liegt ausschließlich beim Verfasser"**

**Inelastic Photoproduction of J/ψ mesons
at HERA**

by

Ling-Wai Hung ✓

Department of Physics, McGill University
Montreal, Quebec

April 1997

A Thesis submitted to the
Faculty of Graduate Studies and Research
in partial fulfillment of the requirements for the degree of
Doctor of Philosophy

© Ling-Wai Hung, 1997

**Inelastic Photoproduction of J/ψ mesons
at HERA**

by

Ling-Wai Hung
Department of Physics, McGill University
Montreal, Quebec
April 1997

A Thesis submitted to the
Faculty of Graduate Studies and Research
in partial fulfillment of the requirements for the degree of
Doctor of Philosophy

© Ling-Wai Hung, 1997

Abstract

A measurement of the inclusive inelastic J/ψ photoproduction cross section using the ZEUS detector at HERA is described. The cross section of the reaction $e^+p \rightarrow e^+J/\psi X$ was determined for events with an inelasticity, z , less than 0.9, where z is the ratio of the energy of the outgoing J/ψ to the energy of the incoming photon in the proton's rest frame. The measurement was performed in the photon-proton centre of mass energy range $110 < W_{\gamma p} < 160$ GeV using the decay channel $J/\psi \rightarrow e^+e^-$. The measurements compare favourably with recent NLO calculations using the colour singlet model.

Résumé

Une mesure de la section efficace de la photoproduction du J/ψ en utilisant le détecteur ZEUS à HERA est décrite. La section efficace de la réaction $e^+p \rightarrow e^+J/\psi X$ a été déterminée pour les événements avec une inélasticité, z , plus petit que 0.9, où z est la proportion d'énergie du J/ψ par rapport à l'énergie du photon dans le référentiel du proton. La mesure a été effectuée dans la gamme d'énergie de centre de masse photon-proton entre $110 < W_{\gamma p} < 160$ GeV en utilisant la désintégration $J/\psi \rightarrow e^+e^-$. Ces mesures sont en accord avec les calculs théoriques aux deuxième ordre de QCD du "colour singlet model".

Contents

Abstract	iii
List of Figures	vii
List of Tables	xiv
Acknowledgements	xv
Personal contribution to the ZEUS experiment	xvi
Foreword	xix
1 Introduction	1
1.1 Background	1
1.2 Lepton-Hadron Scattering	4
1.3 The J/ψ particle	5
1.3.1 Properties of the J/ψ	6
1.3.2 Why do we still care about the J/ψ	7
1.4 Production Mechanisms of the J/ψ	8
1.4.1 Elastic and Diffractive	9
1.4.2 Inelastic J/ψ Production	10
2 The Experiment	19
2.1 HERA (Hadron Elektron Ring Anlage)	19
2.2 The ZEUS Detector	25
2.2.1 Inner Tracking Detectors	26
2.2.2 Calorimetry	30
2.2.3 The ZEUS Calorimeter	33
2.2.4 Muon Detectors	35
2.2.5 Luminosity Monitor	35
2.2.6 Other Detectors	36
2.3 Data Acquisition	37
2.3.1 Trigger	37
2.3.2 The First Level Trigger	38
2.3.3 The Second Level Trigger	38

CONTENTS	v
2.3.4 The Third Level Trigger	39
2.3.5 Reconstruction	39
2.4 Data Set	41
2.5 Track Reconstruction	41
2.5.1 Determination of dE/dx	42
2.6 Calorimeter Reconstruction	46
2.6.1 Islands	47
2.7 Analysis environment	47
3 Monte Carlo	50
3.1 Event Generators	50
3.1.1 Inelastic (Direct Photon)	53
3.1.2 Resolved Photon	54
3.1.3 Proton Dissociation	55
3.2 ZEUS Monte Carlo	56
3.2.1 FUNNEL	57
3.3 Requirements	57
4 Data Selection	59
4.1 The Trigger Selection	59
4.1.1 First Level Trigger	59
4.1.2 The Second Level Trigger	61
4.1.3 Third Level Trigger	63
4.2 Offline Selection	66
4.2.1 Selecting Electrons from J/ψ Decay	66
4.3 Kinematics	70
4.4 Signals	75
4.4.1 Bremsstrahlung fit	75
4.4.2 Final Sample	78
5 Analysis	80
5.1 Distributions and Comparison to Monte Carlo	81
5.1.1 Proton Dissociation Contamination	84
5.2 Acceptance Calculation	87
5.2.1 dE/dx Efficiency	94
5.2.2 Calorimeter Thresholds	94
5.3 Systematic Studies	97
5.3.1 Additional Checks	100
5.4 Cross section	102
5.4.1 Photoproduction Cross section	103
6 Summary and Outlook	106
A Using dE/dx	108

CONTENTS	vi
B Glossary	119
References	122

List of Figures

1.1	Diagrams of deep inelastic scattering (left) of a photon and a quark from the proton and boson gluon fusion (right) of a photon and a gluon	5
1.2	a) An otherwise preferred decay mode of the J/ψ which is not allowed because the mass ($3097 \text{ MeV}/c^2$) is insufficient to produce two D mesons ($1870 \text{ MeV}/c^2$ each). b) An example of a hadronic decay mode of the J/ψ through a three gluon exchange. c) Electromagnetic decay of the J/ψ to an e^+e^- pair through a single virtual photon.	7
1.3	Diagrams for elastic photoproduction of J/ψ (left) and diffractive photoproduction of J/ψ through proton dissociation (right).	9
1.4	The measurements [22, 23, 24] of the cross section for diffractive J/ψ photoproduction compared with the full perturbative QCD prediction obtained with three recent structure function sets. Although the predictions have a significant normalization uncertainty, the shape of the cross section clearly favours MRS(A') over GRV(94).	10
1.5	Leading order diagram for inelastic J/ψ photoproduction via the colour singlet model.	12
1.6	Comparison of the sensitivity of the NLO calculations of the inelastic J/ψ photoproduction cross section to different gluon distributions for two different kinematic ranges [35].	14
1.7	The predicted J/ψ energy distribution $d\sigma/dz$ integrated over $p_t > 1 \text{ GeV}$ for $W_{\gamma p} = 100 \text{ GeV}$	16
1.8	J/ψ production through a resolved photon	17
2.1	Layout of the HERA ring.	20
2.2	Layout of the HERA injection system.	21
2.3	Integrated Luminosity in 1994. The upper curve shows the integrated luminosity delivered by HERA to the ZEUS interaction region over the course of the year. The lower curve shows the integrated amount of luminosity actually recorded by ZEUS.	24
2.4	Layout of the central region of the ZEUS detector with one quadrant removed.	27
2.5	View of a CTD octant. The thick dots are the sense wires.	29
2.6	Overview of the ZEUS trigger system.	40

2.7	The dE/dx of tracks versus momentum from run 10037. The tracks were required to have at least 35 hits contributing to the truncated mean. The momentum dependence predicted by the Bethe-Bloch formula, with an arbitrary scale, is overlaid for the pion, kaon, and proton bands. The bands are clearly distinguishable. The electron band is not visible, but would lie around 75 ADC counts.	43
2.8	dE/dx distribution, scaled by the pion mean dE/dx value, of the individual hits belonging to electron tracks. The sample was taken from elastic $J/\psi \rightarrow e^+e^-$ events with tracks in the polar angle region $1.2 < \theta < 1.9$ rad. The shape is typical of a Landau distribution which has a tail towards higher values. The peak around 4 originates from saturated hits.	44
2.9	Value of the mean dE/dx (in units of ADC counts) for pions with momentum between 0.3 and 0.4 GeV/c versus run number. The large jump in the mean dE/dx around run number 9400 is due to the nominal settings of the CTD high voltage being raised.	45
2.10	An example of the island clustering algorithm. The dots denote towers which are island seeds. The trail of pointers to the neighbouring tower with the most energy is shown by the arrows. The thick black lines delimit the boundary of an island.	48
3.1	Distributions of kinematic quantities for events generated by HERWIG using the colour-singlet model. A cut of $z < 0.95$ was imposed.	53
3.2	Distributions of events generated by EPJPSI using the colour singlet model.	54
3.3	Distribution of events generated by EPJPSI with the resolved photon process $gg \rightarrow J/\psi g$	55
3.4	Distribution of proton dissociative events generated by EPSOFT with the cross section falling as $e^{- t }$ and $M_X^{2.25} c^2$ in the W range $20 < W < 225 \text{ GeV}$	56
4.1	The CAL timing distribution of events at the SLT. Events (beam-gas) outside the box (black dots) are rejected by the timing cuts. The cluster of good events centred around a time of (0,0) ns is clearly separated from beam-gas events. However, some beam-gas events are still accepted (in the bottom right corner of the box).	62
4.2	Distributions at the SLT for paasthrough (unbiased) events and for inelastic $J/\psi \rightarrow e^+e^-$ MC events from HERWIG (hatched histogram). The HERWIG events were required to pass bit 43 at the FLT and have the decay electrons within the CTD.	64
4.3	TLT track multiplicity of inelastic colour singlet $J/\psi \rightarrow e^+e^-$ events generated by HERWIG with $50 < W_{\gamma p} < 250 \text{ GeV}$	65
4.4	The z -vertex distribution of events selected by the J/ψ TLT filter in 1994. A Gaussian fit is overlaid. The bump near $z = 70 \text{ cm}$ is due to the presence of a satellite proton bunch caused by the radiofrequency cavity system.	68

- 4.5 A scatter plot of the p_t correlation between the two candidate electron tracks for (left) data after preselection and (right) HERWIG J/ψ MC events. The two plots are shown with arbitrary normalization. 68
- 4.6 Distributions of variables used to find electrons. The solid line is from candidates from data after preselection, the dashed line is from true electrons from HERWIG MC events and the dots are from electrons from elastic J/ψ events in the data. Electrons from elastic $J/\psi \rightarrow e^+e^-$ events are not expected to agree perfectly those from inelastic J/ψ Monte Carlo, but do give an indication of the suitability of the cuts. e.g. in a) the electrons from the elastic J/ψ sample have a relatively smaller radius than those from inelastic processes because they are more often in BCAL which has a smaller EMC cell size than RCAL. In d) the lower E_{island}/P_{track} values are expected because electrons from elastic J/ψ decays have on average less energy than their counterparts from inelastic J/ψ decays. The peak is at less than one because energy is lost in the inactive material between the interaction region and the calorimeter. 69
- 4.7 Mass distribution of $J/\psi \rightarrow e^+e^-$ candidates after a) the preselection, b) p_t of the electron tracks > 0.8 GeV/c, c) electron island radius < 16 cm, d) $E_{emc}/E > 0.95$ for electron islands, e) track-island distance < 15 cm, f) $|\eta|$ of electron tracks < 1.5 , g) Energy in forward cone > 1 GeV, h) $z_{rec} > 0.48$, i) dE/dx of electron tracks > 1.25 times pion mean, j) $105 < W_{rec} < 149$ GeV, k) $z_{rec} < 0.9$, l) $p_t(J/\psi) > 1$ GeV/c, m) $z_{rec} < 0.85$. The cuts most effective in reducing the background are the lower limit on z and the dE/dx cut. 71
- 4.8 A picture of a typical $J/\psi \rightarrow e^+e^-$ event. The display is divided into three parts. The larger one gives a side view of the CAL plus inner detectors. FCAL is on the left and the two rightmost energy deposits are from the decay electrons. The other two views are of the calorimeter transverse energy deposits on a $\eta - \phi$ grid and of an axial view of the CTD and BCAL. Note: the display program automatically assumes that the electron-like island with the largest transverse energy originates from the scattered electron of a DIS event. Since this was not the case, the Q^2 value printed along with other event information at the top of the display is not correct. 72
- 4.9 z reconstruction of the J/ψ from the HERWIG Monte Carlo: (a) z reconstructed versus z generated (b) $(z_{rec} - z_{gen}) / z_{gen}$ for $0.34 < z_{gen} < 0.46$ (c) $(z_{rec} - z_{gen}) / z_{gen}$ for $0.78 < z_{gen} < 0.82$. The fits shown are Gaussian. 74
- 4.10 W reconstruction of the J/ψ from the HERWIG Monte Carlo: (a) W reconstructed versus W generated (b) $(W_{rec} - W_{gen}) / W_{gen}$ for $100 < W_{gen} < 120$ GeV (c) $(W_{rec} - W_{gen}) / W_{gen}$ for $150 < W_{gen} < 170$ GeV. The fits shown are Gaussian. 74
- 4.11 W_{rec} versus the mass of the J/ψ candidates. The horizontal lines are at $W_{rec} = 105$ GeV and at $W_{rec} = 149$ GeV. 75

- 4.12 p_t resolution of the J/ψ 's: a) p_t of the J/ψ reconstructed versus the generated p_t b) $(p_t \text{ reconstructed} - p_t \text{ generated}) / p_t \text{ generated}$ c) average of $((p_t \text{ reconstructed} - p_t \text{ generated}) / p_t \text{ generated})$ versus $p_t \text{ generated}$. The vertical error bars indicate the size of the spread. 76
- 4.13 Results from the bremsstrahlung fit procedure applied to Monte Carlo samples each with 50 true J/ψ events plus 10 randomly distributed background events all in the mass range between 2.4 and 3.6 GeV/c². a) Number of Signal Events, b) Width of Mass distribution, c) Mass of J/ψ as determined by the fit. 77
- 4.14 Mass distribution of inelastic $J/\psi \rightarrow e^+e^-$ candidates with $0.48 < z_{rec} < 0.9$. The full line shows the result of the bremsstrahlung fit plus background. The dashed line shows the size of the background. 78
- 4.15 Mass distribution of inelastic $J/\psi \rightarrow e^+e^-$ candidates after all cuts and with $0.48 < z_{rec} < 0.9$ and $p_t(J/\psi) > 1$ GeV/c. The full line shows the result of the bremsstrahlung fit plus background. The dashed line shows the size of the background. 79
- 4.16 Mass distribution of inelastic $J/\psi \rightarrow e^+e^-$ candidates after all cuts and with $0.48 < z_{rec} < 0.85$ and $p_t(J/\psi) > 1$ GeV/c. The full line shows the result of the bremsstrahlung fit plus background. The dashed line shows the size of the background. 79
- 5.1 Comparison of distributions from data and inelastic colour singlet Monte Carlo. The data, taken from the final sample with $0.48 < z < 0.9$ and $p_t > 1$ GeV/c are represented by the filled circles. The predictions from the HERWIG MC are represented by the solid line histograms, and those from EPJPSI by the dashed line histograms. The plots shown are a) γp centre of mass energy W , b) Inelasticity z , c) J/ψ transverse momentum, d) Number of tracks associated with the vertex, e) Number of tracks reconstructed by the TLT and f) Polar angle of the decay electrons in the laboratory frame. 82
- 5.2 Comparison of distributions from data and inelastic colour singlet Monte Carlo. The data, taken from the final sample with $0.48 < z < 0.9$ and $p_t > 1$ GeV/c are represented by the filled circles. The predictions from the HERWIG MC are represented by the solid histograms, and those from EPJPSI by the dashed histograms. The plots shown are a) Polar angle of J/ψ candidate in the laboratory frame, b) Energy deposited in FCAL, c) Energy in BCAL, d) Energy in RCAL, e) Energy in BCAL discounting the deposits from the decay electrons and f) Same as in e) but for RCAL. 83
- 5.3 Multiplicity of tracks associated with the vertex for candidate J/ψ events with $0.48 < z_{rec} < 0.9$ for data and MC. 84
- 5.4 Mass distribution of elastic (right) and of inelastic $J/\psi \rightarrow e^+e^-$ candidates with $z > 0.48$ (left). The full line shows the result of the bremsstrahlung fit plus background. The dashed line shows the size of the background. 85

- 5.5 The z_{rec} and p_t distributions of the J/ψ candidates for $z_{rec} > 0.48$ are compared with inelastic MC distributions from HERWIG (solid line), EPJPSI (dashed line) and proton dissociation distributions from EPSOFT with the cross section falling as $e^{-|t|}$ and $M_X^{-2.25}$ (dotted line). 86
- 5.6 χ^2 values from the comparison of the data distributions for z and p_t with a Monte Carlo mixture of either HERWIG+EPSOFT or EPJPSI+EPSOFT. The solid and dashed lines are from HERWIG+EPSOFT mixtures. The cross section dependence of EPSOFT on t and M_X were varied; the former had $b = 1$, $n = -2.25$; the latter had $b = 0.6$, $n = -2.0$ and its $E - P_z$ values shifted by +70 MeV to simulate extra noise in the calorimeter. The corresponding mixtures with EPJPSI instead of HERWIG are represented by the dotted and dot-dashed lines respectively. 87
- 5.7 χ^2 values from the combined comparison of the data distributions for z and p_t with Monte Carlo mixtures of HERWIG+EPSOFT and EPJPSI+EPSOFT. The solid and dashed lines are from HERWIG+EPSOFT mixtures. The cross section dependence of EPSOFT on t and M_X were varied; the former had $b = 1$, $n = -2.25$; the latter had $b = 0.6$, $n = -2.0$ and its $E - P_z$ values shifted by +70 MeV. The corresponding mixtures with EPJPSI instead of HERWIG are represented by the dotted and dot-dashed lines. Lines showing the χ^2 values for 65% and 90% confidence are also shown. 88
- 5.8 The z_{rec} and p_t distributions of the J/ψ candidates for $z_{rec} > 0.48$ are compared with MC distributions from the combination of HERWIG (72%), plus EPSOFT (28%) whose cross section falls as $e^{-|t|}$ and $M_X^{-2.25}$ 89
- 5.9 The selection efficiencies (excluding dE/dx cut) dependence on the kinematics of J/ψ production according to the Monte Carlos. The open circles representing EPJPSI are offset slightly to the right of their proper positions. The generated values for W , p_t and z were used. Efficiencies are given in a) for $0.4 < z < 0.9$, $p_t > 1$ GeV/c; b) $0.4 < z < 0.9$, $110 < W < 160$ GeV, and c) $110 < W < 160$ GeV, $p_t > 1$ GeV/c. The dE/dx cuts were not used. 92
- 5.10 Efficiency of the trigger and track angle cuts applied to the HERWIG J/ψ events at the generator level. The full line represents the efficiency of the FLT bit 43 with W . The dashed line is with the SLT bit HPL03 added, the dotted after applying an η cut on the decay electron tracks and the dot-dashed line also includes the TLT J/ψ bit. 93
- 5.11 Efficiency of requiring the dE/dx of an electron candidate to be greater than 1.25 times the pion mean value versus the polar angle of the track. 94
- 5.12 The online CFLT threshold efficiencies for a) EREMC > 2.0 GeV and b) EBEMC > 3.4 GeV triggers. The energies along the horizontal axes are the offline reconstructed ZGANAs energies. 96

- 5.13 $E - P_z$ distribution of the calorimeter cells from elastic J/ψ events after excluding the cells associated with the decay leptons. The remaining cells should correspond to the contribution from the calorimeter noise. The plots are shown for data and Monte Carlo events from the DIPSI [72] generator (a MC generator for elastic J/ψ events). 100
- 5.14 Estimates of the systematic uncertainties associated with the cross section measurements. The selection cuts were slightly modified and the difference in the resulting cross section are plotted here. Cuts which could be construed as being correlated to some degree with one another are grouped together; the largest percent difference (shown on the line describing the category) is used for the size of the uncertainty pertaining to that group of cuts. 101
- 5.15 Total cross section for inelastic (direct photon) J/ψ production for $z < 0.9$ (upper) and $z < 0.8$, $p_t > 1$ GeV/c (lower). The curves represent NLO pQCD calculations [33] for different parton distributions. They also contain a 15% correction to take into account background from inelastic ψ' production. The inner error bars of the electron data show the statistical errors and the outer error bars also include the systematic certainties. The ZEUS muon data [75] show only statistical errors, whereas for the H1 data [74] the error bars represent the combined statistical and systematic errors. Data from lower energy experiments, NA14[30] and FTFS[24] are also shown (error bars represent combined statistical and systematic uncertainties). 105
- A.1 Comparison of the dE/dx measurement for elastic J/ψ electrons from Monte Carlo (left) and data (right). The selection of the events is described in the text. In addition, only tracks which used at least 30 hits in their truncated mean were used. The resolution was determined by applying a Gaussian fit. 109
- A.2 Mass distribution of an elastic $J/\psi \rightarrow e^+e^-$ sample. The results of a fit using a bremsstrahlung function (see Section 4.4.1) plus a linear background is shown by a solid line; the linear background is illustrated by the dotted line. The histogram shows the estimated contribution from the Bethe-Heitler process which completely accounts for the background. 110
- A.3 Distribution of DISTB for conversion candidates. 112
- A.4 Point of conversion in the x-y plane for candidates with a) $0 < DISTB < 1$ and b) $-25 < DISTB < 0$. The offset of the VXD with respect to the beamline can clearly be seen. The photons convert primarily in the walls of the beampipe (inner ring) and the CTD (outer ring). Radial distance from the origin of the points of conversion for candidates with c) $0 < DISTB < 1$ and d) $-25 < DISTB < 0$ 113

A.5	The dE/dx distribution for tracks from conversion electrons candidates with $p_t > 0.8$ GeV/c and having between 36 and 40 hits used in the truncated mean. The left plot shows the distributions for the signal region $0 < \text{DISTB} < 1$ (unfilled histogram) and background region $-20 < \text{DISTB} < 0$, scaled by 1/20 (filled histogram). The right plot shows the result after the background has been subtracted from the signal distribution. A Gaussian fit is overlaid in both plots.	114
A.6	Mean dE/dx versus polar track angle for electrons from a) the elastic J/ψ sample and b) the conversion sample. The solid circles are for tracks with no restriction on the number of saturated hits. The open circles are for tracks with no saturated hits used in the calculation of the truncated mean.	115
A.7	Fit to the mean dE/dx as a function of $ \cos\theta $. Only tracks which used no saturated hits in determining the truncated mean are included. The fit was applied to the elastic J/ψ data points.	116
A.8	Mean dE/dx after correction versus polar angle for electrons from a) elastic J/ψ and b) conversion candidates. The solid circles are for tracks with no restriction on the number of saturated hits. The open circles are for tracks with no saturated hits used in the calculation of the truncated mean.	117
A.9	Properties of conversion electrons.	118

List of Tables

2.1	Parameters of the HERA collider, design and in 1994.	23
2.2	R.M.S. width of the noise in the CAL measured at the end of the 1994 running period.	46
4.1	Selection of 94 data.	70
5.1	The number of proton dissociation events expected to have migrated into the measurement region as determined by extrapolating from an elastic J/ψ sample and by comparing the z and p_t distributions. The values were determined by taking the average of the two extremes of the EPSOFT Monte Carlo, one with $b = 0.6$, $n = -2.0$ and shifting $E - P_z$ by 70 MeV, the other with $b = 1.4$, $n = -2.5$. The errors given are systematic; the first is determined by varying the t and M_X dependence of the EPSOFT Monte Carlo and the second is from the uncertainty in the proton dissociation fraction. The statistical errors on the values are 20% for the first column and 16% for the second, in both cases coming from the bremsstrahlung fits of Figure 5.4.	89
5.2	Acceptances, purities and efficiencies for $110 < W < 160$ GeV as determined by Monte Carlo.	93
5.3	Calculation of the inelastic J/ψ cross section for three different z and p_t ranges. The first error is statistical; the second is systematic. The uncertainty in W_{ep} is statistical only.	104

Attempting to obtain a PhD was much more than a pure scholastic endeavour. It also required adapting to a very different environment while living in Germany. Those six years in Germany would have been much more difficult without the support of the closely knit group of Canadians (plus honorary Canadians) at DESY. In particular, I would like to thank my office mates at DESY, Laurel, Rainer, Marc, Michael and Andreas plus the other fellow students and postdocs, Burkhard, Miloš, Richard, Cortney, Pat, Peter, Mohsen, Dave, Frédéric, Joo, Larry, Jon, Frank, Mike, Raphael and Ali, who, for the most part, have become dependable friends over the years. I should not forget my office mates in Montreal, mighty Claude, Rainer (again), Shem, Kostas and Marko, who made me feel welcomed when I came back to finish my thesis. I would also like to thank my colleagues at DESY, Riccardo, Alessandro, Luca, Tim, Kensuke, Ming, Peppe and Jit Ning, for valuable discussions while working on this analysis. I also benefited from discussions with Michael Krämer who explained some aspects of inelastic J/ψ production to me. I am grateful to David Hanna, my supervisor, for his guidance and his patience. I owe much to my parents for their generous and unconditional support which made this all possible. Special thanks go to Frédéric, Rainer and David for giving my thesis a critical reading. And to Charline whose faith and pride in me never wavered, thanks for everything.

Personal contributions to the ZEUS experiment

I first joined the ZEUS experiment in 1990 while I was still in the masters program. During part of the summer I participated in the assembly of the ZEUS calorimeter modules in Markham. Later, in the fall, I went to DESY where I joined the calorimeter group and over a period of several months helped conduct and analyse ^{60}Co source scans of the calorimeter modules as a quality control check before their final installation. I also wrote a Monte Carlo simulation of the source scanning procedure using the EGS4 package.

When I started my PhD on ZEUS in the fall of 1991, we were still preparing for the first ep collisions which were scheduled to take place the following year. I joined the magnet group which was responsible for operating the superconducting solenoid which provides the magnetic field for the central trackers. As we were still gaining experience with the magnet and its cryogenic system, constant supervision was required during the cooling and operation of the magnet.

In 1992 I returned to the calorimeter group and was given the responsibility for writing the Calorimeter Status Manager (CSM), software which obtains lists of individual bad calorimeter channels from the data quality monitoring processes and groups them into a much shorter list of hardware components. The CSM sends every few minutes an updated list of these hardware components along with the calorimeter's overall status to the ZEUS slow control system. In this way problems with the calorimeter could be communicated quickly to the shift crew and action taken. I would maintain and update this code for the next four years. In addition, during the 1992 running period, I frequently participated in shifts in which I monitored the

data quality and safety of the calorimeter. I conducted regular calibration runs which included the laser calibration system. During the analysis of these runs, I would often spot bad calorimeter channels. I would then attempt to pinpoint the reason for the bad channels and repair them if possible. Also during 1992, I was a founding member of the FUNNEL (the ZEUS Monte Carlo production utility) group and became their first operator, which meant I processed the Monte Carlo physics events through the FUNNEL system to simulate the response to the ZEUS detector to these events. All of the Monte Carlo used by ZEUS would eventually be produced through the FUNNEL system.

In 1993 I was the Monte Carlo representative in the Hard Photoproduction group. This required coordinating the production of generator-level Monte Carlo events and their submission into FUNNEL. Often I had to reprocess them again through the ZEUS trigger and reconstruction software programs to obtain different running configurations.

During the yearly running periods, except for 1994, I did my share of shifts in the ZEUS control room, either as safety officer or deputy shift leader. The safety officers were responsible for the safe operation of the ZEUS detector. They were required to make rounds about the experiment checking if everything was performing within nominal parameters. The deputy too had a check list of duties to perform, primarily dealing with data quality monitoring. In 1994 I did monthly sets of online operator shifts, where I was responsible for the ZEUS data acquisition. If a problem occurred, I would have to localise it and solve it as quickly as possible so that ZEUS could continue to take data. Often I would have to restart processes on various computers, and if all else failed, would contact the component expert responsible.

From 1994 on, I concentrated on the analysis of the inelastic production of J/ψ 's by tagging the e^+e^- decay mode. Working independently, I developed my own set of analysis cuts. The results of the analysis on the 1993 data (muons and electrons) were shown at Photon '95 in Sheffield, U.K. There, I provided the primary analysis for the electron decay channel. It was the first publicly shown ZEUS data which used

dE/dx information. My investigations contributed to the understanding the dE/dx response of the CTD. The preliminary 1994 ZEUS results, for which I provided the primary electron analysis, have been shown at various international conferences. A paper is currently under preparation with the final results from the 1994 data where I provided the second analysis for the electron channel.

Foreword

The direct photoproduction of the heavy quarks can be calculated using perturbative QCD and is sensitive to the gluon distribution of the nucleon. However, the transition from the quark-antiquark pair to a bound state involves nonperturbative physics. Different models describing this process have appeared in the literature, the most popular being the “colour singlet model”. The measurement of the production cross section of heavy quark bound states (such as a J/ψ) in γp collisions can distinguish between these models and also provide information on the gluon density of the nucleon.

This thesis presents an analysis of the 1994 data taken with the ZEUS detector at the HERA ep collider. The *inelastic* photoproduction cross section of J/ψ mesons is determined by tagging the e^+e^- coming from the decay of the J/ψ .

The organization of this thesis is presented here. In the first chapter, after a very brief introduction to particle physics and in particular QCD, we present an overview of the J/ψ and theories regarding its production mechanisms. In particular, the main model explaining inelastic J/ψ photoproduction, the colour singlet model, will be described in detail. Possible sources of signal background will be discussed, from diffractive proton dissociation to resolved photoproduction. The HERA collider and the ZEUS detector are described in chapter two, with an emphasis placed on the main components used in this analysis: the calorimeter and the central tracking detector. This is followed by a brief diversion into the realm of Monte Carlo simulation in chapter three where the programs used to model the production mechanisms of the J/ψ which contribute to the signal are described. In chapter four we explain the selection procedure used to extract a clean sample of a few dozen inelastic J/ψ events decaying into an e^+e^- pair from the many millions of events recorded by ZEUS. The analysis of the data is presented in chapter five, including comparisons with the Monte Carlo distributions. In turn the production cross sections are determined and an estimate of the systematic uncertainties associated with the measurement are

given. These results are compared with recent theoretical calculations. Finally in chapter six we discuss the significance of the results in the perspective of theories introduced in chapter one. An appendix follows which describes the determination of the efficiency of the dE/dx cut on the electron tracks which was a crucial step in isolating true J/ψ events. A glossary is also provided to explain recurring acronyms and specialized terminology.

Chapter 1

Introduction

1.1 Background

Particle physics concerns itself with the study of the properties of the fundamental constituents of matter and their interactions with each other. According to our current understanding, called the *Standard Model*, matter is composed of spin one half particles (*fermions*) divided into quarks and leptons. They interact through four different forces, the electromagnetic, strong, weak and gravitational, by the exchange of integral spin particles called *bosons*. Of the four forces, the electromagnetic force, whose exchange particle is the photon, is understood the best. Its foundations were first established through Maxwell's equations in the 19th century and was incorporated by the late 1940's in a quantum gauge field theory called *Quantum Electrodynamics* (QED). In the late 1960's Weinberg, Salam and Glashow showed how the electromagnetic and weak forces were aspects of the same, unified force [1]. The quantum field formalism was later applied to the strong interaction, which led to the theory of *Quantum Chromodynamics* (QCD). Gravitation, however, is not included in the Standard Model, which nevertheless does not pose a dilemma from an experimental point of view as it is much too weak to affect elementary particles at the energy scales which can now be probed.

In the Standard Model there are three pairs each of quarks (u, d, c, s, t, b) and

leptons ($e, \mu, \tau, \nu_e, \nu_\mu, \nu_\tau$), plus their corresponding antiparticles. Quarks have yet to be seen alone. They are instead found grouped in bound states (*hadrons*), which are formed either from $q\bar{q}$ pairs, where q signifies a quark and \bar{q} an antiquark, or qqq , $\bar{q}\bar{q}\bar{q}$ triplets. The former are called *mesons*, the latter *baryons*. The quantum number *colour* was introduced for quarks to explain the existence of the Δ^{++} baryon which is made from a uuu quark combination. Were it not for the extra degree of freedom from colour, the u quarks would all be in the same quantum state, violating the Pauli Exclusion Principle for fermions. Quarks come in three colours, labeled for convenience red, blue and green, with antiquarks having anticolour. Only particles with colour experience the strong force. The colour of quarks has nothing to do with the colours of visible light except that the addition of the quantum number colour behaves in many ways analogously to the addition of the primary colours of light. Ultimately, the colour of the strong force is properly described by a non-Abelian group, $SU(3)$. Hadrons, however, are made up of colourless (colour singlet) combinations of quarks, either a colour-anticolour pair in mesons, or one of each colour in baryons. The mediators of the colour force are called *gluons* and come in eight possible colour combinations, i.e., are members of a colour octet.

Unlike the electromagnetic force, which decreases rapidly with distance, the force of attraction between coloured objects is such that the energy between them increases linearly with distance. Hence quarks are *colour confined* as they would rather create $q\bar{q}$ pairs from the vacuum with the energy stored in the colour field than be separated from other quarks. An interesting effect of this, known as *asymptotic freedom*, is that at very short distances the colour forces are weak and quarks almost behave as free particles. High energy reactions (high energy means short distance scale) can then be used to investigate the properties of QCD in a regime where perturbative techniques are applicable. The strength of the strong force is expressed by the value of the strong coupling constant, $\alpha_s(Q^2)$, which is a function of the scale Q^2 (the four-momentum

transferred squared) of the interaction. It can approximately be expressed by:

$$\alpha_s(Q^2) = \frac{12\pi}{(11 - 2n_f)\ln(Q^2/\Lambda^2)},$$

where n_f is the number of quarks with mass less than the energy scale Q and Λ is a dimensional parameter determined by measurement to be around a few hundred MeV. The use of perturbative QCD (pQCD) allows one to calculate cross sections through the leading terms of a power series expansion in terms of α_s , but is only applicable at energy scales where α_s is small enough that the series converges quickly. Interactions which occur at scales where pQCD is applicable are usually referred to as being 'hard'; likewise those which occur at lower energy scales are referred to as being 'soft'. The transition between the two regimes occurs where Q^2 is around one to a few GeV^2 .

When calculating cross sections of hard interactions involving nucleons, it is necessary to know how the momentum of the nucleon is distributed amongst its *partons*, where a parton is a general term for a constituent of the nucleon, i.e., a quark or gluon. Nucleon structure functions such as $F_2(x, Q^2)$ ¹ are introduced, where x can be considered the fraction of the nucleon momentum carried by the parton involved. F_2 , in particular, can be related to the density distribution of quarks and gluons in the nucleon. Through QCD interactions, a quark may emit a gluon, or a gluon may split into a quark-antiquark pair or even two more gluons. These splittings create virtual partons which exist through the uncertainty principle for only a short period of time. Since the scale Q^2 of the interaction determines the time interval at which the hadron is being probed, the density of partons with a given momentum fraction will change with Q^2 . Although pQCD does not predict the precise shape of the structure functions, it does however predict the evolution of the structure functions with Q^2 . In other words, once $F_2(x, Q^2)$ is measured at a fixed Q^2 for all x , it can be determined for all Q^2 , at least in the regions where pQCD is applicable. A whole subindustry has sprung up parametrizing F_2 and making fits to the published data

¹There are actually many more nucleon structure functions required to fully describe deep inelastic lepton scattering [3], but F_2 is the most important one for charged lepton scattering.

available. Most notable are the parametrizations from Glück, Reya and Vogt (GRV) [4], Martin, Roberts and Stirling (MRS) [5, 6] and the CTEQ² collaboration [7] whose structure function parametrizations differ in the number of free parameters used and assumptions made.

1.2 Lepton-Hadron Scattering

One type of experiment which has made important contributions to the development of the Standard Model and in particular to the understanding of the structure of the nucleon has been the scattering of leptons by hadrons. Since leptons are considered to be point particles, they are ideal for probing the substructure of hadrons. Evidence for the existence of pointlike, charged partons within the proton was first provided in 1968 at SLAC³ where electrons of energies 9-16 GeV were scattered off protons [8]. There the angular scattering cross sections at high momentum transfers behaved more like the elastic scattering of point-like objects than the inelastic breakup of the proton. These partons were eventually identified as quarks.

The lepton essentially interacts with the partons of the hadron through the exchange of a photon⁴. The interactions are typically subdivided into two categories depending on the size of the photon momentum transfer squared Q^2 (also called the photon virtuality). If Q^2 is small, typically less than 1 GeV^2 , the photons are almost real and the events are referred to as photoproduction events. The lepton exchanges almost no transverse momentum (relative to its initial direction) and escapes the cen-

²Coordinated Theoretical Experimental Project on QCD Analysis and Phenomenology

³Stanford Linear Accelerator Center

⁴The exchange particle could also be a boson, (W^\pm , Z^0), mediating the weak interaction, but these are suppressed by a factor of $\frac{1}{Q^2 + M_{boson}^2}$ compared to $\frac{1}{Q^2}$ for pure photon exchange, where the weak bosons have masses $\sim 80-90$ GeV. Neutrino-hadron scattering, however, only occurs through the weak interaction. Also, at HERA energies, high Q^2 values can be reached and such studies attract a great deal of interest because a deviation from the Standard Model predictions can be a sign of new physics.

tral detector undetected, though it may be deflected out of the beam line by magnets into a detector further on. For larger values of Q^2 , the events are referred to as deep inelastic scattering (DIS) events and the lepton is scattered enough such that it is detected in the detector. The kinematics can then be determined by looking at either the scattered lepton or the hadrons in the event.

The diagram representing the leading order (LO) pQCD term for DIS is shown in Figure 1.1, where a photon is exchanged between the lepton and a quark from the proton. Also shown in Figure 1.1 is the diagram for leading order hard photoproduction events, where the almost real photon interacts perturbatively through boson gluon fusion (BGF) with a gluon from the proton. In this case the scale, Q^2 , of the hard interaction is no longer the four-momentum of the photon, but is determined by the transverse momentum of the quarks or by their masses if they are heavy. The BGF process is an example of *direct* photoproduction. Its counterpart, *resolved* photoproduction, will be described later in this chapter.

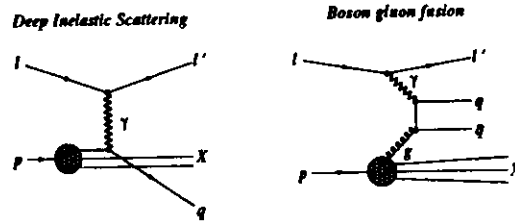


Figure 1.1: Diagrams of deep inelastic scattering (left) of a photon and a quark from the proton and boson gluon fusion (right) of a photon and a gluon

1.3 The J/ψ particle

Before delving into the particulars of J/ψ production at HERA, an overview of the history and properties of this particle will now be presented. The discovery of the

J/ψ particle played a pivotal role in the development of the Standard Model. In November 1974 the M.I.T. group at the Brookhaven National Laboratory discovered a mass resonance at $3.1 \text{ GeV}/c^2$ decaying into an e^+e^- pair from the collisions of 30 GeV protons with a beryllium target [9]. Meanwhile researchers at the electron-positron storage ring, SPEAR, at SLAC observed a sharp resonance in the cross section of e^+e^- to hadrons at the same energy [10]. Their simultaneous publications in 1974 in Physics Review Letters, along with a third, independent, confirmation [11], led to what was known as the November revolution, spurring a flood of theoretical discussion.

Its narrow mass resonance ($\sim 90 \text{ keV}/c^2$) ruled out that its constituent quarks were among the three light quarks (u, d, s) known at the time. Most particles which decay through the strong interaction have very short lifetimes and consequently, due to the uncertainty principle, have a large mass width. Thus the J/ψ could only be explained as a $q\bar{q}$ combination of a new heavy quark, the charm (c), whose existence had been postulated earlier [12]. The leaders of the two collaborations which made the discovery, Ting and Richter, were rewarded in 1976 with the Nobel prize in physics.

1.3.1 Properties of the J/ψ

The J/ψ is an example of quarkonium, a term used for mesons which are formed from a heavy quark plus its antiquark (charmonium in the specific case for charm quarks) [13]. Since it has spin 1, odd parity and odd charge conjugation ($J^{PC} = 1^{--}$), it is called a vector meson. These are the same quantum numbers which a photon has. Other examples of vector mesons made from light quarks are the ρ , ϕ , and the ω .

Since the J/ψ mass is not sufficient to produce two D mesons, which are the lightest mesons containing a charm plus a light quark, it must decay through the annihilation of the charm quarks. This is suppressed in QCD by what is known as the Zweig rule to a point where the electromagnetic decay modes compete with the hadronic ones. Here the Zweig rule manifests itself through the conservation of charge conjugation which requires that the non-electromagnetic decays of the J/ψ occurring

through $c\bar{c}$ pair annihilation proceed through the production of at least three gluons (annihilation through a single gluon being prohibited by colour conservation). The J/ψ still decays predominately to hadrons, but also has a significant decay rate to leptons, with a 6% branching fraction in each of the e^+e^- and $\mu^+\mu^-$ modes. Diagrams demonstrating these decay modes are shown in Figure 1.2.

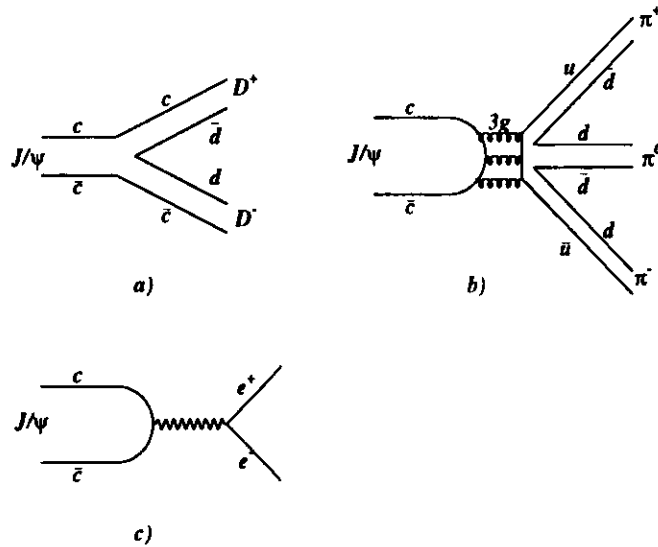


Figure 1.2: a) An otherwise preferred decay mode of the J/ψ which is not allowed because the mass ($3097 \text{ MeV}/c^2$) is insufficient to produce two D mesons ($1870 \text{ MeV}/c^2$ each). b) An example of a hadronic decay mode of the J/ψ through a three gluon exchange. c) Electromagnetic decay of the J/ψ to an e^+e^- pair through a single virtual photon.

1.3.2 Why do we still care about the J/ψ

Today, over twenty years after its discovery, the production of J/ψ mesons continues to generate interest. The charm quark mass ($m_c \sim 1.5 \text{ GeV}/c^2$), which sets the scale

of QCD interactions involving the J/ψ is just large enough to allow the application of perturbative QCD techniques. Through its leptonic decay modes it provides a clean experimental signature. This makes it useful in hadron-hadron and e^+e^- collisions where it is often used to tag B -meson (mesons with a b quark) production as it is present in some of the decay chains of the B . Furthermore, and as will be described in the next section, the production mechanisms in photoproduction can provide a direct probe of the gluon density of the proton. Indeed, at the start of the HERA running period, the measurement of the inelastic J/ψ cross section was considered to have excellent potential in constraining the gluon distribution [14, 15]. Developments in the past few years though, seem to show that elastic J/ψ production is actually more sensitive. However, interest in inelastic J/ψ production has taken a new emphasis in trying to understand the interplay of perturbative and nonperturbative dynamics of quarkonium production.

1.4 Production Mechanisms of the J/ψ

The various mechanisms of J/ψ photoproduction occupy different regions of phase space characterized by the Lorentz invariant inelasticity variable,

$$z = P_p \cdot k_\psi / P_p \cdot k_\gamma,$$

where P_p, k_ψ, k_γ are respectively the momenta of the hadron, J/ψ and photon. In the rest frame of the hadron, z is the ratio of the J/ψ energy to the photon energy. J/ψ 's produced by elastic and diffractive processes have z values at or near one and have low values of transverse momentum (p_t) relative to the colliding beams. Meanwhile, inelastic production mechanisms can span the whole range of $z < 1.0$ with the J/ψ having significant p_t .

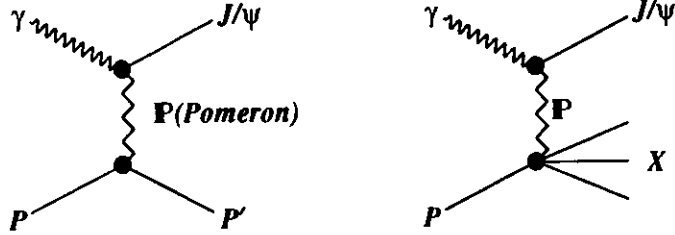


Figure 1.3: Diagrams for elastic photoproduction of J/ψ (left) and diffractive photoproduction of J/ψ through proton dissociation (right).

1.4.1 Elastic and Diffractive

Since the J/ψ is a vector meson, with the same quantum numbers as the photon, one can imagine interactions occurring where the photon first fluctuates into a vector meson such as the J/ψ before interacting with the hadronic target. The model incorporating this idea, called the vector meson dominance model (VDM) [17] could describe elastic and diffractive J/ψ photoproduction at low (10-20 GeV) centre of mass energies [18]. In diffractive models, the proton dissociates into some low mass state, with mass M_X , with the cross section decreasing roughly with M_X^2 . The exchange particle in these reactions is a pseudo-particle called the pomeron (\mathbf{P}), an object with the same quantum numbers as the vacuum. The Feynman diagrams for elastic and proton diffractive dissociation are shown in Figure 1.3. Models based on perturbative QCD treat the pomeron as a colourless pair of gluons, or more elaborately, as a series of gluon ladder diagrams [19, 20]. Such models predict a more rapid increase of the cross section with $W_{\gamma p}$, the photon-proton centre of mass energy, than VDM, with the cross section varying with the square of the gluon density. According to these models, the scale at which the gluon density is probed is $Q^2 \sim m_\psi^2/4$, where m_ψ is the mass of the J/ψ . Predictions from an improved version of the perturbative QCD model [21], albeit with uncertainties in the overall normalization,

have compared favourably with initial results from HERA. Figure 1.4 shows how the variation of the cross section with the photon-proton centre of mass energy, $W_{\gamma p}$, can distinguish between different structure function parametrizations.

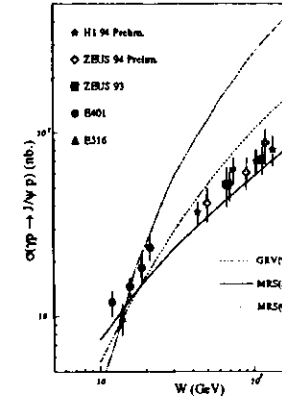


Figure 1.4: The measurements [22, 23, 24] of the cross section for diffractive J/ψ photoproduction compared with the full perturbative QCD prediction obtained with three recent structure function sets. Although the predictions have a significant normalization uncertainty, the shape of the cross section clearly favours MRS(A') over GRV(94).

1.4.2 Inelastic J/ψ Production

Over the years, three models have been used to describe the inelastic production of heavy quark states in high energy collisions: the colour evaporation model [25], the colour singlet model [27] and, very recently, a factorization model [29]. They share the similarity that the production mechanisms can be divided into a short distance, short time scale, perturbatively calculable part, which, in the case of J/ψ photoproduction, includes the diagram where a photon and gluon combine to form a $c\bar{c}$ pair (boson gluon fusion), and a long distance, long time scale, nonperturbative part where the $c\bar{c}$ pair somehow combines to make the transition into a J/ψ . They differ in the description

of how this nonperturbative part occurs and on the constraints this places on the allowed angular momentum and colour states in the short distance part. Although they are described below for the case of the J/ψ in photoproduction, the basic arguments can also be applied to the production of any quarkonium state and to hadron-hadron collisions.

In the *colour evaporation* model one assumes that the colour octet $c\bar{c}$ pair transforms into a colour singlet state nonperturbatively by emitting soft gluons. One calculates the short distance open charm cross section ($\gamma g \rightarrow c\bar{c}$), averaging over all possible spin and colour states, and makes the assumption that some fraction of the states where the $c\bar{c}$ pair has a mass between the charm quark production threshold of $2m_c$ and $2m_D$, the threshold of producing a pair of D mesons, will end up as a particular charmonium state. This fraction is not specified in the theory but should be constant at all energies and independent of the hard process. However, one of the predictions is that the characteristics of J/ψ production should be essentially the same as that of open charm ($D\bar{D}$) production. This model describes qualitatively many of the features of J/ψ production in hadron-hadron collisions [26] but no definitive predictions have been made for photoproduction at HERA.

The standard description of inelastic J/ψ production has traditionally been the *colour singlet* model. It explicitly requires that the $c\bar{c}$ produced at short distances be in a colour singlet state with the correct quantum numbers to be a J/ψ . This is achieved by requiring that a perturbatively calculable gluon, which carries off the correct colour and spin, be emitted during the short distance interaction. To leading order the subprocess is described by

$$\gamma + g \rightarrow J/\psi + g.$$

This production amplitude can be factorized into that of the hard boson gluon fusion subprocess, $\gamma + g \rightarrow c\bar{c} + g$, where in a static approximation, the relative momentum of the charm quarks is ignored, combined with the nonrelativistic wavefunction of the J/ψ . The binding energy is neglected and the J/ψ is treated as an S-wave $c\bar{c}$ system with each of the charm quarks carrying half the mass and half the momentum of the

J/ψ . The wavefunction can then be determined from the leptonic decay width of the J/ψ which, in principle, provides the absolute normalization of the cross section. The diagram representing the colour singlet model is shown in Figure 1.5.

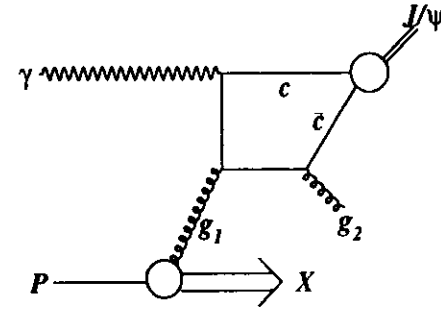


Figure 1.5: Leading order diagram for inelastic J/ψ photoproduction via the colour singlet model.

The J/ψ radial wavefunction at the origin, $\varphi(0)$, is related to the J/ψ measured leptonic decay width, Λ_{ee} , by

$$\Lambda_{ee}^0 = \frac{16\pi\alpha^2 e_c^2}{m_\psi^2} |\varphi(0)|^2,$$

where α is the electromagnetic coupling constant and e_c is the charge of the charm quark. After including the leading order QCD radiative corrections to the leptonic width, one obtains [28]

$$\Lambda_{ee} = \left(1 - \frac{16\alpha_s}{3\pi}\right) \Lambda_{ee}^0.$$

All long distance effects should be contained in $|\psi(0)|^2$ which allows the colour singlet model to make absolute predictions.

An upper cutoff in z must be applied to the colour singlet model to remain in a perturbative region where both the initial and final gluons are hard. Also, at large z the J/ψ scatters more elastically and near this end point in the kinematics (a singularity for $z = 1$) the corrections due to multiple soft gluon emission can become large.

In addition, contributions from elastic or diffractive processes can become significant at large enough z making it difficult to obtain a pure sample of inelastic events in this region. Consequently, fixed target experiments which investigated inelastic J/ψ photoproduction in the 80's and early 90's normally applied a cut in z between 0.9 and 0.95. The resulting measurements from photoproduction (FTPS,NA14) [24, 30] and muoproduction(NMC, EMC) [31, 32] fixed target experiments found that the colour singlet model described the differential distributions in z and p_t well, but the overall normalization was at least a factor of 2-3 too low. These were attributed to higher order corrections, higher twists (extra diagrams involving the intrinsic perpendicular momentum (k_T) of the gluons in the proton which lead to terms with a $(1/Q^2)^n$ dependence), relativistic effects on the J/ψ bound state and contributions from decays of ψ' ($\psi(2S)$) or higher mass charmonium states. Nevertheless, by assuming that these extra corrections did not affect the differential distributions, EMC and NMC made measurements of the gluon density $G(x)$ in the range $10^{-2} < x_f < 10^{-1}$ by fitting the shape of the $xG(x, Q^2)$ distribution and including an arbitrary normalization.

The value of x_f can be calculated to leading order from the event variables as follows:

$$x_f = \frac{\hat{s} + Q^2}{ys},$$

where y is the fraction of energy transferred from the lepton to the proton, s is the lepton-proton centre of mass energy and \hat{s} , the centre of mass energy of the hadronic system, is

$$\hat{s} = \frac{p_t^2 + (1-z)m_\psi^2}{z(1-z)}.$$

Recent theoretical advances have included next-to-leading order (NLO) [33] and relativistic corrections [34] to the original colour singlet model. The relativistic treatment of the internal motion of the bound charm quarks increased the cross section in the high z region, improving the agreement with EMC and NMC data. The NLO corrections (to order α_s^2 , where α is the electromagnetic coupling constant) increased the predicted cross section, leading to good overall agreement with photoproduction data from fixed target experiments at low centre of mass energies in the region $z < 0.9$.

However, the calculations prove to be unstable at high values of z and low values of p_t .

The authors of the NLO calculations believe that they are valid in the region $z < 0.8$ and $p_t > 1$ GeV/c. Unfortunately the p_t cut forces the average x_f to be higher, reducing the sensitivity of the total cross section to different gluon distributions. Figure 1.6 shows the predictions of the NLO calculations for inelastic J/ψ cross sections using different gluon distributions. The absolute normalization is still somewhat uncertain as the calculations are also sensitive to the choice of values used for the charm mass, the renormalization and factorization scales and α_s .

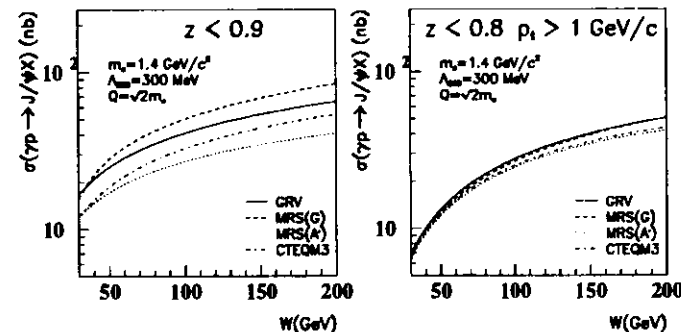


Figure 1.6: Comparison of the sensitivity of the NLO calculations of the inelastic J/ψ photoproduction cross section to different gluon distributions for two different kinematic ranges [35].

More recently, predictions have also been made for inelastic J/ψ photoproduction at HERA using a new factorization model which includes colour octet contributions to the cross section [35, 36]. This factorization model [37] was successful in explaining the drastic excess of J/ψ and ψ' production at high transverse momentum seen by the CDF detector at the Tevatron ($p\bar{p}$ collider) [38] compared to theoretical predictions based on the colour singlet model and fragmentation processes⁵. According to this factorization model, the cross section for J/ψ production can be expressed as a sum

⁵Fragmentation production of J/ψ mesons occurs when a hard parton produces a $c\bar{c}$ pair dur-

of terms, each of which factors into a short distance part and a long-distance matrix element:

$$d\sigma(\gamma + g \rightarrow J/\psi + X) = \sum_n d\hat{\sigma}(\gamma + g \rightarrow c\bar{c}[n] + X) \langle 0 | \mathcal{O}^{J/\psi}[n] | 0 \rangle$$

where $\langle 0 | \mathcal{O}^{J/\psi}[n] | 0 \rangle$ is a matrix element expressing the probability that the $c\bar{c}$ pair in some colour, spin and angular momentum state $[n]$ converts over a long distance to a J/ψ through the emission of soft gluons.

Using rules from nonrelativistic QCD (NRQCD) [39], an effective field theory, the long distance matrix elements can be expressed in powers of v/c , where v is the average velocity of the charm quark in the J/ψ rest frame and v^2/c^2 is estimated to be ~ 0.25 [40]. The use of NRQCD provides for a systematic method to absorb into the long distance matrix elements effects which occur at scales of $m_c v/c$ which could otherwise lead to divergences in the calculations. In the limit $v \rightarrow 0$, the factorization model reduces to the colour singlet model. However, for non-zero values of v/c , colour octet terms, although suppressed by powers of v/c , can be enhanced by numerical factors from their short distance part and lead to a significant contribution to the cross section. The precise values of the matrix elements can in principle be determined either by lattice QCD calculations or by fits to experimental data. The latter was done with the CDF data and agreed roughly with what was expected from counting powers of v [37]. Using the values determined at CDF, calculations have been made for the colour octet contributions at HERA [35, 36]. Although a sizable contribution is expected, a measurement of the total cross section is not believed to be very sensitive to the colour octet terms because of the uncertainties in the absolute normalization of the NLO calculation mentioned earlier. However, the calculations do predict a very steep rise with z in the differential cross section compared to the colour singlet model (see Figure 1.7). A significant deviation in the z distribution from the expectations of the colour singlet model could signify the presence of colour octet terms. Fragmentation is the main source of J/ψ production at large (~ 10 GeV/c) p_t .

octet terms.

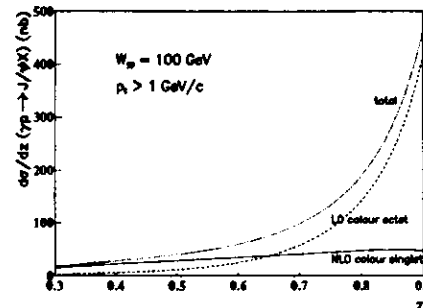


Figure 1.7: The predicted J/ψ energy distribution $d\sigma/dz$ integrated over $p_t > 1$ GeV for $W_{pp} = 100$ GeV.

Higher mass $c\bar{c}$ bound states can also contribute to J/ψ production through their decay channels. In particular, ψ' particles, which have the same quantum numbers as the J/ψ , decay 57% of the time to J/ψ particles plus two pions. Estimates from the colour singlet model [33] predict the $\sigma(\gamma P \rightarrow \psi' X)/\sigma(\gamma P \rightarrow J/\psi X)$ ratio to be ~ 0.25 , in rough agreement with values from photo- and hadroproduction experiments [30].

Mechanisms involving resolved photoproduction or B -meson decays are additional possible sources of inelastic J/ψ , but are generally confined to low values of z . In hadron-hadron collisions at sufficiently high energies, B decays represent a significant source ($\sim 20\%$) of J/ψ production [41]. However the relative cross section is expected to be small at HERA except at high values of p_t and can be safely neglected for the purposes of this study [15].

Next, we describe resolved photoproduction of J/ψ as it is expected to be seen for the first time at HERA. Often called the anomalous contribution of the photon, resolved photon processes treat the photon as having a virtual partonic structure. During the hard interaction a quark or gluon from the photon can interact with a

parton in the proton to produce J/ψ 's either directly or through intermediate states. Some of the possible processes are [15]:

$$g + g \rightarrow J/\psi + g$$

$$g + g \rightarrow J/\psi + \gamma$$

$$g + g \rightarrow (\chi \rightarrow J/\psi + \gamma) + g$$

$$g + q \rightarrow (\chi \rightarrow J/\psi + \gamma) + q.$$

An example of J/ψ production through a resolved photon is shown in Figure 1.8.

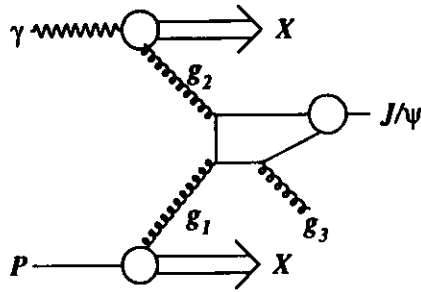


Figure 1.8: J/ψ production through a resolved photon

An investigation into J/ψ production through resolved photon processes would be interesting because it could give insight into the partonic structure of the photon. However, their overall cross section is small compared to the direct photon (BGF) process and only dominates in the experimentally difficult region at low values of z [15, 16]. Resolved photon processes will be experimentally excluded in this study by requiring a lower bound in z .

The rest of this thesis will concentrate on the extraction of the inelastic J/ψ photoproduction cross section in a kinematic region where the resolved photon process

does not contribute and the proton dissociation contribution is small (by avoiding high and low z). In such a region the NLO calculations for the colour singlet model are also more trustworthy. Elastic $J/\psi \rightarrow e^+e^-$ events will be used to determine in part the efficiency of the selection cuts. A comparison will be made between the data and the NLO predictions of the colour singlet model. The differential distributions will also be examined. Thus, in the following chapters *inelastic* J/ψ production will refer to the direct photon process unless otherwise specified.

Chapter 2

The Experiment

2.1 HERA (Hadron Elektron Ring Anlage)

The HERA ep collider is located at the Deutsches Elektronen-Synchrotron (DESY) within the city of Hamburg, Germany. Construction of the 6.3 km long tunnel housing the proton and electron rings began in 1984. To reduce the cost of the project, existing accelerators were modified to serve as injectors for the main rings. In addition, several nations, including Canada, participated in the design and construction of HERA and its injection systems, combining to contribute roughly 20% of the cost of the collider. By fall 1990 the last of the superconducting magnets for the proton rings was in place. After the installation and commissioning of their detectors, the experiments ZEUS and H1 witnessed the first collisions between 26.7 GeV electrons and 820 GeV protons in 1992. The layout of the HERA ring and its preaccelerators is shown in Figure 2.1 and Figure 2.2.

The proton injection chain begins with negatively charged hydrogen ions brought to 750 keV with a radiofrequency quadrupole and then accelerated to 50 MeV by an H^- linac (linear accelerator). During injection into the proton synchrotron DESY III they are stripped of their electrons. The protons are then collected into bunches and accelerated to 7.5 GeV before being transferred into the PETRA ring, which is also part of the electron injection system. After being accelerated in PETRA to 40 GeV,

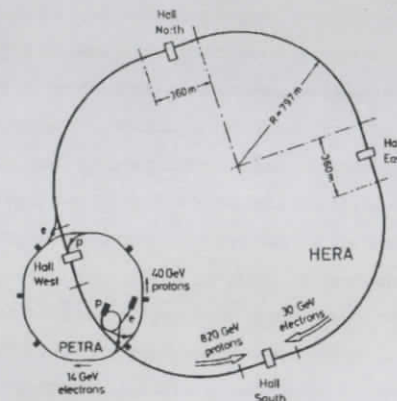


Figure 2.1: Layout of the HERA ring.

the proton bunches are ready to enter the HERA ring. In HERA they are accelerated to their final energy of 820 GeV. The final energy of the protons is limited by the strength of the 4.65 T superconducting dipole magnets needed to bend them around the ring. A complete fill typically takes a few hours and the final resulting beam has a lifetime (exponential decay constant of the current) of well over 100 hours.

The electron injection system begins with a linac system which can produce pulses of either 450 MeV electrons or positrons. The pulses are collected into single bunches in the accumulator ring PIA and then accelerated by the synchrotron DESY II to 7 GeV. From DESY II the electrons are transferred to PETRA, where they are accelerated to 12 GeV before injection into HERA. In HERA the maximum electron beam energy of 30 GeV is limited by the amount of power that can be delivered by the radiofrequency cavities to replace that lost through synchrotron radiation. It takes about an hour to complete an electron fill and the lifetime of the electron beam is nominally around 10 hours.

Since both the lifetime and filling time of the proton beam are much longer than

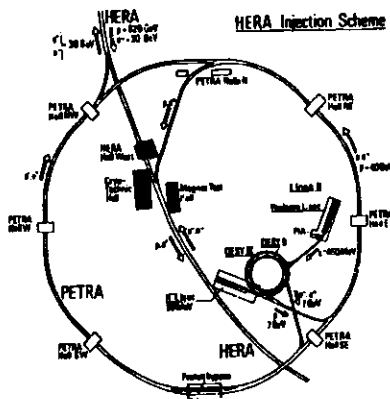


Figure 2.2: Layout of the HERA injection system.

those of the electron beam, the protons are injected before the electrons. Multiple electron fills are possible for a single proton beam, but eventually the transverse size of the proton beam blows up from its interactions with the electron beam and both beams must then be discarded and a new fill started.

HERA began the running period in 1994 using high intensity electron beams but encountered problems with the lifetime of the electron beam which would rapidly drop when the current got too high. The suspected cause was the presence of small ($< 1\mu\text{m}$) ionized "dust" particles, which, being positively charged, were attracted to and trapped by the electron beam, scattering the electrons. The occurrence of the dust particles was correlated to the operation of the ion getter pumps used by HERA, as the problem was seen to become more severe with higher pump voltages. In July, 1994 HERA reversed the polarity of the magnets in the electron ring and switched to using positrons, effectively bypassing the problem, since the ionized particles were repelled by the positively charged beam. Since the beam electrons are used mostly as a source of real or virtual photons, the cross sections of the physics processes at HERA, aside

from charged-current reactions, are unaffected by the switch. A replacement of the vacuum pumps, which would allow the resumption of operating with high intensity electron beams, is planned for the future. For the remainder of this thesis, electrons will be used synonymously with positrons.

Of the 220 available bunch positions¹, called buckets, available at HERA, 153 were filled in 1994 with colliding bunches. There were also 32 buckets which were filled with electron (15) and proton (17) non-colliding bunches. These non-colliding bunches, called pilot bunches, are used to monitor backgrounds from beam-gas interactions, which are the unwanted interactions between beam particles and remnant gas molecules in the beampipe. The remaining empty buckets are used to determine the background from cosmic ray events. The relevant parameters characterizing HERA are summarized in Table 2.1.

The instantaneous luminosity, L , of an ep storage ring is given by

$$L = \frac{N_e N_p n f_0}{2\pi(\sigma_{xp}^2 + \sigma_{xe}^2)^{1/2}(\sigma_{yp}^2 + \sigma_{ye}^2)^{1/2}},$$

where f_0 is the revolution frequency, n is the number of colliding bunches in each beam; N_e and N_p are the number of electrons and protons in each bunch; and σ_x and σ_y are the horizontal and vertical beam sizes of the electron and proton beams at the interaction point. The sizes of the beams are determined by the emittance, ϵ , and the β function, where $\sigma(s) = \sqrt{\epsilon\beta(s)}$ and s is the position along the beam path. The β function gives the position dependent part of the amplitude of the beam particle oscillation along the beam path, whereas the emittance is the amplitude of the position independent oscillations of the beam. The emittances of the HERA beams are limited by the preaccelerators. Focussing magnets are used to make the β function as small as possible at the interaction point, however, efforts to reduce its size at one point causes it to increase elsewhere, limiting how small the β function

¹Particles travelling along the beam path must be in phase with the radiofrequency cavities to be properly accelerated. This causes the particles to bunch together at certain locations where they get just the right energy to stay along the beam path. The number of available bunch positions thus depends on the frequency of the cavities.

Parameter	1994	Design	units
Proton energy		820	GeV
Electron (Positron) energy	27.52	30	GeV
Centre of mass energy	300	314	GeV
Q_{max}^2	90300	98400	(GeV/c) ²
Number of interaction points		4	
Crossing angle		0	mrad
Circumference		6336	m
Number of buckets		220	
Number of colliding bunches	153	200	
N_e /bunch	2.0	3.6	10^{10}
I_e	27	58	mA
N_p /bunch	3	10	10^{10}
I_p	40	160	mA
$\sigma_{x,y}(e)$.29 .045	.27 .036	mm
$\sigma_{x,y}(p)$.20 .055	.27 .08	mm
Instantaneous Luminosity	2.5	15	$10^{31} \text{ cm}^{-2} \text{ s}^{-1}$
Specific Luminosity	4.4	3.4	$10^{29} \text{ cm}^{-2} \text{ s}^{-1} \text{ A}^{-2}$
Time between crossings		96	ns
Operation efficiency	32	70	%

Table 2.1: Parameters of the HERA collider, design and in 1994.

can be made in the interaction region. Nevertheless, as Table 2.1 shows, in 1994 the specific luminosity, which is the instantaneous luminosity divided by the beam currents, actually surpassed the design value. The main limitations to the integrated luminosity were instead the size of the beam currents and the operation efficiency, i.e., the amount of time HERA actually provided luminosity divided by the total time scheduled for luminosity. In 1994 HERA delivered a total of 6.2 pb^{-1} of luminosity to ZEUS, of which the first 1.1 pb^{-1} were with electron beams.² The accumulated luminosity delivered to and recorded by ZEUS during the 1994 running period is shown in Figure 2.3.

Four interaction regions are available for experiments. Situated several floors underground in the north and south experimental halls, the two largest experiments,

²A barn (b) is a unit of cross section where $1 \text{ b} = 10^{-24} \text{ cm}^2$. So an inverse picobarn (pb^{-1}) is 10^{30} cm^{-2}

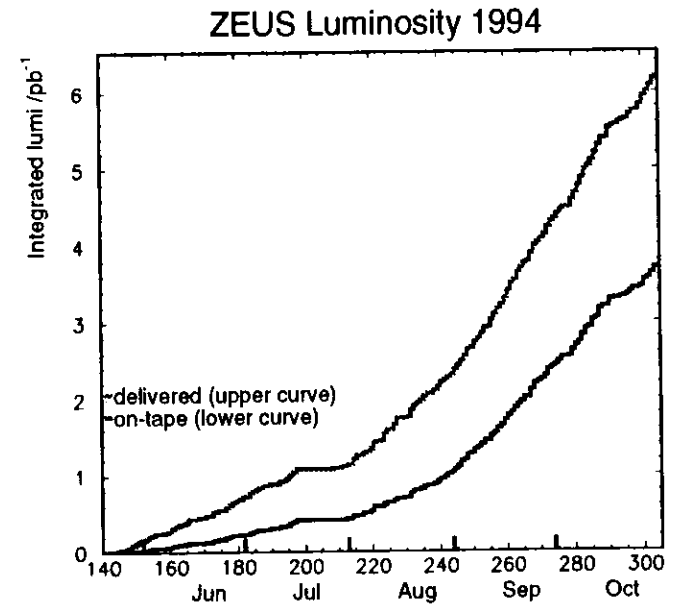


Figure 2.3: Integrated Luminosity in 1994. The upper curve shows the integrated luminosity delivered by HERA to the ZEUS interaction region over the course of the year. The lower curve shows the integrated amount of luminosity actually recorded by ZEUS.

H1 and ZEUS, study collisions between electrons (positrons) and protons. Two non-colliding beam experiments complete the physics programs at HERA: HERMES, which uses the polarized electron beam colliding with a deuterium gas jet target to measure spin dependent structure functions, and HERA-B, which uses a thin wire target interacting with off-axis protons accompanying the proton beam (called beam halo) to study CP-violation through the production and decay of B mesons.

2.2 The ZEUS Detector

The probe deeper into the structure of matter has necessitated the construction of ever larger colliders. As a result the detectors and the collaborations that build and operate them have also grown in size. ZEUS is no exception to this rule. The three-storey 3600 ton detector is the work of a collaboration of over 400 physicists from 50 institutes in 12 countries.

The ZEUS detector is a general purpose detector with almost complete angular coverage of the interaction region. One feature which distinguishes it from most collider detectors is the asymmetry between the forward (proton direction) and rear (electron direction) regions, reflecting the inherent asymmetry of the collisions between 30 GeV electrons and 820 GeV protons. The inner region consists of multi-wire charged particle detectors, surrounded by a solenoid which provides the magnetic field to measure the momentum of charged particles. Calorimeters enclosing the inner region measure the energies of charged and neutral particles. Muon chambers signal the passage of muons which easily penetrate the calorimeters. Since the detector is almost hermetic, with the only gaps located around the beampipe, even neutrinos which pass through the entire detector without interaction can be detected, by a non-zero vector sum of the transverse energy in the calorimeter. A brief description of the detector components follows; a complete description of components can be found in [42]. Fig. 2.4 shows a schematic of the main central components with a quadrant removed. Since the main components used in this analysis are the calorimeter

and the central tracking and vertex detectors, these components will be described in somewhat more detail. Peripheral components away from the central region are also used in the trigger to veto beam-gas events.

The ZEUS coordinate system is a right-handed one, defined such that the positive z -axis is along the direction of the proton beam. The z -axis points towards the middle of HERA and the y -axis points vertically upwards. The origin of the coordinate system lies at the nominal interaction point.

2.2.1 Inner Tracking Detectors

A tracking detector determines the path of charged particles by registering signals as they traverse cells of its active medium, which in the case of multi-wire drift chambers, is usually a gas. The passage of the particles ionizes the gas, liberating electrons. The cell is placed under an electric field which causes the electrons to drift towards the anode wires, known also as sense wires. As the initial electrons approach the sense wires they gain enough energy to liberate more electrons through ionization, creating, via a cascade effect, an avalanche of electrons in the vicinity of the sense wire. The resulting electrons and positive ions are registered as a pulse by the electronics at the end of the wire. If the pulse is large enough, then the wire is considered to have a "hit". From the drift time and drift velocity in the gas the distance from the point of the initial ionization to the anode can be determined. Tracks are reconstructed by fitting curves to the individual hits. The curvature, which is due to an applied magnetic field, is inversely proportional to the transverse momentum of the particle which caused the track.

The innermost component of the ZEUS detector, immediately surrounding the beampipe, is a high resolution vertex detector (VXD) consisting of a high precision drift chamber enclosed in a thin carbon-fibre vessel containing dimethyl ether at atmospheric pressure [43]. The gas volume is divided into 120 wedged shaped cells, each with 12 sense wires in the radial region from 11 to 15 cm running parallel to the beam line and covering the polar angle region between $\theta = 8.6^\circ$ and $\theta = 165^\circ$, where

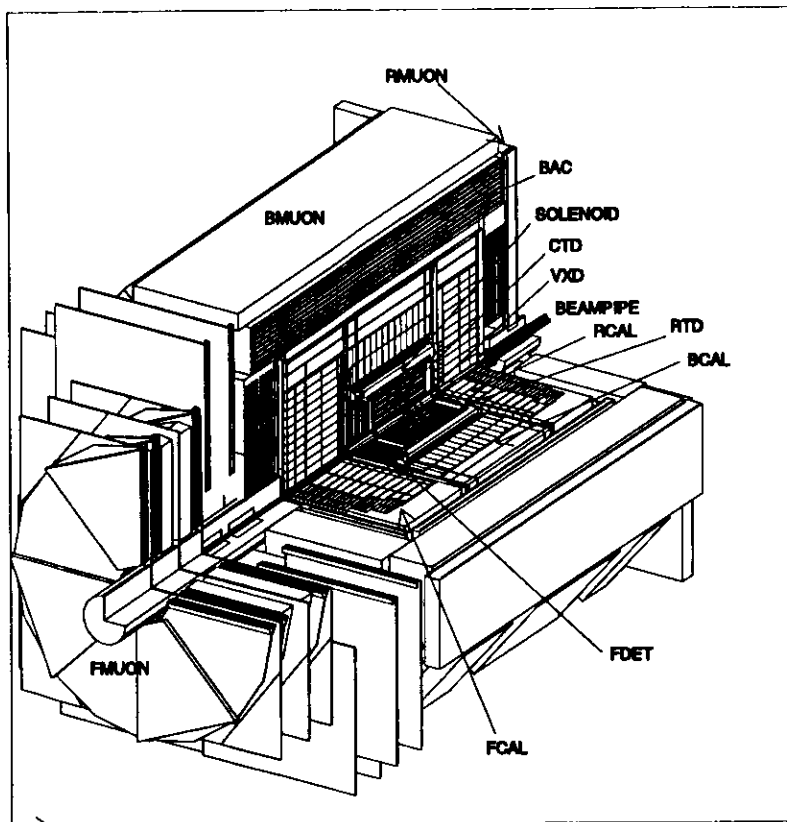


Figure 2.4: Layout of the central region of the ZEUS detector with one quadrant removed.

θ is measured from the positive z -axis. The spatial resolution for single hits ranges from $50 \mu\text{m}$ in the central region of the drift space to $150 \mu\text{m}$ near the edges.

Outside the VXD lies the principle detector used for charged particle detection, the central tracking detector (CTD) [44]. It is a cylindrical jet type drift chamber with an inner radius of 16 cm, an outer radius of 85 cm and a length of 240 cm, covering the polar angle region $15^\circ < \theta < 164^\circ$. There are 72 cylindrical layers, subdivided into 9 "superlayers", each with 8 layers of sense wires to measure track positions and particle energy loss (dE/dx). The wires are read out by 8-bit flash analog-to-digital converters (FADC's) which provide a precise measurement of the pulse arrival time as well as the pulse size for use in dE/dx measurements. Four of the superlayers (SL2, SL4, SL6, SL8) have stereo sense wires strung at angles of about ± 5 degrees which provide roughly equal resolution of the polar and azimuthal angles. The other sense wires are axial, i.e., are parallel to the beam axis, and thus normally provide only r, ϕ information. However, 16 layers (8 in SL1, and 4 each in SL3 and SL5) are also instrumented to measure the z position using the timing difference between the arrival of the pulses at either end of the wire (z -by-timing). The difference in the drift angles of the ionization electrons with the magnetic field on and off, known as the Lorentz angle, is 45° under the designed field of 1.8 Tesla. For this reason the positioning of the sense wires in a superlayer are tilted such that the electron drift lines are tangent to the chamber azimuth at the cell centre. An axial view of a CTD octant is shown in Fig. 2.5.

The CTD used a gas mixture consisting mostly of argon (85%) with some carbon dioxide (8%), ethane (7%) and traces of alcohol. The carbon dioxide and ethane act as quenchers, absorbing ultraviolet photons radiated through the de-excitation of argon. This allows the chamber to be operated at a higher gain. The alcohol increases the operational lifetime of the chamber by inhibiting the growth of organic deposits on the wires.

In 1994 a single hit resolution in $r - \phi$ reaching $240 \mu\text{m}$ was achieved and the single hit efficiency was at least 95%. The momentum resolution for full length tracks

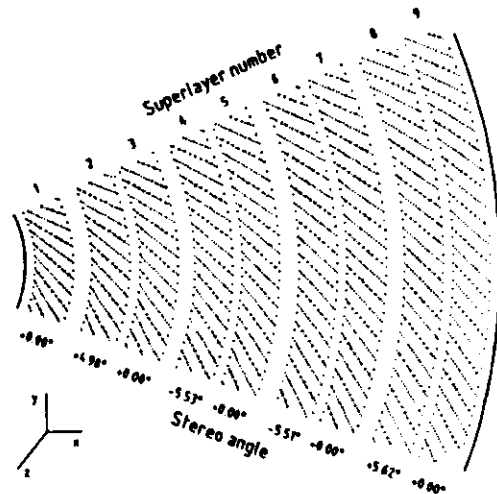


Figure 2.5: View of a CTD octant. The thick dots are the sense wires.

originating at the vertex was $\sigma(p_t)/p_t = 0.005p_t \text{ (GeV)} \oplus 0.016$, where \oplus means addition in quadrature. The vertex resolution using the CTD and the VXD was 0.4 cm in z and 0.1 cm in the $x - y$ plane.

Complementing the CTD, to improve the measurement of low angle tracks, are forward and rear track detectors (FDET, RTD) consisting of three and one planar drift chambers, respectively. The FDET was not instrumented in 1994. A transition radiation detector (TRD), designed to improve electron identification in the forward region, lies sandwiched between the FDET chambers. It was instrumented for only a short period during the 1994 data taking period.

Surrounding these inner detectors is a thin superconducting solenoid, 0.9 radiation lengths (X_0) thick, providing a magnetic field of 1.43 Tesla. Although the solenoid had originally been designed to produce a field reaching 1.8 Tesla, the magnetic axial force on the solenoid, due to the asymmetry of the calorimeters and yoke, was stronger than originally anticipated, limiting the size of the field which could safely be used.

2.2.2 Calorimetry

A calorimeter is a device designed to measure the energy of a particle entering it by fully absorbing its energy and producing a measurable signal proportional to it. When a particle enters a calorimeter it will interact with the material, producing secondary particles which in turn produce more particles propagating through the calorimeter. As this continues, a particle "shower" develops. Two types of showers can be distinguished, electromagnetic and hadronic. Electromagnetic showers are made up of photons, electrons and positrons which interact only electromagnetically through a few well understood processes which are in, principle, fully described by QED. In comparison, hadronic showers are much more complicated, involving strongly interacting particles which also partake in nuclear processes.

The two kinds of showers exhibit different properties, with the longitudinal and transverse dimensions of an electromagnetic shower being much smaller than those of a hadronic shower of the same energy. A useful scale to describe the longitudinal

development of an electromagnetic shower is the radiation length, X_0 , of the material. It is the average distance a high energy electron must travel for its energy to drop to $1/e$ of its original energy purely due to bremsstrahlung. For high energy photons, the average distance travelled before splitting into an e^+e^- pair is $9/7 X_0$. In a similar manner, the nuclear interaction length, λ , gives the longitudinal scale of a hadronic shower. λ is the average distance a hadron travels before colliding with a nucleus and is typically much larger than a radiation length.

A great deal of effort was devoted during the mid to late eighties, through Monte Carlo studies and beam tests, to understand the underlying processes occurring in hadronic showers [45]. This knowledge greatly influenced the design of the ZEUS calorimeter. Before describing the ZEUS calorimeter, we mention briefly the physics behind calorimetry which motivated the design of the calorimeter.

Most large calorimeters are sampling devices composed of interleaved layers of passive absorber and active detector. Since materials suited for detecting particles are usually made from light elements, alone they would require a large volume to stop energetic particles. However, the presence of absorber layers made from high Z elements causes the shower to develop more quickly. This allows sampling calorimeters to be compact, saving much in cost and space compared to homogeneous calorimeters. Also, as discussed below, by correctly selecting the composition and the thicknesses of the absorber and active layers, it is possible to obtain an equal average response from both hadronic and electromagnetic showers. This turns out to be a critical requirement for achieving good hadronic energy resolution.

Hadronic showers are created through the inelastic scattering of strongly interacting hadrons and their secondary particles by the nuclei of the absorber material. A wide variety of different particles are produced, including charged hadrons, low energy photons, neutrons, and electromagnetically decaying π^0 's. The various particle types have different energy loss mechanisms and hence deposit a different fraction of their energy in the active layers. Fluctuations in the relative proportions of these particle types lead to an unavoidable worsening of the energy resolution compared

to electromagnetic showers. In addition, a considerable fraction of the energy in a hadron shower is also expended overcoming nuclear binding energies, which does not contribute to the energy seen by the active layers. As a result, the ratio of the energy response of a calorimeter to electromagnetic and hadronic showers, known as e/h , is usually greater than one. Through the production of π^0 's which decay in 10^{-16} s into two photons each, hadronic showers also contain an electromagnetic component. The size of this component is quite significant and increases logarithmically with the energy of the incident particle. On average one third of the mesons produced in an inelastic interaction with a nucleus will be π^0 's. Because of this electromagnetic component, which also fluctuates significantly in size, as it is primarily determined by the first interaction of the incident particle with a nucleus, the hadronic energy resolution is degraded and the response non-linear if the e/h ratio differs from 1.

To achieve $e/h = 1$, a condition known as compensation, one has to compensate for the undetected energy losses due mostly to the breaking up of nuclei, either by increasing the response of the calorimeter to hadrons or decreasing its response to electromagnetic showers. The most effective method is to increase the response of the calorimeter to hadronic showers for which the primary mechanism is to include hydrogenous material in the active layers. In the final stages of a hadronic shower's development most of the energy is spent on nuclear processes, producing low energy neutrons, protons and gammas. Many more neutrons are released if large Z materials are used. These soft neutrons are eventually recaptured and normally lose their energy invisibly through elastic scattering. However, if the calorimeter contains hydrogen in the active readout material, much of this lost energy will be recovered. The neutrons transfer a large fraction of their kinetic energy to the hydrogen atoms, producing recoil protons. These low energy (~ 1 MeV) protons have a very short range and since they originated in the active layers, they deposit all their energy there. The amount of compensation can be adjusted by varying the relative thicknesses of the active and passive layers of the calorimeter or by adjusting the fraction of hydrogen atoms in the active medium.

2.2.3 The ZEUS Calorimeter

The ZEUS calorimeter (CAL) [46, 47] is a high resolution sampling calorimeter using uranium as absorber and scintillator as the active material. It is divided into three distinct sections, the Forward Calorimeter (FCAL), Rear Calorimeter (RCAL) and the Barrel Calorimeter (BCAL), which together enclose the solenoid and inner tracking detectors³. FCAL covers the polar angles from $\theta = 2.2^\circ$ to 39.9° ; BCAL extends from $\theta = 36.7^\circ$ to 129.2° , and RCAL covers $\theta = 128.1^\circ$ to 176.5° . Together they cover 99.8% of the solid angle in the forward hemisphere and 99.5% in the backward hemisphere. The face of FCAL is situated at $z = 2.2$ m; RCAL is at $z = -1.5$ m, and BCAL is 1.2 m radially distant from the interaction region.

Each calorimeter is longitudinally segmented into electromagnetic (EMC) and hadronic sections (HAC1 and HAC2), with the EMC section roughly a third as deep as a single HAC section. RCAL has no HAC2 section because the most energetic jets go in the forward direction. The division between the EMC and HAC sections greatly helps in distinguishing between electromagnetic showers (e^\pm, γ) and hadronic showers because incident electrons or photons deposit almost all their energy in the EMC section, whereas hadrons deposit a substantial fraction in the HAC sections.

FCAL and RCAL are structurally divided into rectangular modules, 20 cm wide and between 2 and 4.4 m high. BCAL is divided into 32 identical wedged shaped modules attached at either end to radial spokeplates. FCAL and RCAL are divided into non-projective tower cells of 20×20 cm² for readout in the HAC sections. The EMC sections, except for those shadowed by parts of BCAL (called HAC0), are further segmented, with the cells in FCAL being 5×20 cm² large and those in RCAL 10×20 cm². The towers, as seen from the interaction region, form a grid of 20×20 cm² squares, with the central square left empty for the beam-pipe to pass. The EMC cells in BCAL are roughly projective in both θ and in azimuthal angle, ϕ , whereas the HAC cells are projective only in ϕ . Each BCAL module is rotated

³ FCAL and RCAL were constructed in Canada and the Netherlands. BCAL was constructed in the United States.

by 2.5 degrees in the azimuthal plane around an axis parallel to the beam axis but located at a radius of 2.3 m. This ensures that the gaps between the modules do not point towards the beam axis. The modules are subdivided into 53 EMC cells, each with a frontal transverse size of 5×24 cm², and 14 HAC1 and 14 HAC2 cells. The cells are also grouped in a tower structure with a HAC cell behind every four EMC cells, except for the foremost (rear-most) HAC cells which have only 2 (3) EMC cells in front. In total, the calorimeter is seven nuclear interaction lengths deep in FCAL, five in BCAL and four in RCAL. This depth is sufficient to contain over 95% of the energy of the highest energy jets expected anywhere in the calorimeter 90% of the time.

The calorimeters are made of stacked layers composed mainly of 3.3 mm thick depleted uranium⁴ plates and 2.6 mm thick plastic scintillator tiles. Wavelength shifting light guides along either side of the towers transport the light from the scintillator to photomultiplier tubes (PMTs) at the back of the modules. The ratio of uranium to scintillator thickness was chosen such that the calorimeter is fully compensating.

Through the use of test beams the energy resolution of the calorimeter was determined to be $\sigma(E)/E = 18\%/\sqrt{E}$ (GeV) $\oplus 1\%$ for electrons and $\sigma(E)/E = 35\%/\sqrt{E} \oplus 2\%$ for hadrons. The fast response time of the scintillators results in an overall timing resolution of better than 1 ns, aiding in the rejection of beam-gas events. The performance of the calorimeter is continuously monitored and calibrated through pedestal triggers, charge and light injection, and measurements of the background current from uranium radiation (UNO).

A layer of 3×3 cm² silicon detectors, called hadron electron separators (HES), is embedded at a depth of $3 X_0$ inside the EMC section of RCAL to improve the discrimination of electrons from pions, especially within jets. The small size of the HES diodes and their forward positioning allow them to differentiate between electrons and hadrons because electron showers are narrower and develop more quickly than hadron showers. Space is also reserved for the HES in FCAL and BCAL, but

⁴an alloy of 98.4% ²³⁸U, 1.4% Nb and $\leq 0.2\%$ ²³⁵U

they had not been installed as of 1994.

The backing calorimeter (BAC) surrounds the CAL. It measures the energy of particles from showers which leak through the uranium calorimeter. It uses the iron plates of the magnet yoke as absorber and proportional tubes made from aluminum as signal layers. The energy resolution for hadrons is $\sigma(E)/E = 100\%/\sqrt{E}$.

2.2.4 Muon Detectors

Muons behave as minimum ionizing particles which easily penetrate the calorimeter if they have more than a couple of GeV of energy. Their distinct signature provides a clean indication of heavy flavour production or of processes involving exotic physics. The barrel and rear muon detectors (BMUON, RMUON) use limited streamer tubes in front of and behind the yoke to identify particles penetrating the calorimeter [48]. They distinguish between background interactions (events) arising from cosmic ray and beam halo muons⁵ and events originating in the interaction region. The forward muon spectrometer (FMUON) provides an independent momentum measurement of muons as well as improves the rejection of muons from background sources. It uses two toroidally magnetized iron regions interleaved with drift chambers, limited streamer tubes, and time-of-flight counters.

2.2.5 Luminosity Monitor

The luminosity is determined by measuring the rate of high energy bremsstrahlung photons produced by the Bethe-Heitler [49] process $ep \rightarrow e\gamma$ and detected in the photon detector of the luminosity monitor. This process has a very high rate and since it involves only QED, it can be calculated to high accuracy. The pilot bunches are used to statistically subtract the background from beam-gas interactions. The photon detector is a lead-scintillator calorimeter situated 107 m down the beamline.

⁵Beam halo muons are the result of interactions between protons and gas upstream of the ZEUS detector. Some of the particles (pions, kaons) produced in these interactions decay in flight to produce muons.

The photons exit the proton beampipe through a copper exit window 82 m from the interaction point and must penetrate a carbon filter which shields against synchrotron radiation before reaching the photon detector.

Another lead-scintillator calorimeter, positioned 35 m from the interaction region, detects the scattered electrons from bremsstrahlung events and low Q^2 photoproduction events. It accepts electrons deflected by the beam magnets with scattering angles less than 5 mrad and energies between $0.2 E_e$ and $0.9 E_e$, where E_e is the initial electron energy.

2.2.6 Other Detectors

A leading proton spectrometer (LPS) tags elastically scattered protons which would otherwise escape down the beampipe. It consists of six stations of high resolution silicon strip detectors distributed along the region between $z = 24$ and $z = 90$ m, of which only the furthest three were operational in 1994. With the beam magnets providing the bending field, and a spatial resolution of $\pm 25 \mu\text{m}$, a momentum resolution of less than 1% can be reached for elastically scattered protons.

The VETOWALL, located at $z = -7.5$ m, is an 87 cm thick iron wall supporting on each side a 5×6 m scintillator hodoscope. It shields the detector from beam halo particles and vetos events in coincidence with particles penetrating it.

A set of four small scintillator counters at $z = -315$ cm surrounding $3/4$ of the beampipe near the C5 collimator magnet forms the C5 detector. As with the VETOWALL, it is used to veto beam halo events. The timing information from the C5 detector is used to verify the relative timing of the beams. The remaining area around the beampipe is covered by a beampipe calorimeter (BPC). Made of layers of tungsten plates and silicon diodes, the BPC detects low-angle scattered electrons.

Seven pairs of scintillator sheets located around the beampipe at $z = 5$ m (2 pairs) and $z = 24$ m (5 pairs) form the Proton Remnant Tagger (PRT). As its name suggests, it detects particles from the proton remnant which escaped detection by the CAL through the beampipe hole, thus providing a means of distinguishing low mass

diffractive events, which leave no energy in the FCAL, from truly elastic ones.

An array of vertical and horizontal scintillator strips positioned in front of the inner ring of RCAL towers forms the Small angle Rear Track Detector (SRTD). It provides an accurate position measurement for DIS electrons and also allows one to correct the calorimeter measurement of their energy. Due to the abundance of inactive material at low angles in front of RCAL, the scattered electron can lose a significant amount of energy before entering the calorimeter. This loss can be corrected by taking advantage of the correlation between the energy measured in the SRTD and the energy lost from showering in the inactive material.

Situated 102 m from the interaction region along the proton direction is the Forward Neutron Calorimeter (FNC). Made of layers of iron and scintillator, its purpose is to detect the leading neutron produced from interactions where the proton exchanges a pion with the virtual photon coming from the electron, producing a high momentum neutron.

2.3 Data Acquisition

During the running period in 1994 a four person shift crew operated the ZEUS data acquisition system around the clock and performed online (real time) data quality monitoring and safety checks. Calibration and cosmic ray muon runs were also taken when HERA was not in luminosity operation. The events which were accepted by the local data acquisition system located in the ZEUS hall were transferred over a high speed link to the DESY computer centre where they were stored onto tape cartridges while awaiting reconstruction.

2.3.1 Trigger

The short time between bunch crossings (96 ns) places severe demands on the trigger system. Most of the interactions seen by the ZEUS detector originate from collisions between beam particles and gas molecules inside the beampipe. ZEUS uses a three

level trigger system to sift through the ~ 50 kHz beam-gas interaction rate and record a few Hz of data onto tape. Each trigger level uses the information available to decide quickly whether to keep or discard the event. The higher trigger levels have more time and more refined information available and hence can make use of more sophisticated selection algorithms. The result of a specific trigger algorithm (YES or NO) is recorded as a trigger bit located in a data table. An overview of the ZEUS trigger system is illustrated in Figure 2.6.

2.3.2 The First Level Trigger

The first level trigger (FLT) is designed to accept data at a rate of up to 1 kHz, although in practice the deadtime (the amount of time lost because the detector readout is busy) starts to rise after several hundred Hz. Each of the independent components has its own first level trigger using custom-built hardware. The data are stored in a pipeline containing data from 58 beam crossings. The components must send their information to the global first level trigger (GFLT) between 1 and 2.5 μ s after the crossing. The GFLT makes its decision 4.4 μ s after the crossing. The time constraints allow only quickly available information to be used, such as rough energy sums or rudimentary tracking.

2.3.3 The Second Level Trigger

The second level trigger (SLT) is designed to reduce the data rate by roughly a factor of ten. As with the FLT, every component has its own SLT. The SLT makes heavy use of transputers, which are powerful processors highly suited for parallel applications. The SLT has time to calculate such quantities as calorimeter energy and timing. After removing events which fail vetos based on calorimeter timing and energy, simple filters are applied to select events which should be passed on to the next stage. If the SLT accepts an event, the Event Builder collects and organizes all the data from the components before sending the complete event information to the

third level trigger.

2.3.4 The Third Level Trigger

The third level trigger (TLT) consists of a farm of some 30 Silicon Graphics (SGI) servers⁶ which process events using data from all the components. It uses calorimeter timing and track reconstruction to reject much of the remaining non-colliding beam background. Fast algorithms perform an almost full reconstruction to provide input for various physics filters which classify and select appropriate events. In 1994 the selected events were transferred to an IBM main frame in the DESY computer centre via fibre optic link and stored onto tape cartridges. Since 1995 the events have been transferred directly to the machine where the data reconstruction takes place.

2.3.5 Reconstruction

The events are normally fully reconstructed within a few days after being taken. The ZEUS reconstruction program, ZEPHYR, takes the uncalibrated digitized hits and PMT signals, calibrates them, and converts them into useful objects for physics analyses such as track parameters, and cell energies. The data are organized for easy access into tables made by using ADAMO, a relational entity-based system. Filters are applied to the data during the reconstruction, and filter bits (called DST bits) are assigned, which can later be used to speed up the selection for the offline analyses. The reconstruction is performed on an SGI Challenge multiprocessor machine with 18 cpu's. It normally takes a few cpu seconds on the SGI to reconstruct a single event. The fully reconstructed events, as well as the raw data, are stored on a large high-density AMPEX tape drive. In addition, the entire year's data sample is stored in miniDST format on several hundred gigabytes of hard disk for fast access. These miniDSTs contain in compressed form all the information needed for most analyses.

⁶mostly 4D-35 Personal IRIX workstations

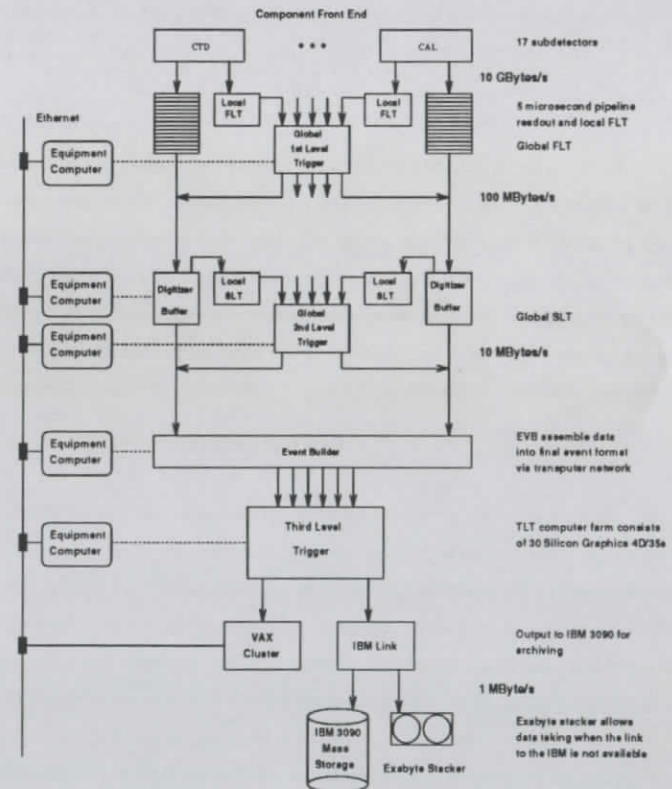


Figure 2.6: Overview of the ZEUS trigger system.

2.4 Data Set

The data are divided into runs, with a run lasting anywhere between a minute and several hours. The runs taken during the 1994 HERA luminosity period can be grouped into three different categories: e^-p , e^+p and shifted vertex, with the bulk of the data from e^+p collisions. A small fraction of the data was taken near the end of the running period with e^+p collisions with the interaction vertex shifted by ~ 70 cm from the nominal vertex position. Taking data with the vertex shifted allows a lower Q^2 to be reached in the DIS analyses.

Data which are found to have been taken when a major system was faulty, e.g. solenoid off, sectors of the CTD off, or too many cells of the CAL dead, are flagged by the routine EVTAK and are not used in the analyses.

Of the 6.2 pb^{-1} of e^+p and e^-p data delivered in 1994 by HERA, ZEUS recorded onto tape 3.7 pb^{-1} . After applying EVTAK, 3.3 pb^{-1} remained. Of the electron data, ZEUS recorded 411 nb^{-1} of which 279 nb^{-1} survived EVTAK. 33 nb^{-1} of positron data were taken with the vertex shifted. A total of 17 million events were recorded by ZEUS during luminosity running in 1994.

2.5 Track Reconstruction

Track reconstruction at ZEUS is performed by the VCTRACK package [50]. Tracks are started from "seeds" in the outer part of the CTD. The seeds are nominally three CTD hits from an axial superlayer, although segments reconstructed in the RTD or hits in the SRTD could also be used in combination with axial CTD hits to form a seed. From a seed, a track trajectory is extrapolated inwards towards the beam line, gathering more axial hits along the way, resulting in a circle in the $x-y$ plane. Z-by-timing information is used and stereo pattern recognition is applied to find a starting z-intercept and polar angle. Stereo hits are then added from the skipped superlayers. By matching the stereo hits to the circle in the $x-y$ plane, z information is obtained because the $x-y$ position of a hit in a stereo wire varies with its z position. Every

track candidate must have either z-by-timing or stereo information. Tracks with too many shared hits are removed; in general, 85% of a track's hits must belong uniquely to the track. The longest tracks are reconstructed first and the succeeding tracks are checked not to duplicate the inner segments of longer tracks already found.

The tracks are fit to a five parameter helix model. Once all the tracks are found, a search for the primary vertex is made. Only tracks which are compatible with originating from the beamline are used. A simple vertex fit is made from the weighted centre of gravity of the remaining tracks and the χ^2 calculated; tracks which contribute too much to the χ^2 are not used. This initial vertex is used as the input into a full vertex fit which can also change the helix parameters of the eligible tracks.

2.5.1 Determination of dE/dx

The energy loss of a charged particle in the CTD gas due to ionization can be determined from the sizes of the pulse hits in the sense wires. If the momentum is not too high, it can be a powerful tool to determine the particle's identity because the rate of energy loss is a function of the particle's velocity and thus can be used to distinguish between particles of different mass. The rate of energy loss by ionization of a heavy particle with charge z travelling at relativistic velocity v through a gaseous medium is given by the Bethe-Bloch formula for which an approximate formula, valid for low energies is given below [52]:

$$-\frac{dE}{dz} (\text{gcm}^{-2}) = \frac{4\pi N_A z^2 e^4 Z}{m_e v^2 A} \left[\ln \left(\frac{2m_e v^2}{I(1-\beta^2)} \right) - \beta^2 - \frac{\delta}{2} \right],$$

where $\beta = v/c$; N_A is Avogadro's number; Z and A are the atomic number and mass of a gas atom; δ is the density effect correction and $I \sim 10Z \text{ eV}$ is the effective ionization potential. A more detailed description can be found in [51]. The relativistic rise can be attributed to the transverse electric field growing with $\gamma = 1/\sqrt{1-\beta^2}$ which increases the contribution from collisions with distant electrons. Eventually when γ reaches a value of several hundred, the *Fermi plateau* is reached where polarization effects, taken into account by the density effect correction, slows the growth and the dE/dx curve

flattens⁷. The curves have a broad minimum around $\gamma = 3$. In this approximation the energy loss is independent of the rest mass of the travelling particle, and varies only with the velocity. Figure 2.7 shows the dE/dx versus momentum distribution of tracks from a single run. The Bethe-Bloch predictions for the pion, kaon and proton bands are also shown.

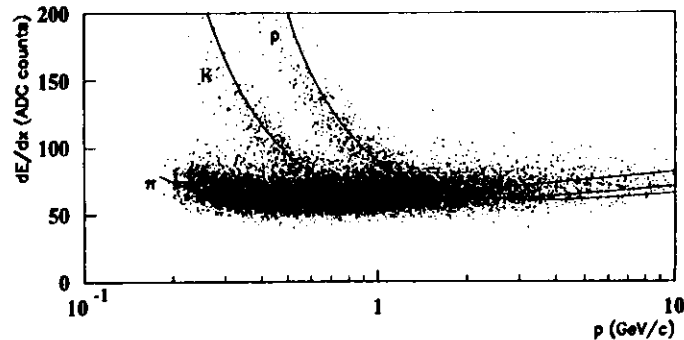


Figure 2.7: The dE/dx of tracks versus momentum from run 10037. The tracks were required to have at least 35 hits contributing to the truncated mean. The momentum dependence predicted by the Bethe-Bloch formula, with an arbitrary scale, is overlaid for the pion, kaon, and proton bands. The bands are clearly distinguishable. The electron band is not visible, but would lie around 75 ADC counts.

Corrections are made to the raw pulse sizes recorded by the CTD to take into account such factors as the track's path length in the cell and individual wire gains. Hits are ignored in the dE/dx measurement if they could have originated from the overlap of two tracks.

The energy loss is dominated by a small number of primary collisions. Fluctuations in the number of these collisions lead to a *Landau* distribution of the energy loss which is not Gaussian, but instead exhibits a long tail towards higher values. Figure 2.8

⁷ The polarization of the medium which limits the extension of the transverse field only slows the relativistic rise. The rest of the rise is accounted for by large energy transfers to a few electrons. The *detected* energy curve flattens if these electrons either escape or travel far enough to be accounted for separately.

shows the Landau distribution from hits belonging to electrons.

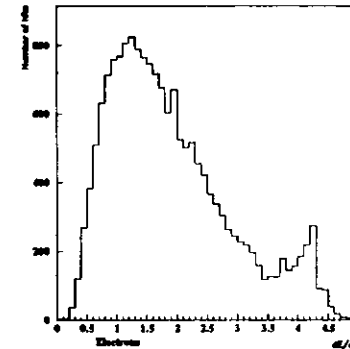


Figure 2.8: dE/dx distribution, scaled by the pion mean dE/dx value, of the individual hits belonging to electron tracks. The sample was taken from elastic $J/\psi \rightarrow e^+e^-$ events with tracks in the polar angle region $1.2 < \theta < 1.9$ rad. The shape is typical of a Landau distribution which has a tail towards higher values. The peak around 4 originates from saturated hits.

Instead of averaging over all the CTD hits, a *truncated mean* is calculated by removing the highest 30% and lowest 10% of hits and averaging over the remainder. From the maximum of 72 hits which could make a full length track, only 42 hits are used to calculate the dE/dx . The truncated mean removes the long tail and makes the distribution behave much more like a Gaussian. The truncated mean gives approximately the same value as the peak of the original Landau distribution.

The dE/dx values are also affected by the overall operating conditions of the CTD which can vary with time. The high voltage settings, which were increased once during the 1994 running period, as well as variations in the pressure and temperature can systematically shift the dE/dx values. The pressure and temperature were monitored throughout the running period, and varied little within a run. The dE/dx dependence on pressure was measured to be about 0.8% per millibar. A natural way to calibrate

the dE/dx is to use the data itself. Since most of the tracks detected in the CTD belong to pions, and the dE/dx of the pion band has a broad minimum between 0.3 and 0.4 GeV/c, they can be used to calibrate the overall dE/dx scale for the CTD on a run to run basis. To determine the dE/dx scale the truncated means of all positive tracks with momentum between 0.3 and 0.4 GeV/c, 22 or more hits in the truncated mean, and a polar angle between 0.7 and 2.4 radians, were histogrammed for every run. A Gaussian was fitted and its mean was used to scale the dE/dx values for that run. The dE/dx values of tracks from data events shown subsequently in this thesis have all been scaled by the appropriate mean pion dE/dx values. The variation of the dE/dx scale with the run number is shown in Figure 2.9. More on dE/dx relevant for this analysis can be found in Appendix A.

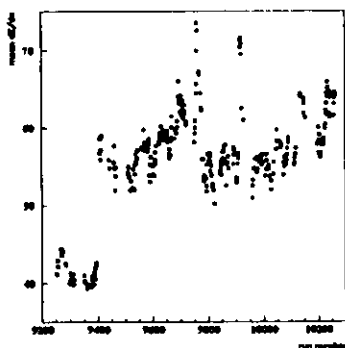


Figure 2.9: Value of the mean dE/dx (in units of ADC counts) for pions with momentum between 0.3 and 0.4 GeV/c versus run number. The large jump in the mean dE/dx around run number 9400 is due to the nominal settings of the CTD high voltage being raised.

Cell Type	Width
EMC	22 MeV
HAC0	27 MeV
HAC1/2	30 MeV

Table 2.2: R.M.S. width of the noise in the CAL measured at the end of the 1994 running period.

2.6 Calorimeter Reconstruction

Every cell has two readouts, one each from the left and right sides. Normally the energy of a cell is calculated as the sum of the two sides. However when one of the two channels is considered bad, usually because the readout is inoperative or too noisy, the energy of the cell can be obtained by using the good channel and multiplying by 2. This redundancy ensures the robustness of the calorimeter data acquisition. Furthermore, on each module the readout chains of the left and right sides of a cell have no common components, limiting the chances that both readouts suffer the same hardware failure. For runs which were accepted by EVTAKE, less than 0.1% of the total cells at any time had both readouts marked bad, in which case the energy of the cell was set to zero.

The calorimeter data was zero-suppressed at the reconstruction level: electromagnetic cells with less than 60 MeV or hadronic cells with less than 110 MeV (100 MeV for HAC0 cells) of energy had their reconstructed energy set to zero. The noise distributions of the calorimeter cells were centred at zero and had typical R.M.S. widths as shown in Table 2.2.

To remove the remaining noisy cells, isolated EMC cells with less than 80 MeV energy or isolated HAC cells of less than 120 MeV energy were removed from the analysis. Since it is very unlikely that both PMTs of a cell are simultaneously noisy, or have sparked⁸, the energy imbalance, $|\frac{E_{left} - E_{right}}{E_{left} + E_{right}}|$, is effective in removing further spurious signals in the CAL. Cells with less than 700 MeV were required to have an

⁸Caused by a spontaneous discharge between the base of the PMT and the shielding around it.

imbalance < 0.7.

2.6.1 Islands

Calorimeter cells with non-zero energy deposits were grouped into objects called *islands*. Islands are designed to correspond to single particles entering the calorimeter. The island algorithm loops over all towers with energy. Each tower points to the neighbouring tower with the most energy. If it has more energy than any neighbour, the tower points to itself. It then becomes the seed of an island. A trail of pointers thus leads every tower uniquely to the seed of some island. All cells in towers leading to an island seed are considered to make up the island. The island algorithm offers the opportunity of separating the energy deposits from two or more incident particles even when the energy deposits are not isolated.

The island position was calculated from the energy weighted average of all the cells belonging to the island:

$$\bar{x} = \frac{\sum \bar{x}_i E_i}{\sum E_i},$$

where \bar{x}_i and E_i are the coordinates and energy of cell i . For islands with most of their energy in the EMC sections, a more accurate algorithm⁹ was used, based upon test beam results on the energy spread of electromagnetic showers and by comparing the energy distribution between the left and right PMTs of the individual cells.

2.7 Analysis environment

Analysis on ZEUS data is conducted by submitting batch jobs to a central server called ZARAH¹⁰ [54]. The server is powered by three SGI multiprocessor machines,

⁹The routine ELECPO[53], which is in the ZEUS analysis utility program library called PHANTOM, was used. It is more selective in which cells are included (generally the eight EMC cells surrounding the EMC cell with the most energy). Also it uses a logarithmically based energy weighting.

¹⁰Zentrale RechenAnlage für HERA Physik

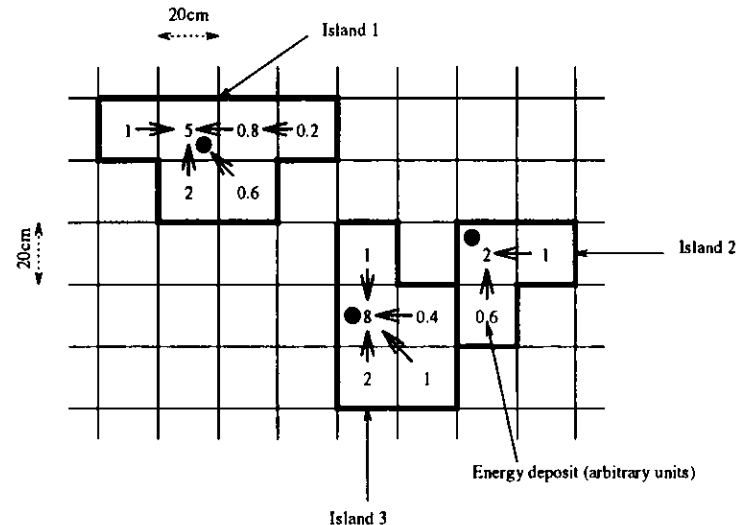


Figure 2.10: An example of the island clustering algorithm. The dots denote towers which are island seeds. The trail of pointers to the neighbouring tower with the most energy is shown by the arrows. The thick black lines delimit the boundary of an island.

of which two (34 processors) are available for running analysis programs. The hard disks storing the data in miniDST format are directly accessible by ZARAH. Access to Monte Carlo events stored in the tape silos and to the raw data on the AMPEX tape drive is also readily available. User defined data structures called *ntuples* used by the physics analysis package, PAW¹¹, are then created and brought back and kept on a local disk. Interactive analysis using the *ntuples*, editing and histogramming is performed on local workstations. Useful routines for analysis developed by ZEUS members are kept in a program library called PHANTOM for use by the entire collaboration.

¹¹ Physics Analysis Workstation project, PAW, is maintained by CERN for use by the High Energy Physics community

Chapter 3

Monte Carlo

The use of Monte Carlo (MC) techniques in simulations plays a large role in any particle physics experiment. Two types of Monte Carlo simulations are generally used in particle physics: event generators which attempt to simulate the results of a physics process, and detector simulations which model the response of the detector to a given physics event input. Combined, they are used for detector design and trigger studies, acceptance calculations and to investigate sources of systematic uncertainties.

3.1 Event Generators

The output of an event generator is a list of particles and their energy-momentum four-vectors. This output should reproduce on average the complex behaviour of real data up to fluctuations arising from the probabilistic nature of quantum mechanics. In MC generators the fluctuations are achieved by subdividing the complete event into a sequence of small steps in which the outcome of each is chosen randomly according to probability distributions.

A key principle behind Monte Carlo QCD event generators is factorization. Factorization means the event generation can be divided into parts which can be done in sequence: the elementary hard subprocess, initial state radiation, final state radiation, and hadronization. In addition, the algorithms for initial and final state

radiation and hadronization should be independent of the hard subprocess.

The hard subprocess is the central element of the event generation and is usually calculated exactly to the lowest order of the perturbative expansion. Parameterizations of the structure functions of the colliding particles are used as input to determine the kinematics of the initial partons. In the case of inelastic J/ψ production the hard subprocess is $\gamma g \rightarrow c\bar{c} \rightarrow J/\psi g$.

The higher order calculations for the hard subprocess are generally too difficult to compute. Instead, higher order effects are taken into account by the parton shower approach which simulates perturbatively, to leading-log accuracy¹, initial state and final state radiation. If we consider only QCD radiation, the partons can undergo the branchings $g \rightarrow gg$, $g \rightarrow q\bar{q}$ and $q \rightarrow qg$ with the new parton taking a fraction z of the original parton energy. The probabilities of these branchings occurring at a virtuality k_T^2 are described by the Altarelli-Parisi splitting functions [55], where k_T is the transverse momentum of the produced partons. The Q^2 scale of the hard subprocess is the highest virtuality scale of the event. At each branching the virtualities of the partons decrease until they reach a cutoff scale, Q_0^2 , where the parton shower stops because $\alpha_s(Q_0^2)$ is too large to continue the perturbative approach. This cutoff is usually around 1 GeV. Most models use coherent showers to take into account destructive interference effects on soft (low k_T) gluon emission by requiring that the branchings are angularly ordered. This means that at each branching the angle between the two emitted partons is smaller than that of the previous branching.

Initial state radiation is done in a similar way to final state radiation, but in reverse. The shower is reconstructed 'backwards' in Q^2 starting from the hard interaction towards the parton which initiated the shower at the cutoff scale Q_0^2 .

At the end of the parton shower the coloured partons must somehow 'dress themselves', i.e. combine to form the colour singlet hadrons which are ultimately seen in

¹The parton shower approach considers terms of the form $\frac{1}{n} \left[\frac{\alpha_s}{\mu} \ln \frac{Q^2}{\mu^2} \right]^n$ where μ^2 is the initial virtuality of the quark or gluon in the proton. These terms are called the leading logs because the logarithms are raised to the same power as α_s .

the detector. QCD inspired hadronization models are used to describe this process in a phenomenological way. The hadronization procedure is assumed to be independent of the hard interaction and initial energy. This means that the phenomenological parameters of hadronization models can be determined by fitting data from different experiments and energies. The Monte Carlos used in this analysis use two different types of hadronization models, the cluster model and the LUND string fragmentation model. Both models convert partons to hadrons locally. Only neighbouring partons which are colour connected interact together to form hadrons. The result is that the event characteristics are mainly determined by the end of the parton shower.

The cluster model takes the outgoing gluons after the perturbative final state radiation and splits them into light quark-antiquark pairs. At this stage colour lines are followed from each quark to an antiquark or diquark with which it forms a colour singlet cluster. The clusters are then decayed isotropically into pairs of hadrons. If a cluster is too light to decay into two hadrons, it is made into a single light hadron and its mass is adjusted by shifting momentum to an adjacent cluster.

The string model, developed at Lund, is incorporated into the JETSET [56] program and is probably the most popular hadronization model. Quarks are believed to undergo linear confinement; i.e. the energy between them increases linearly with distance. This can be modeled as stretching a one dimensional string with string constant, $\kappa \sim 1$ GeV/fm, between them. As the quarks in a colour connected (i.e., colour singlet) $q\bar{q}$ pair move apart, the potential energy stored in the string increases until eventually the string breaks, forming from the vacuum at the breaking point a new $q\bar{q}$ pair. The result is two shorter strings each between a colour-singlet $q\bar{q}$ pair. This continues until the individual strings do not have enough energy to break and only on-mass-shell hadrons remain. A gluon is treated as a kink in the string between a $q\bar{q}$ pair, carrying localized energy and momentum. This string will break along the qg and $\bar{q}g$ pieces, eventually leaving a single hadron around the corner of the string where the kink was.

Three Monte Carlo generators, HERWIG [57], EPJPSI [58] and EPSOFT [59]

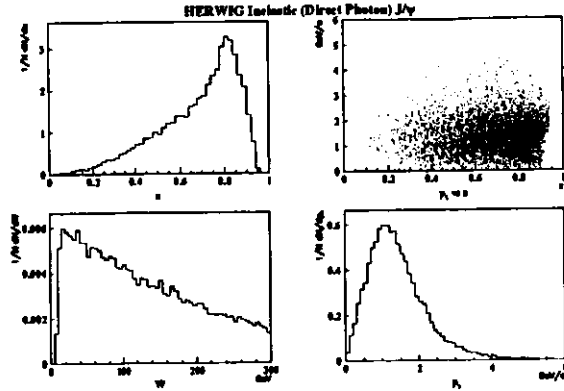


Figure 3.1: Distributions of kinematic quantities for events generated by HERWIG using the colour-singlet model. A cut of $z < 0.95$ was imposed.

were used to simulate inelastic J/ψ production with the colour singlet model and background J/ψ production from resolved photon and diffractive processes. In every case the J/ψ was assumed to be nonpolarized, resulting in an isotropic distribution of the decay electrons. The predicted z , p_t and W of the events are shown in Figures 3.1-3.4 for each process.

3.1.1 Inelastic (Direct Photon)

HERWIG is a multipurpose event generator which uses a cluster model for hadronization. The events generated were restricted to $z < 0.95$ because the generator was unable to produce high z events. The events were generated with the MRSD' proton structure function [5], which has $xG(x)$ behaving like $x^{0.5}$ for low x .

The EPJPSI generator is designed only for the leptoproduction of J/ψ particles. However it can simulate many different processes contributing to J/ψ production at HERA. It uses JETSET for hadronization and does initial and final state radiation like

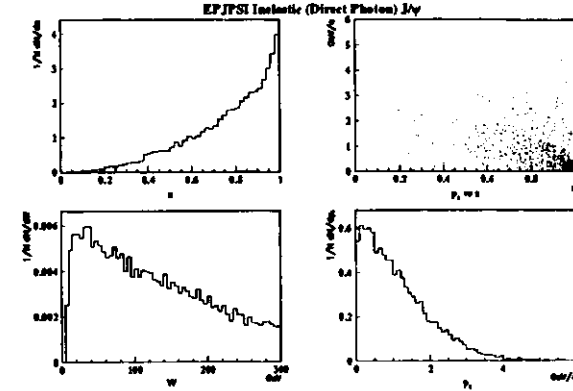


Figure 3.2: Distributions of events generated by EPJPSI using the colour singlet model.

PYTHIA [56]. As with HERWIG, the events were also generated with the MRSD' structure function.

A comparison of the distributions in Figures 3.1 and 3.2 shows significant differences in the z and p_t distributions. The difference between the two generators arises essentially from how they handle parton showering. HERWIG has difficulty to do parton showering for events generated at z near one and with low p_t because the virtuality of the gluon emitted to conserve colour is too low. These events are discarded by HERWIG and a replacement event is generated. EPJPSI, on the other hand, retains the events which cannot undergo parton showering and continues onto the hadronization stage.

3.1.2 Resolved Photon

Resolved photon events of the type $gg \rightarrow J/\psi g$ were generated with the EPJPSI generator using the GRV-HO photon structure function [60] and the MRSD' proton structure function. As seen in the Figure 3.3, resolved photoproduction of J/ψ is

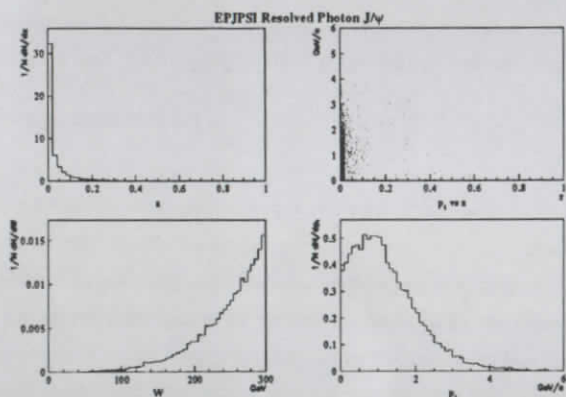


Figure 3.3: Distribution of events generated by EPJPSI with the resolved photon process $gg \rightarrow J/\psi g$.

heavily concentrated in the low z region and can easily be separated from colour singlet events by requiring a lower bound in z .

3.1.3 Proton Dissociation

EPSOFT is a Monte Carlo program designed specifically for simulating soft diffractive and non-diffractive collisions at HERA. It was developed within the framework of HERWIG 5.8. The differential cross section of proton dissociative J/ψ production, $d\sigma/d|t|dM_X^2$, was assumed to be proportional to $e^{-b|t|}$ and M_X^n , where b was varied between 0.4 and 1.6 and n between 2.0 and 2.5². The mass of the nucleonic system, M_X , was generated in the range $(1.25 \text{ GeV})^2 < M_X^2/c^4 < 0.1 W^2$.

²CDF measured the differential cross section for proton dissociation and determined an average value for n to be 2.24 [61]

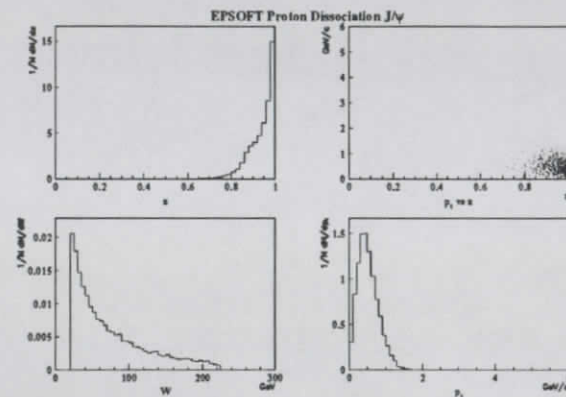


Figure 3.4: Distribution of proton dissociative events generated by EPSOFT with the cross section falling as $e^{-|t|}$ and $M_X^{-2.25} c^2$ in the W range $20 < W < 225 \text{ GeV}$.

3.2 ZEUS Monte Carlo

MC events generated by physics generators are passed through the ZEUS Monte Carlo detector simulation, MOZART. MOZART is based on the GEANT [62] package from CERN³. It simulates the passage of particles through the components of the detector. Energy losses in signal media are converted to digitized hits in the tracking chambers or energy in calorimeters. The parameters of the program are tuned using test beam data, as well as actual ep collisions, to provide an accurate simulation of the ZEUS detector. After MOZART, the events undergo the trigger simulation, CZAR, which simulates the FLT, SLT and TLT. No events are actually discarded, but the results of the filters and vetos are saved in tables. The Monte Carlo data are then reconstructed in the same way as the real data. The final Monte Carlo events are organized for the most part into the same data tables as the HERA data which allows for the same offline analysis code to be run on both.

³Conseil Européen pour la Recherche Nucléaire, the European Laboratory for Particle Physics

3.2.1 FUNNEL

Large samples of Monte Carlo events are needed for every analysis. They must be produced in sufficient quantity that the statistical error incurred is insignificant. Since the events produced for one analysis are often not suitable for another analysis the demand for MC events can grow to be quite large indeed. The production of such large numbers of events as well as the bookkeeping involved to keep track of different software versions can present a major logistical challenge to an experiment. A centrally organized, highly automated system called *FUNNEL* [63] has been developed by *ZEUS* to ensure the orderly and efficient production of MC events.

The event generators are run by the individuals doing a particular analysis. The physics level output of the generators are then submitted to *FUNNEL* which takes care of the detector simulation and event reconstruction. Since most of the time required is taken by the detector simulation, *MOZART* is run in parallel in the background on otherwise idle workstations. *FUNNEL* distributes the physics level events as needed among them and collects back the detector data output which are then sent to dedicated workstations which run the trigger simulation and reconstruction code. The workstations involved are distributed around DESY and outside institutes. Events produced from outside institutes are shipped back electronically over fast networks or on tape through the mail to DESY for central archiving. Several hundred thousand events are typically produced in this manner per week.

3.3 Requirements

This analysis used 60000 *HERWIG* plus 70000 *EPJPSI* inelastic (direct photon) J/ψ events to calculate the acceptance of the selection procedure. These were e^+p events, so only a small fraction contributed to the restricted kinematic region of this measurement. Roughly 10^3 MC events survived the selection procedure described in the Chapter 4, leading to a systematic uncertainty of $\sim 3\%$ due to MC statistics. This was included in the determination of systematic uncertainties presented in Chapter 5.

In addition, 35000 *EPJPSI* resolved photon and 40000 *EPSOFT* proton dissociative events were used to estimate the contamination from these sources in the phase space ($0.4 < z < 0.9$) covered by the measurement.

Chapter 4

Data Selection

4.1 The Trigger Selection

The production of J/ψ 's decaying to an e^+e^- pair can be tagged by looking for evidence of the two decay electrons. The electrons leave tracks in the CTD and energy in the EMC sections of the CAL. Hence the appropriate triggers at the FLT and SLT required that both tracks and electromagnetic energy be present. At the TLT the track and calorimeter energy requirements were combined by matching electromagnetic clusters in the CAL to tracks in the CTD to find the decay electron candidates.

4.1.1 First Level Trigger

The triggers at the GFLT relied mainly on the information from calorimeter FLT (CFLT) and the CTD-FLT to select physics events.

The CFLT [64] summed the charges from the phototubes into trigger tower pulse-heights which were digitized by flash ADC's. The digital values were linearized, stored and used for sum and pattern tests. Calorimeter sums such as total energy, transverse energy, missing transverse energy, and electromagnetic energy were calculated. The sums were recorded as eight bit variables, which led to an energy resolution of

around 200 MeV. Only cells with more than 464 MeV were included in the sums. Each trigger tower consisted of a set of four EMC cells (only 2 in RCAL) plus the HAC1 and HAC2 cells that lie projectively behind the EMC cells.

The CTD-FLT [65] found rudimentary tracks segments by looking for predefined patterns in the CTD, using only the superlayers with z-by-timing information. In 1994 only superlayer one was equipped with the necessary electronics to be used by the CTD-FLT. It classified events by comparing the total number of tracks in an event to the number of tracks pointing to the nominal vertex. In 1994 there were four track categories: REJECT, UNKNOWN, GOOD track and VERYGOOD track. Events with at least one vertex track were called GOOD track events. Events with more than two tracks and which had the number of vertex tracks greater than 0.41 times the number of tracks were called VERYGOOD track events.

Only one FLT trigger, bit 43, which was in fact a general trigger for photoproduction events, was used in the inelastic $J/\psi \rightarrow e^+e^-$ selection because it had the lowest electromagnetic energy thresholds. Unfortunately, the background rate did not allow the thresholds to be set low enough to accept all or even a majority of the inelastic $J/\psi \rightarrow e^+e^-$ events. It had the following requirements:

- GOOD track or VERYGOOD track
- not vetoed by the C5 counter, SRTD, inner or outer VETOWALL
- An OR of the following:
 - Total calorimeter energy sum > 15 GeV, excluding the first three rings of towers around the FCAL beampipe hole, and the first ring around the RCAL beampipe hole
 - Electromagnetic energy sum > 10 GeV
 - Transverse energy sum ($\sum_i E_i \cos\theta_i$) > 11.5 GeV
 - Electromagnetic energy sum in BCAL (EBEMC) > 3.4 GeV

- Electromagnetic energy sum in RCAL (EREMC) > 2.0 GeV, excluding the first ring of towers around the RCAL beampipe hole.

4.1.2 The Second Level Trigger

Most of the events arriving at the SLT were background events originating from collisions between beam particles and gas molecules away from the interaction region, or from cosmic ray muons.

A powerful tool used to remove these events was the time measurement of energy deposits in the calorimeters. The time average of a calorimeter was calculated from all the cells with both PMTs registering more than 200 MeV. Since the time resolution of a PMT improves with increasing energy, PMTs with more energy should have a greater contribution to the time average. The SLT, however, did not have enough time to weight each cell individually. Instead, PMTs with more than 2000 MeV were weighted by a factor of 10. The time measurement of every cell was offset such that energy deposits from particles originating from the interaction point had a time of zero.

Beam-gas events were rejected by requiring that the timing of the calorimeters be consistent with that of an ep interaction (time ~ 0). Events originating from interactions upstream, i.e. in the negative z direction, between the proton beam and gas molecules deposit their energy in RCAL early. They were removed by cutting on the absolute RCAL time ($|\text{RCAL time}| > 8$ ns) and on the difference between the FCAL time and the RCAL time ($\text{FCAL time} - \text{RCAL time} > 8$ ns). Events originating downstream from interactions between the electron beam and gas molecules could be removed by cutting on the FCAL time alone ($|\text{FCAL time}| > 8$ ns). The CAL timing distribution of a sample of events reaching the SLT is shown in Figure 4.1.

Cosmic ray muons were removed by comparing the time in the upper and lower halves of BCAL. These events had a timing consistent with the passage of a single particle from the top to bottom rather than that of particles arriving simultaneously from the vertex.

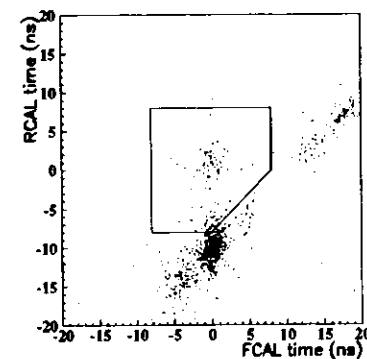


Figure 4.1: The CAL timing distribution of events at the SLT. Events (beam-gas) outside the box (black dots) are rejected by the timing cuts. The cluster of good events centred around a time of (0,0) ns is clearly separated from beam-gas events. However, some beam-gas events are still accepted (in the bottom right corner of the box).

Events triggered by a spark in a single PMT were removed by comparing the energy imbalance between the two PMTs associated with a calorimeter cell.

The quantity $E - P_z = \sum E_i(1 - \cos\theta_i)$ ¹, where the sum is over all cells in the calorimeter, was used to reject non- ep events. Since the maximum value of $E - P_z$ from an ep interaction is twice the electron beam energy, events with $E - P_z > 75$ GeV could be safely rejected.

The following simple filter (bit HFL03) was applied to events which passed the vetos to check for inelastic $J/\psi \rightarrow e^+e^-$ production.

- $P_z/E < 0.92$
- $E - P_z > 4$ GeV
- Sum of electromagnetic energy in BCAL and RCAL > 3 GeV
- VERYGOOD track (from the CAL-FLT)

The relevant calorimeter energy distributions are shown in Figure 4.2 for events reaching the SLT and for HERWIG $J/\psi \rightarrow e^+e^-$ events.

4.1.3 Third Level Trigger

The TLT applied vetos similar to those used at the SLT, but because the time constraints were more relaxed, more sophisticated algorithms could be used before actually selecting events with the physics filters. For example, the calorimeter time was calculated more accurately, with each PMT weighted by the inverse of the square of its estimated uncertainty. Muon events not originating from the interaction region were removed using a combination of track information, the correlation between the time and position of energy deposits in the calorimeter, as well as information from BMUON and VETOWALL [66].

¹For notational simplicity, we will drop the factor of c for formulae combining P and E .

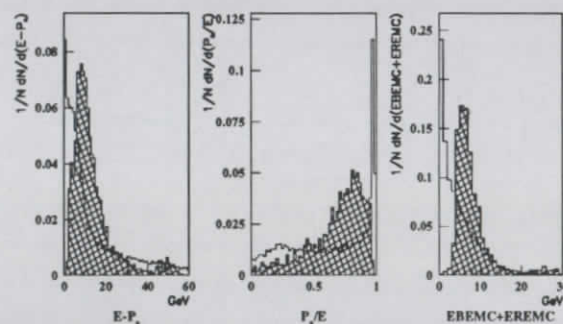


Figure 4.2: Distributions at the SLT for passthrough (unbiased) events and for inelastic $J/\psi \rightarrow e^+e^-$ MC events from HERWIG (hatched histogram). The HERWIG events were required to pass bit 43 at the FLT and have the decay electrons within the CTD.

The main selection of elastic and inelastic J/ψ events was performed by a dedicated J/ψ filter which searched for either of the leptonic decay channels. First, the reconstructed vertex of the event, if it existed, had to have a z position within 75 cm of the origin. If so, the filter would attempt to match tracks to calorimeter islands which were consistent with originating from electrons or muons. To save time at the TLT only events with twenty or fewer tracks were checked. The rest were not accepted by the filter. Monte Carlo simulations showed that this restriction rejects only a small fraction of J/ψ events. Fig. 4.3 shows the TLT track multiplicity of J/ψ events as predicted by HERWIG.

Tracks with $p_t > 0.4$ GeV/c were first extrapolated to the calorimeter, by swimming the tracks through the magnetic field from the edge of the CTD to the face of the calorimeter. Each track was then projected into the CAL with a straight line from its entry point and the closest island within 30 cm of the line was taken to be matched to the track. If the island matched to the track was either electron-like or

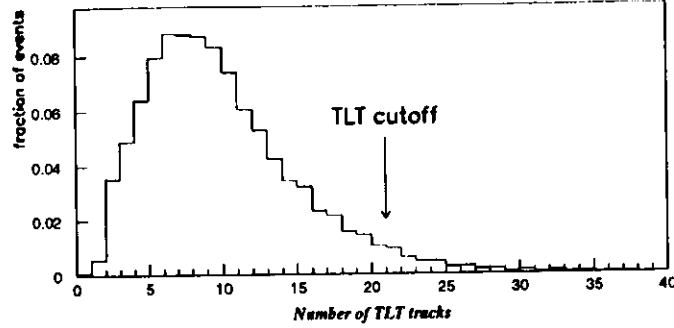


Figure 4.3: TLT track multiplicity of inelastic colour singlet $J/\psi \rightarrow e^+e^-$ events generated by HERWIG with $50 < W_{TP} < 250$ GeV.

muon-like (see below) then the track was treated as a lepton candidate. The invariant masses of all pairs of lepton candidates (either electron-electron or muon-muon) with opposite sign were calculated and if there was a pair with an invariant mass above $2 \text{ GeV}/c^2$, the event was accepted. For events with less than 5 tracks, the mass cut was lowered to $1 \text{ GeV}/c^2$; this accepted events in the low mass tail of the elastic peak.

The requirements for electron-like islands were:

- EMC energy $> 0.3 \text{ GeV}$
- Ratio of EMC energy to total energy $E_{emc}/E > 0.9$
- Number of EMC cells < 9
- Number of HAC cells < 4

Likewise the requirements for muon-like islands were:

- EMC energy $< 3 \text{ GeV}$
- $0.3 \text{ GeV} < \text{HAC energy} < 8 \text{ GeV}$
- $E_{emc}/E < 0.9$

- Number of EMC cells < 5
- Number of HAC cells < 7

4.2 Offline Selection

Events which passed the TLT trigger described above were assigned their own DST bit during reconstruction. The offline selection was restricted exclusively to these events. A preselection was first applied to reduce the number of events to analyze to a manageable level.

4.2.1 Selecting Electrons from J/ψ Decay

In uncovering J/ψ 's from the large combinatorial background, a series of selection cuts combining the calorimeter and tracking information as well as kinematic constraints were used.

Since an electron showers early after entry into the calorimeter, the energy deposition is very localized. Very little energy reaches the HAC layers. Islands were selected on the basis of their radial size and the longitudinal distribution of energy between the EMC and HAC sections. The energy weighted radius, R_{island} , was defined by

$$R_{island} = \sqrt{\sum_{i=1}^3 \left[\frac{\sum_{cells} E_{cell} \cdot x_{i,cell}^2}{E} - \left(\frac{\sum_{cells} E_{cell} \cdot x_{i,cell}}{E} \right)^2 \right]},$$

where $x_{i,cell}$ represents the cartesian coordinates of a particular cell. Because of the low energy ($\sim 2 \text{ GeV}$) of the decay leptons, the sole use of calorimeter information was ineffective in selecting inelastic $J/\psi \rightarrow e^+e^-$ candidates. Pions of the same energy can often leave a similar signature in the calorimeter.

Since the electrons are coming from the decay of the J/ψ , they each have in the J/ψ rest frame half the J/ψ energy, approximately 1.5 GeV . In the lab frame they are expected to have a similarly large p_t . Since most of the background is at low

p_t cuts in the transverse momentum of the decay leptons substantially reduce the background.

The offline requirements for the preselection were similar to the cuts used at the TLT. First, the z position of the vertex had to be within 50 cm of the nominal interaction point. Figure 4.4 shows that in 1994 the distribution of the z position of the vertex was centred at $z = 3.5$ cm and had a width of 10.8 cm, which was approximately half the length of the proton bunch. The search for $J/\psi \rightarrow e^+e^-$ candidates required a pair of opposite signed tracks, each with a $p_t > 0.5$ GeV/c, having hits in either the VXD or SL 1, associated with the vertex and matched with an electromagnetic island cluster. The p_t distribution of the candidate tracks is shown in Figure 4.5 for the preselected data and pure J/ψ Monte Carlo. To be matched, a track, extrapolated in the same manner as by the TLT, had to come within 30 cm of an electromagnetic island which had a radius < 20 cm and at least 90 % of its energy located in the EMC section. Moreover, the momentum of the track and the energy of the island had to agree such that $0.4 < E_{\text{island}}/|p_{\text{track}}| < 1.6$. The distributions for these variables are shown in Figure 4.6. The invariant mass of the track pair, $m_{e^+e^-}$, assuming that they originated from electrons, had to be greater than $2 \text{ GeV}/c^2$.

After the preselection, 87716 J/ψ candidates remained. The individual selection cuts were then tightened: the p_t cut on the tracks was raised to 0.8 GeV/c; the island radius cut was reduced to 16 cm; the track-island distance cut was reduced to 15 cm; and the required electromagnetic energy fraction of the islands was raised to 0.95. In addition, the decay electron tracks were required to be at a polar angle θ such that $|\eta| < 1.5$, where $\eta = -\ln(\tan(\theta/2))$ is called the pseudo-rapidity, so that they would be in a well understood region of the CTD. Since we are interested in inelastic events where a proton remnant is expected, a further requirement was made demanding at least 1 GeV of energy, excluding the islands belonging to the J/ψ candidate, in a 35 degree forward cone in the CAL. This helps remove diffractive-like events as well as completely removing elastic events. Finally, kinematic cuts were imposed on the z and W ranges; dE/dx information was used and a p_t cut was

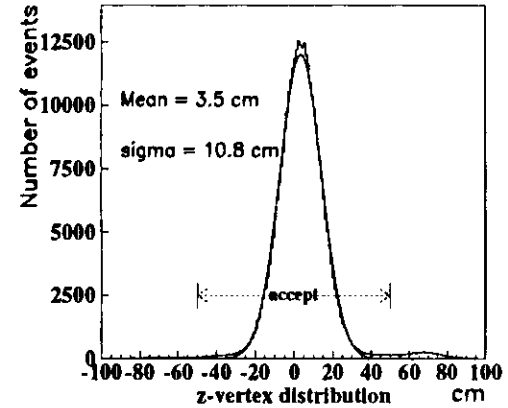


Figure 4.4: The z -vertex distribution of events selected by the J/ψ TLT filter in 1994. A Gaussian fit is overlaid. The bump near $z = 70$ cm is due to the presence of a satellite proton bunch caused by the radiofrequency cavity system.

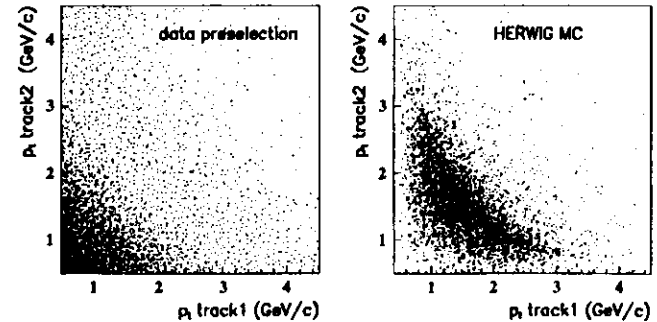


Figure 4.5: A scatter plot of the p_t correlation between the two candidate electron tracks for (left) data after preselection and (right) HERWIG J/ψ MC events. The two plots are shown with arbitrary normalization.

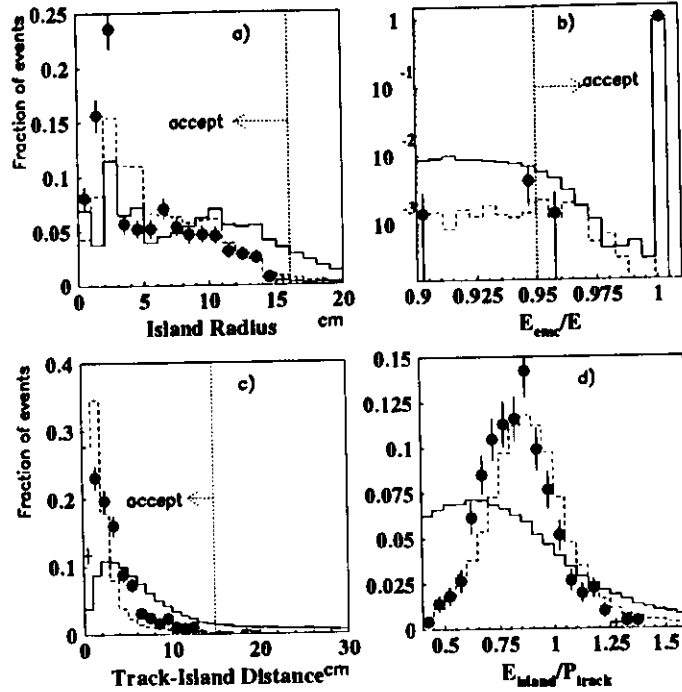


Figure 4.6: Distributions of variables used to find electrons. The solid line is from candidates from data after preselection, the dashed line is from true electrons from HERWIG MC events and the dots are from electrons from elastic J/ψ events in the data. Electrons from elastic $J/\psi \rightarrow e^+e^-$ events are not expected to agree perfectly those from inelastic J/ψ Monte Carlo, but do give an indication of the suitability of the cuts. e.g. in a) the electrons from the elastic J/ψ sample have a relatively smaller radius than those from inelastic processes because they are more often in BCAL which has a smaller EMC cell size than RCAL. In d) the lower E_{island}/P_{track} values are expected because electrons from elastic J/ψ decays have on average less energy than their counterparts from inelastic J/ψ decays. The peak is at less than one because energy is lost in the inactive material between the interaction region and the calorimeter.

Selection cut	Candidates
Stored onto tape in 1994	17×10^6
After reprocessing	8.7×10^6
e^+p data, no shifted vertex	7.6×10^6
DST bit 23 (same as TLT J/ψ bit)	624884
FLT selection bit 43	353510
SLT selection bit HFL03	326479
ep bunch	326366
$ z\text{-vertex} < 50$ cm	319100
preselection	87716
p_t of both tracks > 0.8 GeV/c	29873
Island radius < 16 cm	24406
$E_{ismc}/E > 0.95$	21357
track-island distance < 15 cm	16659
$ \eta $ of both tracks < 1.5	12856
Energy in forward cone > 1 GeV	12315
$z_{rec} > 0.48$	1609
dE/dx of each track > 1.25	281
$105 < W_{rec} < 149$	119
$z_{rec} < 0.9$	78
$p_t (J/\psi) > 1$ GeV/c	48
$z_{rec} < 0.85$	37

Table 4.1: Selection of 94 data.

imposed on the J/ψ candidates. Table 4.2.1 gives an overview of the number of $J/\psi \rightarrow e^+e^-$ candidates surviving after each round of selection cuts. A picture from the ZEUS event display of a typical $J/\psi \rightarrow e^+e^-$ candidate is shown in Figure 4.8.

4.3 Kinematics

The reconstruction of the variables z and W follows the method proposed by Jacquet and Blondel to determine $y = \frac{P_p \cdot q}{P_p \cdot k}$, where P_p, k are the four-momenta of the proton and electron, and q is the four-momentum of the exchanged photon [67]. Since W is the centre of mass energy of the photon-proton system,

$$W^2 = (P_p + q)^2 = m_p^2 - Q^2 + 2P_p \cdot q.$$

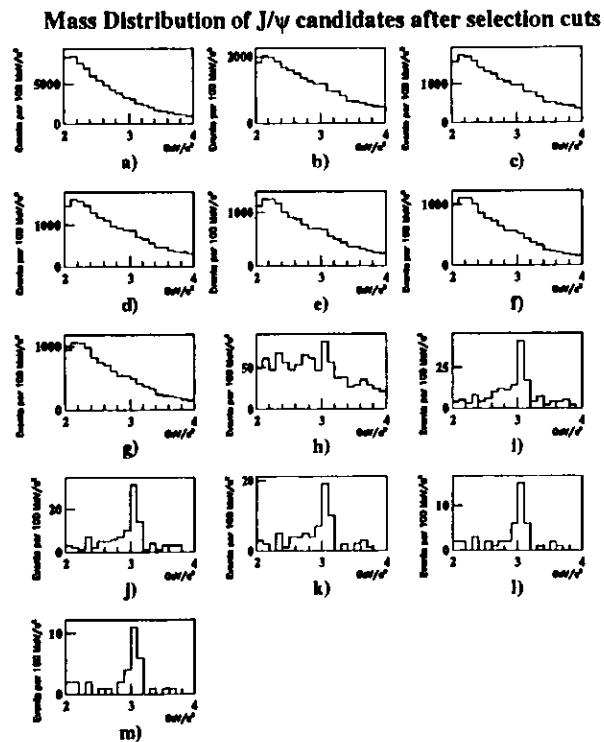


Figure 4.7: Mass distribution of $J/\psi \rightarrow e^+e^-$ candidates after a) the preselection, b) p_t of the electron tracks > 0.8 GeV/c, c) electron island radius < 16 cm, d) $E_{rec}/E > 0.95$ for electron islands, e) track-island distance < 15 cm, f) $|\eta|$ of electron tracks < 1.5 , g) Energy in forward cone > 1 GeV, h) $z_{rec} > 0.48$, i) dE/dx of electron tracks > 1.25 times pion mean, j) $105 < W_{rec} < 149$ GeV, k) $z_{rec} < 0.9$, l) $p_t(J/\psi) > 1$ GeV/c, m) $z_{rec} < 0.85$. The cuts most effective in reducing the background are the lower limit on z and the dE/dx cut.

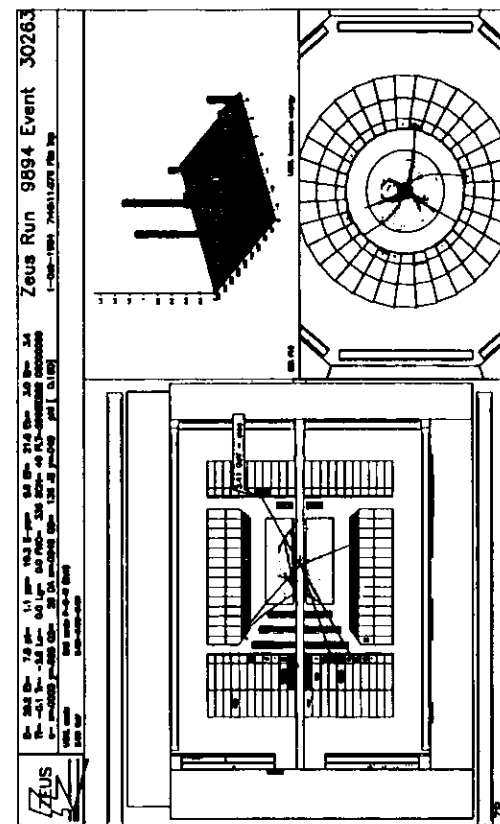


Figure 4.8: A picture of a typical $J/\psi \rightarrow e^+e^-$ event. The display is divided into three parts. The larger one gives a side view of the CAL plus inner detectors. FCAL is on the left and the two rightmost energy deposits are from the decay electrons. The other two views are of the calorimeter transverse energy deposits on a $\eta - \phi$ grid and of an axial view of the CTD and BCAL. Note: the display program automatically assumes that the electron-like island with the largest transverse energy originates from the scattered electron of a DIS event. Since this was not the case, the Q^2 value printed along with other event information at the top of the display is not correct.

Both the mass of the proton and Q^2 are small (photoproduction) leaving us with

$$W^2 \sim 2P_p \cdot q = 2(P_p \cdot k)y = 2(2E_p E_e)y.$$

y can be replaced by y_{JB} (JB for Jacquet-Blondel) with

$$y_{JB} = \frac{(E - P_z)}{2E_e},$$

where $(E - P_z)$ is obtained by summing over all the calorimeter cells. This leaves us with

$$W^2 \sim 4E_p E_e \frac{(E - P_z)}{2E_e}.$$

A similar expression can be obtained for z . However, we can do better than this because two of the islands are matched to the decay electrons from the J/ψ . We can replace the contribution to the $(E - P_z)$ sum from the cells in the islands matched to the decay lepton tracks with the values from the track parameters. Since the track parameters give a better measurement of the energy, this improves the resolution of the reconstructed variables.

$$W_{rec} = \sqrt{2E_p((E - P_z)_{J/\psi} + (E - P_z)_{cal-J/\psi})}$$

and

$$z_{rec} = \frac{(E - P_z)_{J/\psi}}{(E - P_z)_{J/\psi} + (E - P_z)_{cal-J/\psi}}$$

Nevertheless the measured kinematic variables z and W are shifted from their true values due to the energy loss in the inactive material in front of the calorimeter and the escape of particles down the rear beampipe. The shifts and resolutions as determined from the HERWIG Monte Carlo are shown in Figures 4.9 and 4.10.

The z reconstruction suffers from large shifts and poor resolution at low values of z and improves for higher z . The size of the shift varies from almost 20% for the MC generated values of z (z_{gen}) near 0.4 to 6% for z_{gen} near 0.8 to less than 1% for z_{gen} near 0.9. The resolutions on z are respectively 15, 6 and 4%.

The shifts in the W reconstruction are more stable and range from -4% for W_{gen} near 110 GeV to -7% for W_{gen} near 160 GeV. The resolution is constant at 5% over

this range of W . The W_{rec} values of 105 and 149 were chosen to correspond to W_{gen} values of 110 and 160 GeV which is the range where the acceptance was high (see Section 5.2). Figure 4.11 shows the mass distribution with respect to W_{rec} . The range in W_{rec} effectively removes DIS events, because events with a scattered electron in the detector would have a very large W reconstructed value, falling outside the range being considered.

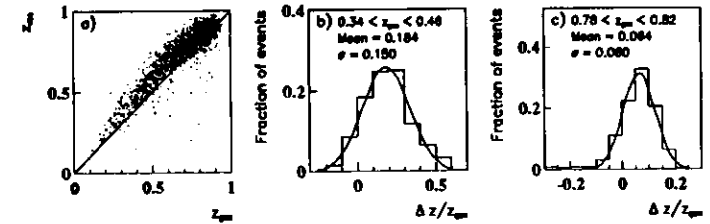


Figure 4.9: z reconstruction of the J/ψ from the HERWIG Monte Carlo: (a) z reconstructed versus z generated (b) $(z_{rec} - z_{gen}) / z_{gen}$ for $0.34 < z_{gen} < 0.46$ (c) $(z_{rec} - z_{gen}) / z_{gen}$ for $0.78 < z_{gen} < 0.82$. The fits shown are Gaussian.

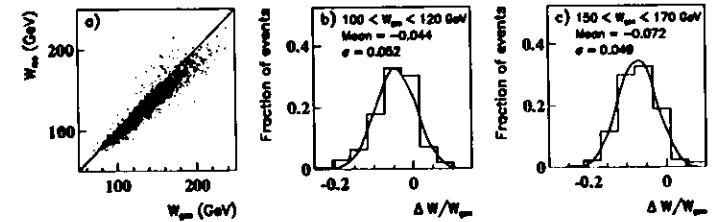


Figure 4.10: W reconstruction of the J/ψ from the HERWIG Monte Carlo: (a) W reconstructed versus W generated (b) $(W_{rec} - W_{gen}) / W_{gen}$ for $100 < W_{gen} < 120$ GeV (c) $(W_{rec} - W_{gen}) / W_{gen}$ for $150 < W_{gen} < 170$ GeV. The fits shown are Gaussian.

The transverse momentum, p_t , of the J/ψ is better reconstructed than z or W because it needs to use only the information from the two tracks of the decay electrons. Figure 4.12 shows the resolution of p_t , which is better than a few percent. The mean p_t is slightly shifted to lower values. This is caused by events where one or more of

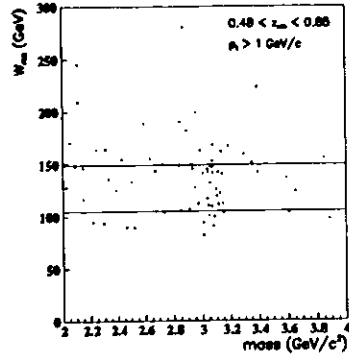


Figure 4.11: W_{rec} versus the mass of the J/ψ candidates. The horizontal lines are at $W_{rec} = 105$ GeV and at $W_{rec} = 149$ GeV.

the decay electrons underwent bremsstrahlung (see next section).

4.4 Signals

4.4.1 Bremsstrahlung fit

As the decay electrons from the J/ψ travel from the interaction point through the material of the beampipe and walls of the tracking detectors it is possible that they radiate photons. Since this occurs before or at the beginning of a track, the momentum determined by the CTD will reflect the energy of the electron after bremsstrahlung and be less than the original momentum it had when the J/ψ decayed. This bremsstrahlung complicates the attempt to fit a function to describe the reconstructed mass spectrum of the J/ψ candidates. Instead of behaving like a simple Gaussian, the mass spectrum also has a tail towards lower masses. The fit function which was used consisted of a Gaussian term plus a bremsstrahlung tail which itself was a Gaus-

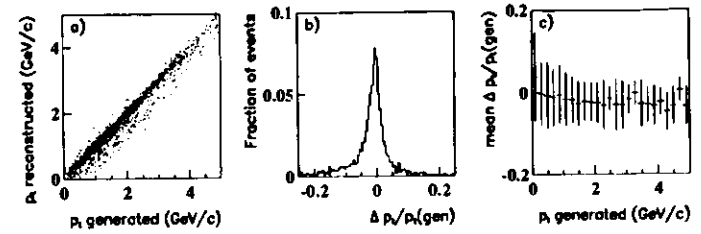


Figure 4.12: p_t resolution of the J/ψ 's: a) p_t of the J/ψ reconstructed versus the generated p_t b) $(p_t \text{ reconstructed} - p_t \text{ generated}) / p_t \text{ generated}$ c) average of $((p_t \text{ reconstructed} - p_t \text{ generated}) / p_t \text{ generated})$ versus p_t generated. The vertical error bars indicate the size of the spread.

sian function convoluted by a bremsstrahlung factor. The bremsstrahlung factor is based on the assumption that only one electron, if any, emits a bremsstrahlung photon with energy E_γ above some cutoff energy E_{min} . The cutoff is necessary because the energy spectrum for bremsstrahlung is known to be proportional to $1/E_\gamma$. The emission of photons with energy less than E_{min} is ignored. Because the emitted photon is practically collinear with the electron, the change in the reconstructed mass is well approximated by E_γ . The fraction of events with a decay electron emitting a bremsstrahlung photon with energy above E_{min} was found from studying Monte Carlo events. The value of E_{min} chosen was 5 MeV, for which f_{tail} , the fraction of the Monte Carlo events which had at least one bremsstrahlung photon was 0.375 [68].

A Gaussian distribution centred at μ with width σ is given by

$$G(m, \mu, \sigma) = \frac{1}{\sigma\sqrt{2\pi}} e^{-(m-\mu)^2/2\sigma^2}$$

The bremsstrahlung tail is then described by

$$B(m, m_{J/\psi}, \sigma) = 1/Norm \int_0^{m_{J/\psi} - E_{min}} \frac{1}{m_{J/\psi} - \mu} G(m, \mu, \sigma) d\mu,$$

where $Norm$ is a normalization factor. In addition to the above function for the real J/ψ signal, a polynomial was included to describe the background.

The complete fit function used was the following [68]:

$$F(m) = f_{J/\psi}((1 - f_{tail})G(m) + f_{tail}B(m)) + (1 - f_{J/\psi})P(m),$$

where $f_{J/\psi}$ is the fraction of the total events coming from real J/ψ 's and $P(m)$ is a polynomial term describing the background. The fit was applied using the maximum likelihood method on the unbinned mass distribution [69]. This is a superior method to the standard χ^2 procedure on a binned sample when there are not many events per bin.

As a check of the validity of the fitting procedure, the fit was applied to the masses from different samples of MC events, each containing 50 true $J/\psi \rightarrow e^+e^-$ MC events which had passed the selection cuts, mixed with a random background of 10 events with masses distributed evenly between 2.4 and 3.6 GeV/c^2 . The distributions of the fit results are shown in Figure 4.13. The mass is correct and the width of signal distribution is expected to be around 30 MeV/c^2 . The average number of events returned by the fit is systematically low by 4% and has a width of 7%. These values can be used to correct the fit results when applied to the data samples and as an estimate of the systematic uncertainty arising from the fitting procedure.

Bremsstrahlung Fit results on Monte Carlo Samples

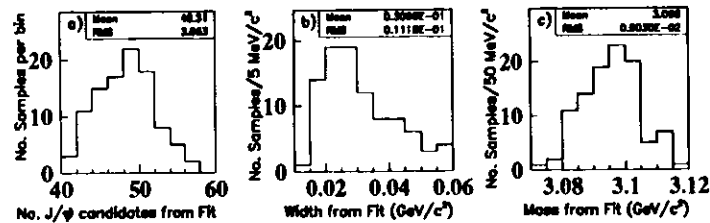


Figure 4.13: Results from the bremsstrahlung fit procedure applied to Monte Carlo samples each with 50 true J/ψ events plus 10 randomly distributed background events all in the mass range between 2.4 and 3.6 GeV/c^2 . a) Number of Signal Events, b) Width of Mass distribution, c) Mass of J/ψ as determined by the fit.

4.4.2 Final Sample

The bremsstrahlung fit was applied after all the selection criteria were applied to the data samples $z_{rec} < 0.9$; $z_{rec} < 0.9$, $p_t(J/\psi) > 1 \text{ GeV}/c$, and $z_{rec} < 0.85$, $p_t(J/\psi) > 1 \text{ GeV}/c$. The results are shown in Figures 4.14, 4.15, and 4.16. In each case the fit was performed in the mass range between 2.4 and 3.6 GeV/c^2 . For the first plot the background was assumed to be a linear function; for the latter two mass distributions a constant background shape was used. The shape of the fits matches the data distributions well. No events had more than one J/ψ candidate after all the selection cuts. The events near the mass peak will be the ones used in Chapter 5 to compare with Monte Carlo predictions. The fitted values of signal events given here will also be used for the cross section determination.

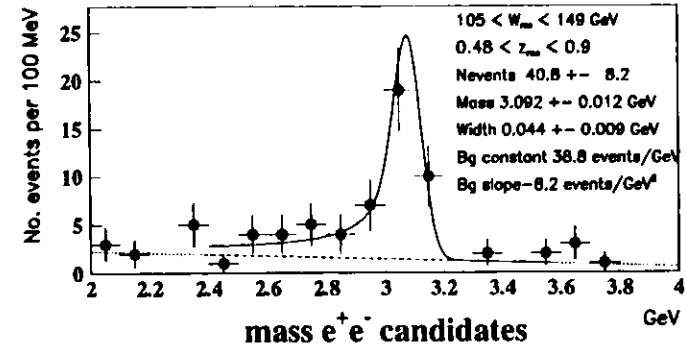


Figure 4.14: Mass distribution of inelastic $J/\psi \rightarrow e^+e^-$ candidates with $0.48 < z_{rec} < 0.9$. The full line shows the result of the bremsstrahlung fit plus background. The dashed line shows the size of the background.

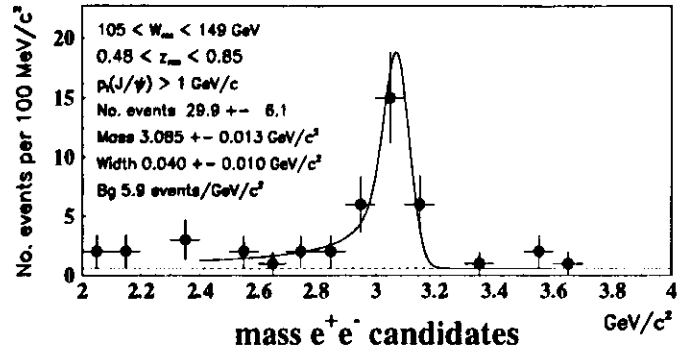


Figure 4.15: Mass distribution of inelastic $J/\psi \rightarrow e^+e^-$ candidates after all cuts and with $0.48 < z_{rec} < 0.9$ and $p_t(J/\psi) > 1$ GeV/c. The full line shows the result of the bremsstrahlung fit plus background. The dashed line shows the size of the background.

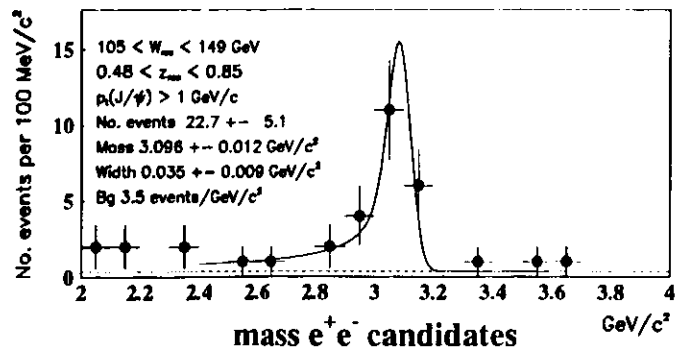


Figure 4.16: Mass distribution of inelastic $J/\psi \rightarrow e^+e^-$ candidates after all cuts and with $0.48 < z_{rec} < 0.85$ and $p_t(J/\psi) > 1$ GeV/c. The full line shows the result of the bremsstrahlung fit plus background. The dashed line shows the size of the background.

Chapter 5

Analysis

Now that a sample of inelastic J/ψ events has been selected it remains to decide what to do with them. Ultimately we wish to calculate production cross sections and compare them to theoretical predictions. To this end we must be able to calculate the effectiveness of our selection criteria, using a combination of Monte Carlo events and data. We also rely on the Monte Carlo simulation to estimate the migration of events into and out of our measurement region and to understand the possible influence of systematic biases due to some arbitrary choice in the analysis procedure.

The acceptance of the selection cuts can be determined for the most part by comparing with Monte Carlo events, except in the case of the dE/dx cut for which real electrons from the data are used. However, before one can reliably use the Monte Carlo simulation to calculate acceptances, one must first be assured that the events generated by it have properties similar to real data events. For example, the simulation of the dE/dx in the Monte Carlo leads to a resolution superior to that found in the data (see Appendix A), which is one reason why real data is used instead. In the following sections, the distributions of various event characteristics are compared with Monte Carlo predictions; the acceptances are calculated and checks are performed to detect possible systematic biases.

5.1 Distributions and Comparison to Monte Carlo

The distributions of the inelastic J/ψ candidates with $0.48 < z_{rec} < 0.9$ and $p_t > 1$ GeV/c, whose masses were shown previously in Figure 4.15, are compared in Figures 5.1 and 5.2 with the predictions from the HERWIG and EPJPSI inelastic J/ψ Monte Carlos, normalized to the number of data events. The same selection cuts used on the data, except for the dE/dx cut, were applied to both Monte Carlos. No dE/dx cut at all was applied to the Monte Carlo events. However, since the efficiency of the cut used is very high (see Figure 5.11) it should not affect any of the distributions. Only events which had a reconstructed J/ψ mass between 2.9 and 3.2 GeV/c² were used. By selecting events from a small region near the mass peak, the signal to background ratio was high. Since the background estimated from the fit was 5.9 events/GeV/c², only 1.8 events of the 27 events in this mass region are expected to have originated from non J/ψ background. The signal to background ratio in this region is thus around 14 to 1. Because of the high purity in this sample, we discount the effects from non J/ψ events to the distributions.

The distributions of the main kinematic variables, W , z and p_t , are all in good agreement with both inelastic Monte Carlos. This supports the hypothesis that these events can be described by the colour singlet model. In addition, the energy distributions in BCAL and RCAL also agree well with the Monte Carlo predictions. They are important because the triggers at the FLT and SLT make use of the BCAL and RCAL energies. There is, however, an excess of low track multiplicity events which could indicate that diffractive mechanisms are contributing to the inelastic signal. Indeed, once we remove the $p_t > 1$ GeV/c requirement on the J/ψ , the discrepancy in the track multiplicity distribution between the inelastic MC's and the data becomes much more prominent (see Figure 5.3). The contribution to the signal from proton dissociation events will be estimated in the following section. Furthermore, as a systematic check, the cross section calculation will also be performed after excluding two track events.

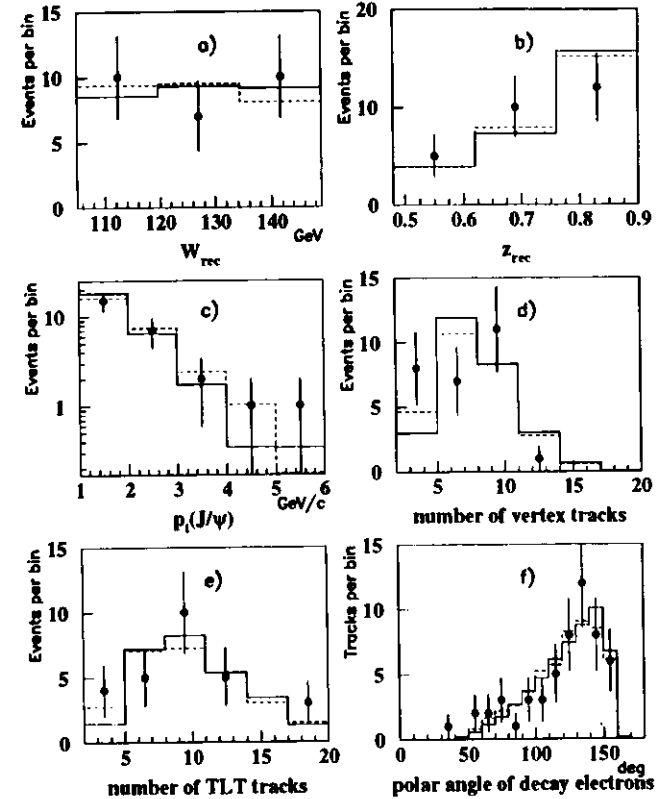


Figure 5.1: Comparison of distributions from data and inelastic colour singlet Monte Carlo. The data, taken from the final sample with $0.48 < z < 0.9$ and $p_t > 1$ GeV/c are represented by the filled circles. The predictions from the HERWIG MC are represented by the solid line histograms, and those from EPJPSI by the dashed line histograms. The plots shown are a) γp centre of mass energy W , b) Inelasticity z , c) J/ψ transverse momentum, d) Number of tracks associated with the vertex, e) Number of tracks reconstructed by the TLT and f) Polar angle of the decay electrons in the laboratory frame.

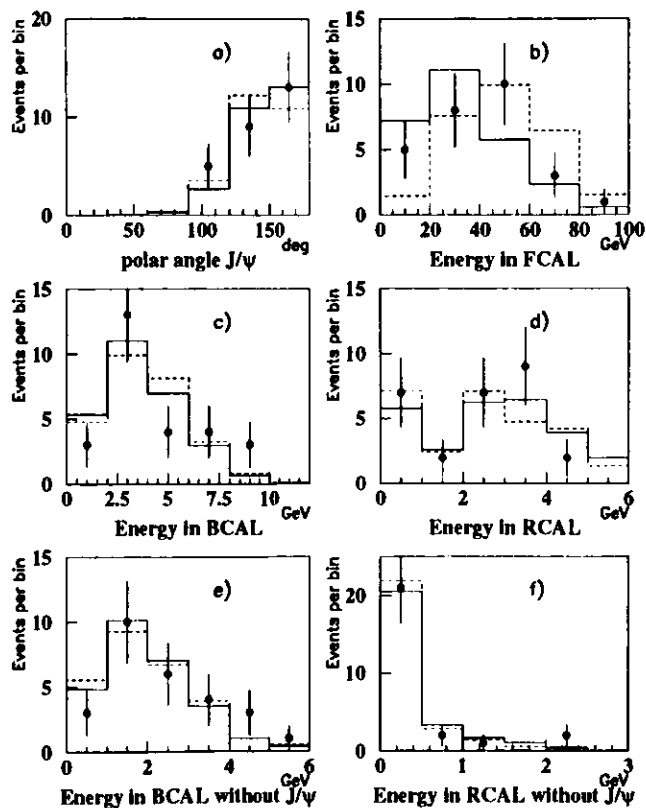


Figure 5.2: Comparison of distributions from data and inelastic colour singlet Monte Carlo. The data, taken from the final sample with $0.48 < z < 0.9$ and $p_t > 1$ GeV/c are represented by the filled circles. The predictions from the HERWIG MC are represented by the solid histograms, and those from EPJPSI by the dashed histograms. The plots shown are a) Polar angle of J/ψ candidate in the laboratory frame, b) Energy deposited in FCAL, c) Energy in BCAL, d) Energy in RCAL, e) Energy in BCAL discounting the deposits from the decay electrons and f) Same as in e) but for RCAL.

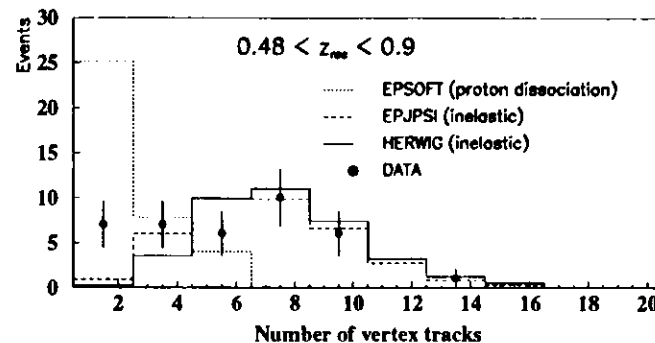


Figure 5.3: Multiplicity of tracks associated with the vertex for candidate J/ψ events with $0.48 < z_{rec} < 0.9$ for data and MC.

5.1.1 Proton Dissociation Contamination

Contributions to the inelastic J/ψ signal from proton dissociation production mechanisms are expected to be significant at high z and low p_t . Although the upper z cut of 0.9 would be effective in removing practically all of the proton dissociation Monte Carlo events at the generator level, it is possible that after reconstruction some proton dissociation data events migrate into the measurement region.

The number of such events was estimated in two ways: a) by counting the number of elastic $J/\psi \rightarrow e^+e^-$ events found after loosening the selection cuts, since a fraction of the proton dissociation events will have the hadronic state escaping detection in the central detector, and b) by examining the distribution of all inelastic J/ψ events with no upper z cut applied and then fitting the z and p_t distributions to a combination of inelastic and proton dissociative Monte Carols. The mass fits to both event samples are shown in Figure 5.4.

In the first method we count the number of elastic $J/\psi \rightarrow e^+e^-$ events, defined by having less than 1 GeV of energy in the calorimeter aside from that associated with the decay leptons, which passed the same inelastic selection cuts, after removing the forward energy requirement, z and p_t cuts and increasing the W range to 40-140 GeV.

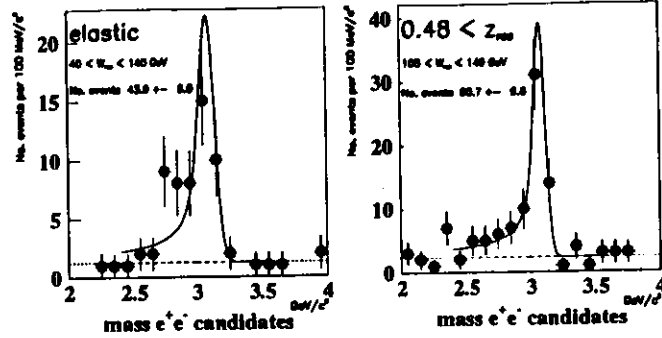


Figure 5.4: Mass distribution of elastic (right) and of inelastic $J/\psi \rightarrow e^+e^-$ candidates with $z > 0.48$ (left). The full line shows the result of the bremsstrahlung fit plus background. The dashed line shows the size of the background.

The bremsstrahlung fit returned 44 ± 9 candidates. ZEUS studies of elastic J/ψ data in the same W range, which also used EPSOFT to describe proton dissociation, determined that the fraction of such events originating from proton dissociation was $30 \pm 5_{-4}^{+7}$ % [70]. We then take EPSOFT Monte Carlo and normalize the number of MC events to match what we would expect to appear as elastic in the data and see how many should then be found by the inelastic cuts. The $e^{-|M|}$ and M_X^2 dependences of the EPSOFT cross section, $d^2\sigma/dt|dM_X^2$, were varied from $b = 1.4$ to 0.6 GeV^{-2} and $n = -2$ to -2.5 . In addition the $E - P_z$ values from the calorimeter were shifted by up to $+70 \text{ MeV}$ to simulate the effect of extra noise in the calorimeter (see Section 5.3). The shift in $E - P_z$ increased the number of proton dissociation events with $z < 0.9$ by about 40%. The results, along with those from the second method are shown in Table 5.1.

For the second method we calculate the combined χ^2 from the comparisons of the z and p_t distributions in the data, shown in Figure 5.5, to distributions obtained by combining various mixtures of inelastic and proton dissociation Monte Carlo. As in the previous distributions, only events with a reconstructed mass between 2.9 and

$3.2 \text{ GeV}/c^2$ are used. Figure 5.6 shows the individual χ^2 results for the z and p_t distributions, whereas Figure 5.7 shows the χ^2 results from the combined z and p_t distributions.

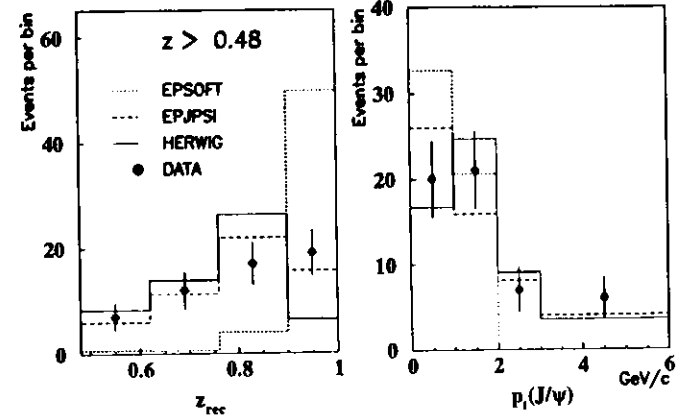


Figure 5.5: The z_{rec} and p_t distributions of the J/ψ candidates for $z_{rec} > 0.48$ are compared with inelastic MC distributions from HERWIG (solid line), EPJPSI (dashed line) and proton dissociation distributions from EPSOFT with the cross section falling as $e^{-|M|}$ and $M_X^{-2.25}$ (dotted line).

The Monte Carlo combination of HERWIG+EPSOFT agrees better with the data than that with EPJPSI+EPSOFT, with the former being insensitive to variations in the p_t and M_X dependences of EPSOFT, whereas the latter prefers a harder proton dissociation part. The fraction of proton dissociation events in the data is determined from the value which gave the lowest χ^2 . The 1σ uncertainty is determined by the range of values for the fraction of proton dissociation which agrees well enough with the data such that the χ^2 values are within the 65 % confidence level for the 6 degrees of freedom. Thus the fraction of the total number of inelastic events with $z > 0.48$ originating from proton dissociation is estimated by this method to be 28 ± 12 %. A comparison of the resulting z and p_t distributions with the data is shown in Figure 5.8.

Both methods agree well with one another. Since the values from the second

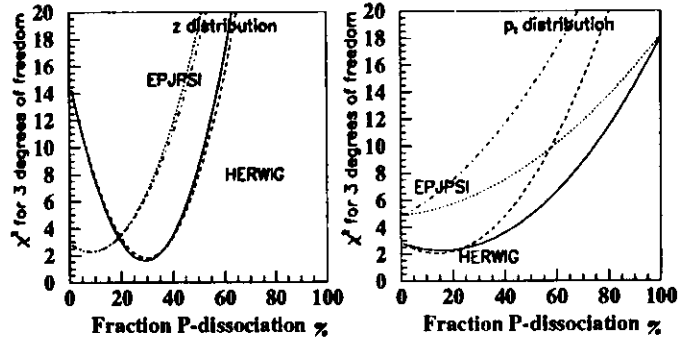


Figure 5.6: χ^2 values from the comparison of the data distributions for z and p_t with a Monte Carlo mixture of either HERWIG+EPSOFT or EPJPSI+EPSOFT. The solid and dashed lines are from HERWIG+EPSOFT mixtures. The cross section dependence of EPSOFT on t and M_X were varied; the former had $b = 1$, $n = -2.25$; the latter had $b = 0.6$, $n = -2.0$ and its $E - P_z$ values shifted by $+70$ MeV to simulate extra noise in the calorimeter. The corresponding mixtures with EPJPSI instead of HERWIG are represented by the dotted and dot-dashed lines respectively.

method were determined by examining the distributions of the actual events involved in the cross section measurement, they will be used later on in this analysis to statistically subtract the proton dissociation contribution from the inelastic cross section.

5.2 Acceptance Calculation

The *acceptance* is used to determine how many events of given type actually occurred from the number of events found in the analysis. To calculate acceptance, one normally divides the relevant kinematic regions into bins. One counts the number of events generated by the Monte Carlo in a particular bin and the number of MC events reconstructed in a corresponding bin of reconstructed variables. The ratio of the latter over the former gives the acceptance. However, some of the events generated in a particular bin are reconstructed in other bins because the variables are not perfectly measured. This *migration* is generally unavoidable. Migration decreases

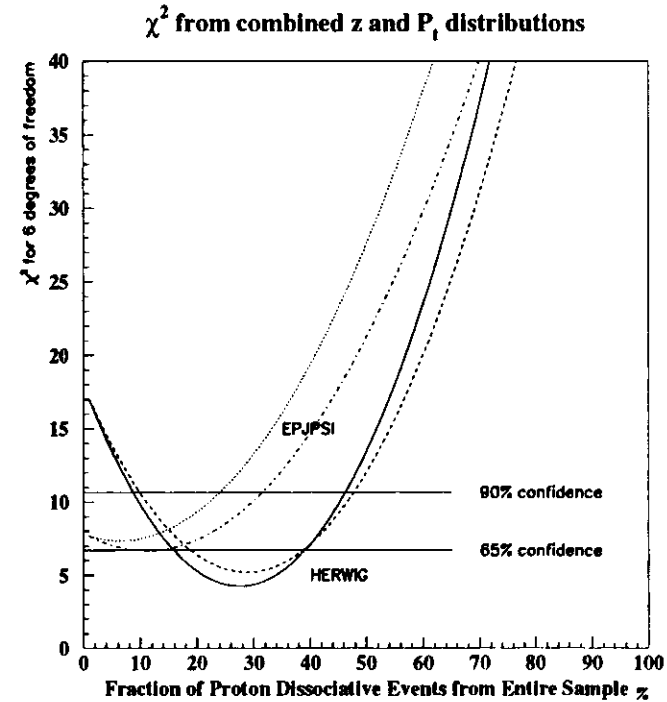


Figure 5.7: χ^2 values from the combined comparison of the data distributions for z and p_t with Monte Carlo mixtures of HERWIG+EPSOFT and EPJPSI+EPSOFT. The solid and dashed lines are from HERWIG+EPSOFT mixtures. The cross section dependence of EPSOFT on t and M_X were varied; the former had $b = 1$, $n = -2.25$; the latter had $b = 0.6$, $n = -2.0$ and its $E - P_z$ values shifted by $+70$ MeV. The corresponding mixtures with EPJPSI instead of HERWIG are represented by the dotted and dot-dashed lines. Lines showing the χ^2 values for 65% and 90% confidence are also shown.

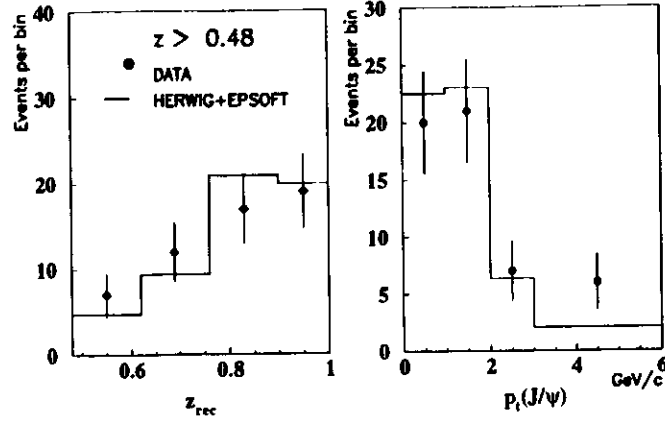


Figure 5.8: The z_{rec} and p_t distributions of the J/ψ candidates for $z_{rec} > 0.48$ are compared with MC distributions from the combination of HERWIG (72%), plus EPSOFT (28%) whose cross section falls as $e^{-|t|}$ and $M_X^{-2.25}$.

Kinematic Range	Expected number of Proton Dissociation events in Signal	
	Elastic J/ψ extrapolation	z and p_t distributions
$0.4 < z < 0.8$ $p_t > 1$ GeV/c	$0.2 \pm 0.1 \pm 0.1$	$0.4 \pm 0.1 \pm 0.2$
$0.4 < z < 0.9$ $p_t > 1$ GeV/c	$0.5 \pm 0.3 \pm 0.1$	$0.8 \pm 0.2 \pm 0.3$
$0.4 < z < 0.9$	$0.9 \pm 0.3 \pm 0.2$	$1.3 \pm 0.3 \pm 0.6$

Table 5.1: The number of proton dissociation events expected to have migrated into the measurement region as determined by extrapolating from an elastic J/ψ sample and by comparing the z and p_t distributions. The values were determined by taking the average of the two extremes of the EPSOFT Monte Carlo, one with $b = 0.6$, $n = -2.0$ and shifting $E - P_t$ by 70 MeV, the other with $b = 1.4$, $n = -2.5$. The errors given are systematic; the first is determined by varying the t and M_X dependence of the EPSOFT Monte Carlo and the second is from the uncertainty in the proton dissociation fraction. The statistical errors on the values are 20% for the first column and 16% for the second, in both cases coming from the bremsstrahlung fits of Figure 5.4.

the *purity*, which is the ratio of the number of events reconstructed in a bin and originating from the same bin to the total number of events reconstructed in the bin. A low purity increases the sensitivity of the measurement to differences between the distributions in the data and those from the Monte Carlo. Another term should also be properly introduced, the *efficiency*, which, in this case, is defined as the number of events generated in a given bin and reconstructed in the same bin over the total number generated in that bin. Then the acceptance is the ratio of the efficiency over the purity. So, if there were no migration, the efficiency and the acceptance would be the same.

The reconstructed bins need not be identical to the generator level bins. Indeed, if the Monte Carlo simulation were to reproduce the data distributions perfectly, it would not matter what the reconstructed bins were. But since it is not usually the case, one tries to choose reconstructed bins which minimize migration effects, and maximize simultaneously the purity and efficiency. If there were no shifts in the reconstruction of the variables, it would be a natural choice to use the same bins for both the reconstructed and generated variables. Since the z and W reconstruction do shift on average, we see how much the generated bin edges shift after reconstruction and use those values for the reconstructed bins. This is equivalent to first finding a function to correct the reconstructed z and W values and then choosing the same bins for the corrected reconstructed values, because only the corrections for the values of the end points of the bins need to be known.

However, to first choose the generator bins it is useful to look at efficiencies without any migration effects. The three most important kinematic quantities which define the phase space in which the J/ψ is measured are the inelasticity z , the photon-proton centre of mass energy W , and the J/ψ transverse momentum p_t . By using the generated kinematic values in the Monte Carlo instead of the reconstructed values for W , z and p_t , we can disentangle migration effects from the efficiency. Figure 5.9 shows the dependence of the efficiency of the selection cuts on W , z and p_t . Since the efficiency of the dE/dx cut is determined from data alone, it was not included

in the cuts used for Figure 5.9. The plots show that the efficiency peaks around $W = 140$ GeV and that it increases with higher p_t of the J/ψ . It is fairly flat in the z region $0.4 < z < 0.9$, dipping slightly at very high z . Both Monte Carlos show similar efficiencies with respect to the kinematic variables. The shape of the W efficiency plot can be understood by examining Figure 5.10. There the efficiencies of the selection process are shown as first the FLT, the SLT, the η cut on the tracks, and finally the TLT cuts are applied. The low efficiency at low W is a direct result of the FLT bit, which requires EMC energy in BCAL and/or RCAL. Remember, W is related to $E - P_z$, which gets large with energy in the rear direction. The SLT bit is 100% efficient at high W , but the $E - P_z > 4$ GeV requirement corresponds roughly to removing events with $W < 80$ GeV. The η requirement on the decay lepton tracks removes most of the high W events, leaving the region of highest efficiency at moderate values of W .

The acceptances, efficiencies and purities, excluding the dE/dx cut, are shown in Table 5.2. Since the results from the previous section have shown that the z and p_t distributions from HERWIG, when combined with EPSOFT, describe the data better than EPJPSI with EPSOFT, the corresponding values are also presented after reweighting the z and p_t distributions of EPJPSI to agree with those of HERWIG. Furthermore, since the reconstruction of z and W is affected at values of Q^2 where the scattered positron deposits all or part of its energy in RCAL, a proper comparison of the two Monte Carlos can only be made by restricting the Q^2 range of the virtual photon in HERWIG such that the scattered positron is assured not to interact with the calorimeter. When comparing $Q^2 < 0.1$ GeV² HERWIG events with reweighted EPJPSI events, the EPJPSI events have an acceptance 5-8% higher than the HERWIG ones, depending on the region measured. These values will later be used as the systematic uncertainty in the cross section arising from the use of a different MC generator.

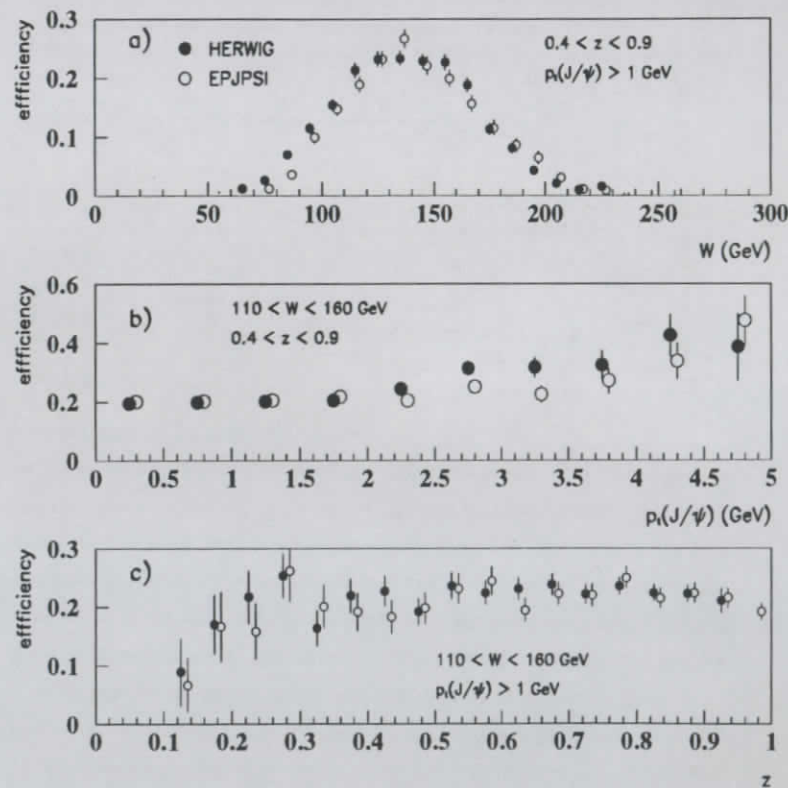


Figure 5.9: The selection efficiencies (excluding dE/dx cut) dependence on the kinematics of J/ψ production according to the Monte Carlos. The open circles representing EPJPSI are offset slightly to the right of their proper positions. The generated values for W , p_t and z were used. Efficiencies are given in a) for $0.4 < z < 0.9$, $p_t > 1$ GeV/c; b) $0.4 < z < 0.9$, $110 < W < 160$ GeV, and c) $110 < W < 160$ GeV, $p_t > 1$ GeV/c. The dE/dx cuts were not used.

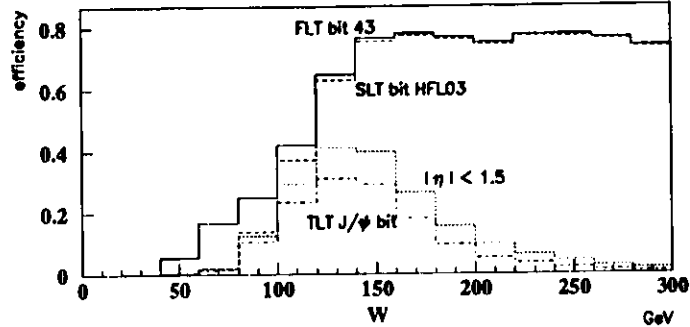


Figure 5.10: Efficiency of the trigger and track angle cuts applied to the HERWIG J/ψ events at the generator level. The full line represents the efficiency of the FLT bit 43 with W . The dashed line is with the SLT bit HFL03 added, the dotted after applying an η cut on the decay electron tracks and the dot-dashed line also includes the TLT J/ψ bit.

Kinematic Range	HERWIG			EPJPSI		
	Acceptance	Purity	Efficiency	Acceptance	Purity	Efficiency
$0.4 < z < 0.8$ $p_t > 1$ GeV/c	19.1 %	73 %	14.5 %	22.0 %	73 %	16.8 %
$0.4 < z < 0.9$ $p_t > 1$ GeV/c	17.1 %	85 %	15.1 %	20.3 %	79 %	16.6 %
$0.4 < z < 0.9$	17.1 %	87 %	15.6 %	19.8 %	80 %	16.4 %
	HERWIG $Q^2 < 0.1$ GeV ²			EPJPSI z, p_t reweighted		
$0.4 < z < 0.8$ $p_t > 1$ GeV/c	20.1 %	73 %	15.1 %	21.7 %	74 %	16.7 %
$0.4 < z < 0.9$ $p_t > 1$ GeV/c	17.9 %	84 %	15.7 %	18.9 %	84 %	16.4 %
$0.4 < z < 0.9$	17.9 %	87 %	16.3 %	18.9 %	86 %	16.9 %

Table 5.2: Acceptances, purities and efficiencies for $110 < W < 160$ GeV as determined by Monte Carlo.

5.2.1 dE/dx Efficiency

The efficiency of selecting tracks with a dE/dx value of 1.25 times the pion mean dE/dx value was determined for electrons from the elastic $J/\psi \rightarrow e^+e^-$ and photon conversion samples described in appendix A. The fraction of electron tracks having a dE/dx value greater than 1.25 times the pion mean value is shown in Figure 5.11. Since the points are evenly distributed within the band between 92% and 98% for most values of the polar angle θ , the efficiency is estimated to be $95\% \pm 3\%$ per electron. The efficiency, when applied to a pair of electrons, is then $90\% \pm 4\%$, assuming that the efficiency estimates are independent for the two electrons. There is also an indication of a small dip in efficiency for forward tracks, but the effect would be smaller than that covered by the given uncertainty in the dE/dx efficiency since most of the tracks are in the rear direction.

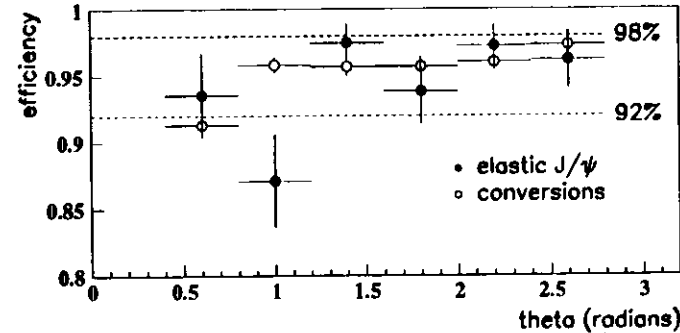


Figure 5.11: Efficiency of requiring the dE/dx of an electron candidate to be greater than 1.25 times the pion mean value versus the polar angle of the track.

5.2.2 Calorimeter Thresholds

The Monte Carlo simulation uses a well defined algorithm to calculate the calorimeter trigger sums. However, in the data the calibration of the analog devices which produce the sums are not as well fixed and the online sums produced by the hardware can differ

from the values calculated by ZGANA (part of CZAR), the simulation program for the FLT. Instead of the efficiency being a sharp step function at the energy threshold (the default case in the Monte Carlo), the efficiency in the data for a given CFLT cut follows a threshold curve, which goes smoothly from 0 at low energy to 1 at high energy. The shapes of the calorimeter thresholds curves were calculated by using real events which were topologically similar to the Monte Carlo events. A sample of events which passed the FLT and accepted by some trigger other than the electromagnetic energy triggers EREMC and EBEMC was selected. We selected events accepted by at least one of the following subtriggers of the FLT: a luminosity monitor tag, $E_{CAL} > 14$ GeV, $E_{EMC} > 10$ GeV, or $E_t > 11$ GeV. In addition, they had to be accepted by the initial J/ψ preselection offline. ZGANA was run on these events and offline values for EREMC and EBEMC were determined. By histogramming the offline EREMC values for all the events in the sample and for those whose online energies passed the online cut, a trigger efficiency could be determined for a given offline EREMC energy by dividing one histogram by the other. The same was done for EBEMC. The resulting efficiency curves are shown in Figure 5.12.

The event weight, $wght$, which gives the probability that an event would be accepted by an OR of the EREMC and EBEMC subtriggers, is given by

$$wght = 1 - (1 - bprob) * (1 - rprob),$$

where $bprob$ and $rprob$ are the efficiencies given by the above curves for the ZGANA energies EBEMC and EREMC of the event. Although the trigger bit used at the FLT included other calorimeter triggers, the J/ψ events which passed the trigger were all accepted by either the EBEMC or EREMC subtriggers. Hence it suffices to consider only these two subtriggers. The event weights were applied to the Monte Carlo and the efficiency was recalculated. With the use of the threshold curves the efficiency increased by 10%, averaged over the W range measured, compared to that obtained using a step function from 0 to 1 at the threshold value. The effect of threshold curves has already been included in all the Monte Carlo histograms shown.

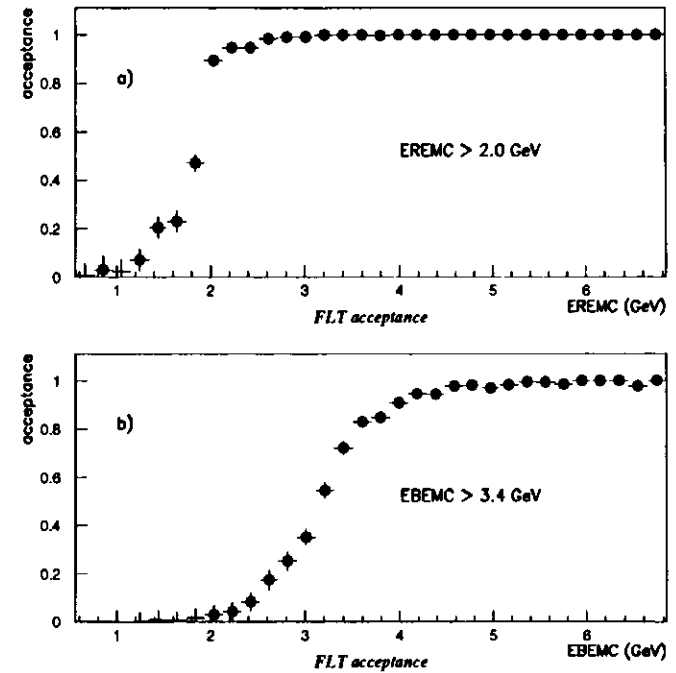


Figure 5.12: The online CFLT threshold efficiencies for a) EREMC > 2.0 GeV and b) EBEMC > 3.4 GeV triggers. The energies along the horizontal axes are the offline reconstructed ZGANA energies.

5.3 Systematic Studies

The selection criteria were each individually varied and applied to both the data and Monte Carlo. The cross section was recalculated with each changed cut to check the stability of the cross section measurement with regards to the selection cut. Ideally, if the Monte Carlo perfectly simulates the data, any variation of the selection criteria should have no influence on the cross section measurement.

The systematic uncertainties due to the selection procedure are grouped into two categories, one for cuts related to the track-island matching procedure, and one related to the cuts applied to the tracks themselves. Two further groupings reflecting the faithfulness of Monte Carlo's description of the data are used, one for the W and z reconstruction, and another for the dependence at the generator level. A final category deals with the resonance background from diffractive processes. The categories are somewhat arbitrarily organized, but the idea was to group sources of systematic uncertainty which are related to one another. Normally, when sources of uncertainty are uncorrelated, the total size of the uncertainty is obtained by adding in quadrature. Instead, we take the largest uncertainties in both the positive and negative directions of all the cuts within a category as the total uncertainties for all the cuts contained within. The systematic studies are summarized in Figure 5.14.

The following sources of systematic biases were considered, grouped into the four categories:

Track-Island matching:

- The required E_{emc}/E ratio of the electron islands was changed from $E_{emc}/E > 0.95$ to $E_{emc}/E > 0.9$ and to $E_{emc}/E > 0.99$.
- The limit on the track-island distance was varied from 20 to 25 and 10 cm.
- The island radius requirement was changed from $radius < 15$ to $radius < 20$ and $radius < 12$ cm.
- E_{island}/P_{track} requirement was changed from $0.4 < E_{island}/P_{track} < 1.6$ to

$$0.6 < E_{island}/P_{track} < 1.4.$$

Tracking:

- The minimum p_t requirement applied the lepton tracks was changed from 0.8 GeV/c to 0.7 and 0.9 GeV/c.
- The η range of the tracks from the decay electrons which were accepted was changed from $|\eta| < 1.5$ to $|\eta| < 1.35$ and $|\eta| < 1.75$.
- The limit in the number of TLT tracks was changed from 20 to 15.

W and z reconstruction: The W_{rec} and z_{rec} ranges were chosen to correspond to the W and z ranges which we wished to measure. The reconstruction of W and z makes use of the Jacquet-Blondel method which uses the quantity $E - P_z$ summed over the calorimeter cells, with the contribution of the cells associated with the decay lepton replaced by the relevant track parameters. A small shift in the W determination is not likely to be a problem because the acceptance and distribution are fairly flat in the W region measured. The z acceptance is also flat. However, since the z distribution rises sharply, a small shift in the z determination can lead to a significant shift in the calculated cross section.

- CAL energy scale: All calorimeter energies were varied by $\pm 3\%$. This had no effect on the track-island matching and affected mainly the W and z determination.
- Calorimeter noise: The amount of noise remaining in the calorimeter cells after the noise suppression cuts affects the amount the reconstructed z and W values shift from their true values. Figure 5.13 shows how much the noise contributes to the $E - P_z$ sum. Although the shapes are similar, the data show a longer tail. The mean differs by 70 MeV. The influence of excess noise was checked by adding 70 MeV to the $E - P_z$ sum for MC events. Although a simple shift is not the ideal solution, it should be sufficient to give us an idea of the sensitivity of the measurement to excess noise in the CAL.

Monte Carlo Dependence:

- The uncertainty attributed to using only a finite number of Monte Carlo events to determine the acceptance was $\sim 3\%$.
- The dependence of the acceptance on the Monte Carlo generator used was checked by using EPJPSI instead of HERWIG. As described in Section 5.2, the EPJPSI events were reweighted and the effect of differences in the scattered positron corrected.
- The MC events were reweighted to match the distributions from using a different proton structure function, MRSD₀' [5]. Unlike MRSD₀' which predicts a rising gluon density with low x , MRSD₀' parameterizes the shape of gluon density to be flat at low x . It affects the generated W and z distributions.

Diffractive Contribution:

- The errors associated with the number of events expected to have originated from proton dissociation were used (see Table 5.1).
- Events with only two vertex tracks were removed and the cross section recalculated. The change in the cross section was adjusted by the number of events already attributed to proton dissociation and subtracted in the original calculation.
- The amount of energy required in the forward region, excluding the contributions from the J/ψ itself, was increased from 1 to 5 GeV. The change in cross section was adjusted as above.

The following other sources of systematic uncertainty were considered:

- dE/dx : Two different samples of electrons from the data, photon conversions and elastic $J/\psi \rightarrow e^+e^-$ events, were used to determine the efficiency of the dE/dx cut for a single electron (see Section 5.2.1). From the variation of the

efficiency with the track's polar angle a total uncertainty of 4% was estimated for the efficiency of the cut when applied to both electrons.

- According to the Monte Carlo results on the fitting procedure (see Fig. 4.13), the fit is systematically low by 4% and has an uncertainty of 7%. The 4% was absorbed into the acceptance calculation.
- Luminosity: A detailed study of the luminosity measurement in 1994 [71] estimated the uncertainty in the luminosity measurement to be 1%.
- Branching ratio: According to the Particle Data book [51], the uncertainty of the $J/\psi \rightarrow e^+e^-$ branching ratio is 4%.

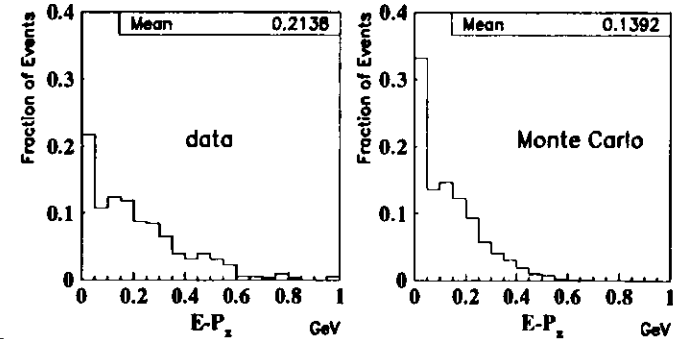


Figure 5.13: $E - P_x$ distribution of the calorimeter cells from elastic J/ψ events after excluding the cells associated with the decay leptons. The remaining cells should correspond to the contribution from the calorimeter noise. The plots are shown for data and Monte Carlo events from the DIPSI [72] generator (a MC generator for elastic J/ψ events).

5.3.1 Additional Checks

The contribution of the resolved photon process $gg \rightarrow J/\psi X$ in this kinematic region was checked using the EPJPSI Monte Carlo. Using the ep cross section calculated by the Monte Carlo and the total luminosity of the data, the expected number of resolved

Systematic Uncertainties

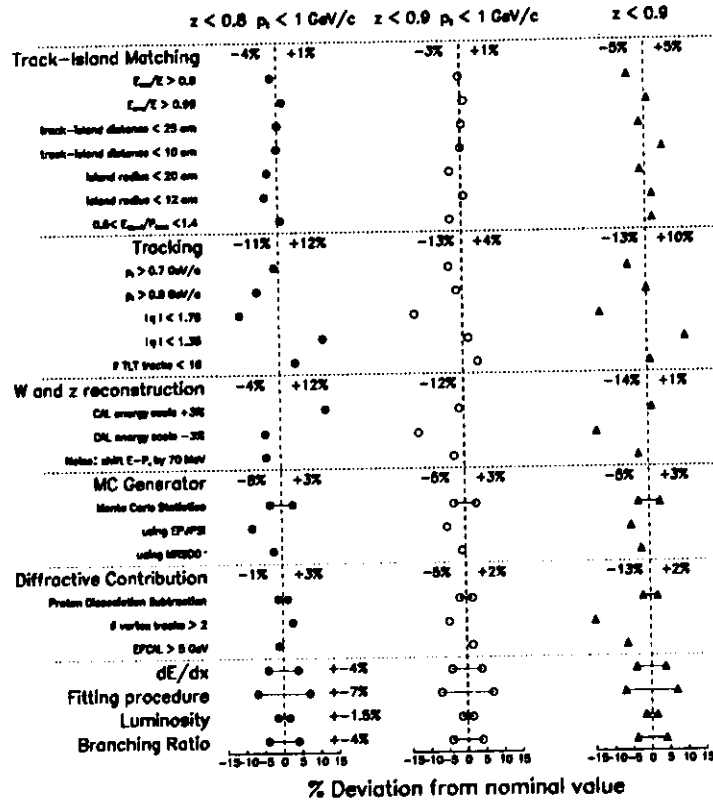


Figure 5.14: Estimates of the systematic uncertainties associated with the cross section measurements. The selection cuts were slightly modified and the difference in the resulting cross section are plotted here. Cuts which could be construed as being correlated to some degree with one another are grouped together; the largest percent difference (shown on the line describing the category) is used for the size of the uncertainty pertaining to that group of cuts.

photon events was estimated to be less than one event. To take into account the effect of the choice of the values of α_s and m_c used in the cross section calculation by the Monte Carlo, we scaled this amount by the ratio between the EPJPSI prediction for inelastic J/ψ production and the measured inelastic J/ψ cross section. From this we estimated a negligible contribution from resolved photon events to the total inelastic J/ψ signal for $z_{\text{rec}} > 0.48$.

Events which had 4 tracks were checked to see if they were consistent with originating from an elastically produced ψ' . No such events were found. No attempt was made to separate out the inelastic ψ' contribution because of the large background from the many track combinations. However, the theoretical calculations to which these measurements are compared in Figure 5.15 are scaled by an extra 15% to include the estimated contribution from inelastically produced ψ' .

Monte Carlo events simulating inelastic Bethe-Heitler production of e^+e^- pairs were produced. No contribution to the inelastic J/ψ signal was found.

With the systematic uncertainties from the categories added in quadrature, the total systematic uncertainty for the three regions $z < 0.8, p_t > 1 \text{ GeV}/c$; $z < 0.9, p_t > 1 \text{ GeV}/c$, and $z < 0.9$ are $^{+20\%}_{-17\%}$, $^{+11\%}_{-21\%}$ and $^{+15\%}_{-26\%}$ respectively.

5.4 Cross section

The electroproduction cross section, σ_{ep} , is given by:

$$\sigma_{\text{ep}} = \frac{N_{J/\psi}}{L} \frac{1}{Br} \frac{1}{Acc},$$

where $N_{J/\psi}$ is the number of J/ψ inelastic signal events found, Br is the branching fraction, Acc is the acceptance and L the integrated luminosity. The photon flux is calculated as shown below and the cross section results for the two z ranges $z < 0.8$ and $z < 0.9$, both with $p_t > 1 \text{ GeV}/c$, and for the z range $z < 0.9$ with no p_t requirement are summarized in table 5.3.

The average W of the events was determined by dividing the W region into 5 bins and calculating the acceptance for each bin. The number of events in each bin from

the mass region $2.9 < m_{e^+e^-} < 3.2 \text{ GeV}/c^2$ was corrected by the acceptance and from the resulting distribution the mean W and its error were determined.

5.4.1 Photoproduction Cross section

The photon-proton cross section $\sigma_{\gamma p \rightarrow J/\psi p}(W_{\gamma p})$ can be obtained from the corresponding positron-proton cross section by using the relation:

$$\sigma_{ep}(s) = \int_{y_{\min}}^{y_{\max}} dy \int_{Q_{\min}^2}^{Q_{\max}^2} dQ^2 \cdot \Phi(y, Q^2) \cdot \sigma_{\gamma p}(y, Q^2),$$

where

$$\Phi(y, Q^2) = \frac{\alpha}{2\pi} \frac{1}{Q^2} \left| 1 + (1-y)^2 - \frac{2m_e^2 y^2}{Q^2} \right|$$

is the flux factor for transverse photons [73], $Q_{\min}^2 = m_e^2 \frac{y^2}{1-y}$, $Q_{\max}^2 = 4 \text{ GeV}^2$ and m_e is the mass of the electron. Since the median $Q^2 \sim 10^{-3} \text{ GeV}^2$ is very small, we will neglect the longitudinal contribution and the Q^2 dependence of $\sigma_{\gamma p}$.

The photon-proton cross section is then obtained as the ratio of the measured electron-proton cross-section and the effective photon flux factor $\Phi(y, Q^2)$ integrated over the y and Q^2 ranges covered by the measurement. This procedure assumes that $\sigma_{\gamma p \rightarrow J/\psi p}(W_{\gamma p})$ is independent of y in the limited range relevant for this measurement. The photon flux factor calculated in this manner for $110 < W_{\gamma p} < 160 \text{ GeV}$ is 0.0262.

Although the cross section measurements were made with a lower limit of 0.4 on z , the cross sections were extrapolated to $z > 0$ using the z distribution produced by HERWIG in order to compare with the published theoretical calculations.

$W_{\gamma p}$ range (GeV)	110 - 160		
Average $W_{\gamma p}$ (GeV)	135 ± 4	135 ± 3	135 ± 3
z range	$0.4 < z < 0.8$	$0.4 < z < 0.9$	$0.4 < z < 0.9$
p_t range	$p_t > 1 \text{ GeV}/c$	$p_t > 1 \text{ GeV}/c$	
Acceptance(includes dE/dx)	0.172	0.154	0.154
Number of signal events	22.7 ± 5.1	29.9 ± 6.1	40.8 ± 8.2
Number of inelastic events ¹	22.3 ± 5.1	29.1 ± 6.1	39.5 ± 8.2
Integrated luminosity	2.998 pb ⁻¹		
$J/\psi \rightarrow e^+e^-$ branching ratio	0.0599		
σ_{ep} (nb)	$0.72 \pm 0.16^{+0.14}_{-0.12}$	$1.05 \pm 0.22^{+0.12}_{-0.22}$	$1.42 \pm 0.31^{+0.21}_{-0.37}$
Extrapolation factor to extend lower z limit to 0	1.17	1.12	1.11
σ_{ep} (nb)	$0.84 \pm 0.19^{+0.17}_{-0.14}$	$1.18 \pm 0.25^{+0.13}_{-0.25}$	$1.58 \pm 0.34^{+0.24}_{-0.41}$
Photon flux factor Φ	0.0262		
$\sigma_{\gamma p}$ (nb)	$32.1 \pm 7.3^{+6.4}_{-5.5}$	$40.1 \pm 8.4^{+4.4}_{-6.4}$	$60.5 \pm 13.2^{+9.1}_{-13.7}$

Table 5.3: Calculation of the inelastic J/ψ cross section for three different z and p_t ranges. The first error is statistical; the second is systematic. The uncertainty in $W_{\gamma p}$ is statistical only.

The results of this thesis using the J/ψ electron decay channel are shown in Figure 5.15 along with recent H1 data [74], ZEUS data from $J/\psi \rightarrow \mu^+\mu^-$ decays[75] and the NLO theoretical calculations using the colour singlet model[33]. The H1 data was also taken using the muon channel.

¹ After the statistical subtraction of the contribution from proton dissociation

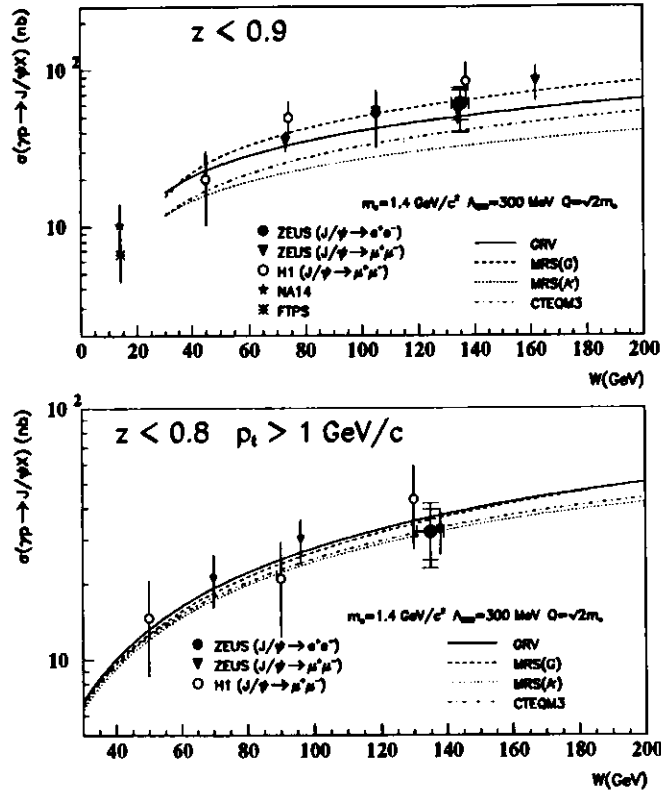


Figure 5.15: Total cross section for inelastic (direct photon) J/ψ production for $z < 0.9$ (upper) and $z < 0.8$, $p_t > 1 \text{ GeV}/c$ (lower). The curves represent NLO pQCD calculations [33] for different parton distributions. They also contain a 15% correction to take into account background from inelastic ψ' production. The inner error bars of the electron data show the statistical errors and the outer error bars also include the systematic uncertainties. The ZEUS muon data [75] show only statistical errors, whereas for the H1 data [74] the error bars represent the combined statistical and systematic errors. Data from lower energy experiments, NA14[30] and FTFS[24] are also shown (error bars represent combined statistical and systematic uncertainties).

Chapter 6

Summary and Outlook

The analyses of 1994 HERA data have presented the first detailed measurements of inelastic J/ψ at high W in photoproduction. With the electron channel we have measured $\sigma_{\gamma p \rightarrow J/\psi X}$ at an average W of 135 GeV to be $60.5 \pm 13.2^{+8.1}_{-15.7} \text{ nb}$ for $z < 0.9$ and $32.1 \pm 7.3^{+6.4}_{-5.5} \text{ nb}$ for the more restrictive region $z < 0.8$, $p_t > 1 \text{ GeV}/c$. The differential distributions are consistent with the events originating through direct photoproduction and are well described by the colour singlet model. These cross section measurements show that the NLO perturbative QCD calculations following the colour singlet model are sufficient to account for the inelastic cross section without the introduction of arbitrary normalization factors. Although this thesis does not include a corrected measurement of $d\sigma/dz$, the good agreement in the uncorrected z distribution between HERWIG and data shown in Figure 5.1 could be taken as evidence that the colour octet terms are not as large as calculated in [35], since the colour octet terms are expected to contribute immensely at high z (See Figure 1.7. This can be attributed to the sizes of the colour octet matrix elements as fitted by [37] being too large. Both H1 and ZEUS, which have had sufficient statistics to measure the corrected differential z cross section using the muon decay channel, have also shown that the data agrees with the NLO calculations and have found no evidence of contributions through colour octet terms.

Although the muon channel was more efficient, mainly due to an increased ac-

ceptance at the FLT, especially for lower values of W , the analysis with the electron data has provided an important independent confirmation of the muon results. The use of the HES would help extend the $|\eta|$ range of the decay tracks and consequently increase the range in W attainable. This has been done in [76][75]. Higher luminosity would allow a more meaningful measurement of the the cross section as a function of z and W and a more precise statement on the size of the colour octet contributions. The z range could be extended and resolved photon production investigated. However, it seems that even with much improved statistics, it will be very difficult to distinguish between the most current structure function parametrizations, at least with inelastic J/ψ production.

Appendix A

Using dE/dx

The application of a selection cut on the dE/dx value of the electron candidate tracks was the single most effective method of separating in an unbiased way true electrons from J/ψ decay from the background of non-electrons, mostly pions. Hence, it was essential to understand the properties of the dE/dx measurement and to ensure that they were as free as possible from systematic effects. Since the electrons seen in the detector were all highly relativistic, they had reached the Fermi plateau, and should have had dE/dx values independent of momentum. A cut on the dE/dx of the electrons fixed at a constant value independent of the momentum of the electron was then feasible and was also simple to implement. In this section we describe how the efficiency of the dE/dx cut was determined. All the dE/dx values of tracks from the data have already been scaled by the pion mean value.

To investigate the efficiency of the dE/dx cut, pure samples of electrons were required. Two samples of electrons were used, elastic $J/\psi \rightarrow e^+e^-$ and photon conversions, $\gamma \rightarrow e^+e^-$. In principle the Monte Carlo simulation could also have been used to study the effects of selecting on dE/dx . However, the quality of the dE/dx measurement in the ZEUS Monte Carlo was superior to what was actually found in the data, as shown in Figure A.1. For this reason and the ready availability of an ample and pure supply of electron tracks, the Monte Carlo simulation was not used to determine the efficiency of the dE/dx selection.

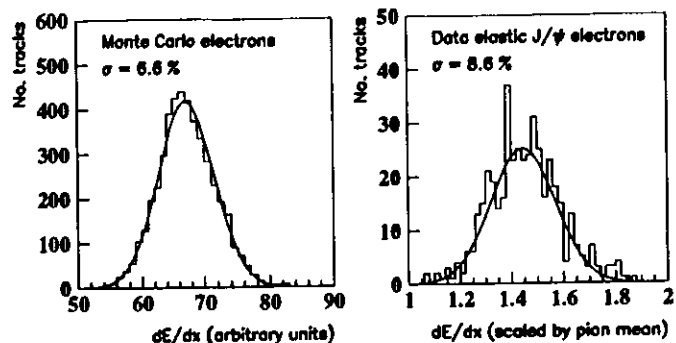


Figure A.1: Comparison of the dE/dx measurement for elastic J/ψ electrons from Monte Carlo (left) and data (right). The selection of the events is described in the text. In addition, only tracks which used at least 30 hits in their truncated mean were used. The resolution was determined by applying a Gaussian fit.

Elastic J/ψ

The elastic J/ψ sample offered the additional advantage that the momentum spectrum of the decay electrons was similar to those from the inelastic J/ψ processes. The signal was very clean because only the two decay electrons were seen in the detector. In addition, most of the background under the signal peak also came from electrons, through the Bethe-Heitler process. If the selection criteria were chosen strictly enough, all the non-electron background could be removed leaving a totally pure sample of electrons.

The elastic $J/\psi \rightarrow e^+e^-$ sample was selected at the FLT by requiring electromagnetic energy in RCAL or BCAL, GOOD track and limiting the amount of energy in the first ring around FCAL. Since the trigger imposed a limit on the energy in the forward region, beam-gas background was naturally suppressed, and a much lower energy threshold could be applied to the electromagnetic energy in RCAL and BCAL. For this reason there were many more events in this elastic sample than the sample shown in Figure 5.4. The track, island and track-matching cuts were done offline in the same manner as the inelastic cuts, except that all the electron island's energy

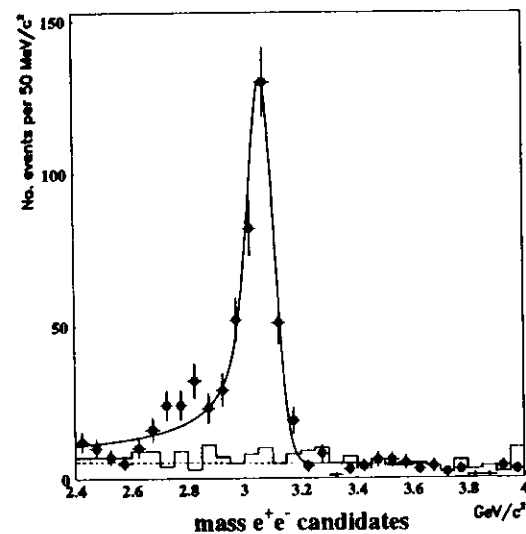


Figure A.2: Mass distribution of an elastic $J/\psi \rightarrow e^+e^-$ sample. The results of a fit using a bremsstrahlung function (see Section 4.4.1) plus a linear background is shown by a solid line; the linear background is illustrated by the dotted line. The histogram shows the estimated contribution from the Bethe-Heitler process which completely accounts for the background.

had to be in the EMC section. To ensure that the events were elastic, the sum of the energy in the CAL aside from the islands matched to the decay electrons had to be less than 1 GeV. Electrons were taken from candidates in a narrow mass region $2.9 < m_{e^+e^-} < 3.2$ GeV/c² to further reduce the possible contamination from pions.

Conversions

Photons from ep interactions occasionally convert to an e^+e^- pair in the walls of the beampipe or tracking detectors. Although these conversion electrons were plentiful, they occurred mostly at low p_t . Tracks from photon conversions were selected by using the PHANTOM routine CONVERT2. Because the photon is massless, the signature of a photon conversion was two oppositely signed tracks which intersected with little or no opening angle. The routine took all pairs of tracks before the vertex fit and extrapolated them to the first pair of points where they were tangent to each other in the $x-y$ plane. If at that point the $x-y$ separation of the two tracks, ΔXY , was less than 0.4 cm and the angular difference, $\Delta\theta$, was less than 0.1 rad, then the quality of the conversion candidate was calculated from the dimensionless quantity, $\text{DISTB} = \sqrt{\left(\frac{\Delta XY}{\sigma(\Delta XY)}\right)^2 + \left(\frac{\Delta\theta}{\sigma(\theta)}\right)^2}$. The values of $\sigma(\Delta XY)$ and $\sigma(\theta)$ were obtained beforehand by fits to the data. DISTB was given a negative sign if the two tracks had the same sign; these track pairs were used to estimate the background from fake conversion pairs.

The following additional constraints were imposed to reduce the number of fake conversions: the z -vertex of the event was within 40 cm of the interaction point; only tracks with stereo layer information were used; the radial distance of the conversion point from the beamline had to be greater than 5 cm; the angle θ between the photon candidate direction and the vector from the event vertex to the conversion point had to satisfy $\cos \theta > 0.98$, and the tracks were not allowed to have hits from the VXD if the conversion point occurred outside the VXD. Figure A.3 shows the distribution of DISTB for conversion candidates.

To calculate the efficiency of a dE/dx cut the background from fake conversion candidates were statistically subtracted from the conversion candidates in the signal

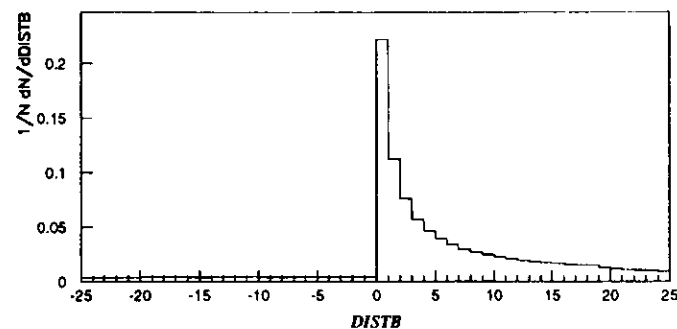


Figure A.3: Distribution of DISTB for conversion candidates.

region $0 < \text{DISTB} < 1$. This region was chosen for its high signal to background ratio. We assumed that the number of same sign fake conversions was the same as the number of opposite sign fake conversions. Since the DISTB distribution was flat for same sign candidates, all the candidates with $-20 < \text{DISTB} < 0$ were used to as an estimate of the background, after being scaled by 1/20. The dE/dx distributions for the signal and background conversion candidate regions are shown in Figure A.5. To find the average efficiency, f_e , of the dE/dx cut on electrons, we calculated instead a background corrected efficiency, f ,

$$f = \frac{N_{\text{pass}}^{\text{sig}} - N_{\text{pass}}^{\text{bg}}}{N^{\text{sig}} - N^{\text{bg}}},$$

where N^{sig} and N^{bg} were the number of tracks in the signal and background regions and $N_{\text{pass}}^{\text{sig}}$, $N_{\text{pass}}^{\text{bg}}$ were the number of those tracks passing the dE/dx cut. By explicitly separating the tracks in the signal region into electrons and hadrons and assuming all the tracks in the background region to be hadrons, this calculated efficiency could then be expressed in terms of the actual efficiencies for electrons and hadrons through

$$f = \frac{f_e N_e^{\text{sig}} + f_{\text{had}} (N_{\text{had}}^{\text{sig}} - N_{\text{had}}^{\text{bg}})}{N_e^{\text{sig}} + N_{\text{had}}^{\text{sig}} - N_{\text{had}}^{\text{bg}}},$$

where N_e^{sig} was the number of electrons in the signal region; $N_{\text{had}}^{\text{sig}}$ and $N_{\text{had}}^{\text{bg}}$ were the number of hadrons in the signal and background regions, and f_{had} was the average

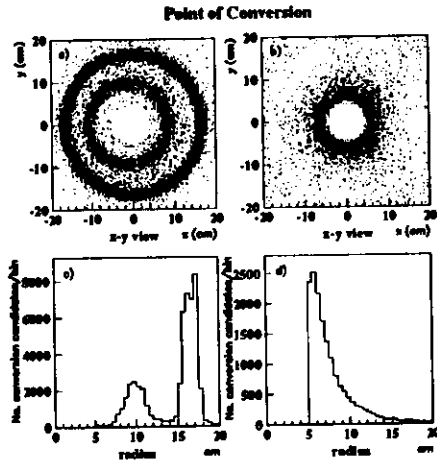


Figure A.4: Point of conversion in the x-y plane for candidates with a) $0 < DISTB < 1$ and b) $-25 < DISTB < 0$. The offset of the VXD with respect to the beamline can clearly be seen. The photons convert primarily in the walls of the beampipe (inner ring) and the CTD (outer ring). Radial distance from the origin of the points of conversion for candidates with c) $0 < DISTB < 1$ and d) $-25 < DISTB < 0$.

efficiency for the dE/dx cut for hadrons. If we had scaled the background correctly such that $N_{had}^{sig} = N_{had}^{bg}$ is correct, then the above equation reduces to $f = f_e$.

conversion electrons

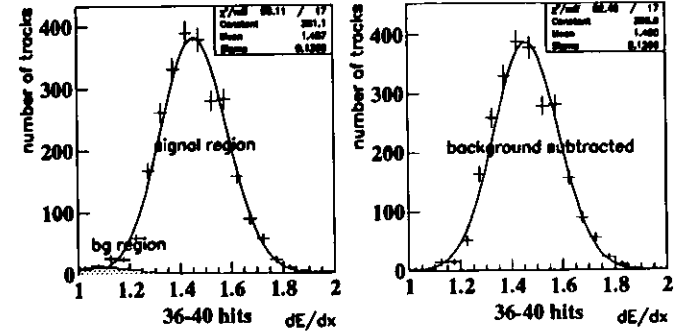


Figure A.5: The dE/dx distribution for tracks from conversion electrons candidates with $p_t > 0.8$ GeV/c and having between 36 and 40 hits used in the truncated mean. The left plot shows the distributions for the signal region $0 < DISTB < 1$ (unfilled histogram) and background region $-20 < DISTB < 0$, scaled by $1/20$ (filled histogram). The right plot shows the result after the background has been subtracted from the signal distribution. A Gaussian fit is overlaid in both plots.

Properties of dE/dx

As mentioned in Section 2.5.1, the raw pulse heights were corrected for the track path length and the wire gains. In order to use a cut in dE/dx fixed at a constant value to select electrons, it was important to first ensure that reconstructed dE/dx measurement was truly independent of angle and momentum. Figure A.6 shows that was not the case with the initial reconstruction of dE/dx .

The dE/dx distribution as a function of track angle exhibited two features. First, there was a symmetric dip in the central region, with the largest effect occurring at 90 degrees. Secondly, the dE/dx values rose rapidly for low angle tracks as the tracks got closer to the beam line.

The first phenomenon can be explained by space charge effects. When a track travels nearly perpendicularly to a sense wire, the charge is collected in a small region

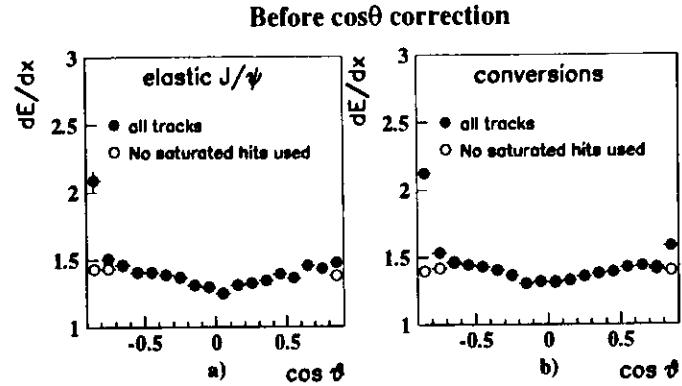


Figure A.6: Mean dE/dx versus polar track angle for electrons from a) the elastic J/ψ sample and b) the conversion sample. The solid circles are for tracks with no restriction on the number of saturated hits. The open circles are for tracks with no saturated hits used in the calculation of the truncated mean.

along the wire. The concentration of avalanche electrons around the wire screens the wire, reducing the electric field which electrons further out experience, and this results in an overall decrease in the amount of charge collected.

A simple correction was made by fitting the mean dE/dx versus $|\cos\theta|$ with a linear function in the range $|\cos\theta| < 0.65$, where the dip was evident. Both the distribution and the result of the fit are shown in Figure A.7. The correction function, which was applied only when $|\cos\theta| < 0.65$, was

$$dE/dx(\text{corrected}) = dE/dx(\text{original}) \times (a_0 + (0.65)a_1)/(a_0 + a_1 |\cos\theta|),$$

where the fit results gave $a_0 = 1.26$ and $a_1 = 0.29$.

The second feature was a result of the treatment of saturated hits in the truncated mean. In general, once a pulse hit is saturated, i.e., the amount of charge collected by the FADC is greater than its dynamic range, the corrected pulse size cannot be found. No correction was done. Since the raw pulse size increased for tracks at angles close to the beam line due to the extra path length traveled in a single cell, tracks at low angles were more likely to have saturated hits. Once a track had over 30%

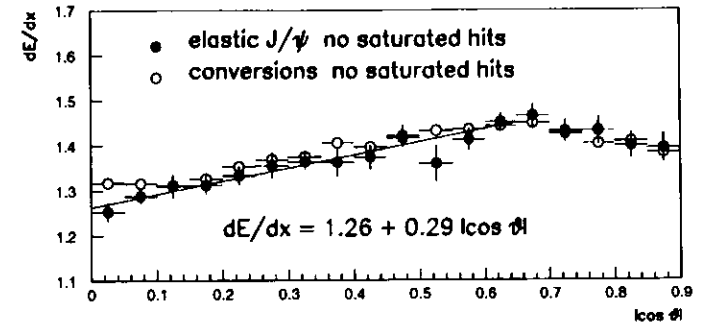


Figure A.7: Fit to the mean dE/dx as a function of $|\cos\theta|$. Only tracks which used no saturated hits in determining the truncated mean are included. The fit was applied to the elastic J/ψ data points.

saturated hits, the truncated mean algorithm included by default the excess saturated hits in the calculation, leading to the increased dE/dx value. The dE/dx values of the tracks in this analysis were not corrected for the inclusion of saturated hits in the truncated mean. However, the $|\eta| < 1.5$ cut restricted the tracks to a region where they had few saturated hits. Since the cut used in the inelastic J/ψ selection of 1.25 times the mean pion value led to a very high efficiency (see Figure 5.11), the possible presence of saturated hits would increase the efficiency by only a small amount. The ability of the dE/dx cut to reject pions faking electrons did suffer at low angles due to the saturated hits, but as can be seen in the final mass plots of Section 4.4.2, the background was well under control.

The conversion sample was used to check the properties of the dE/dx measurements in the data. As seen in Figure A.9, the mean detected energy loss remained for the most part constant around the value 1.45, independent of momentum or number of hits used in the truncated mean. Although there was a small rise for tracks with low momentum or with only a few hits, these tracks were excluded in the analysis by the selection cuts on p_t and η . The resolution of the dE/dx measurements as a

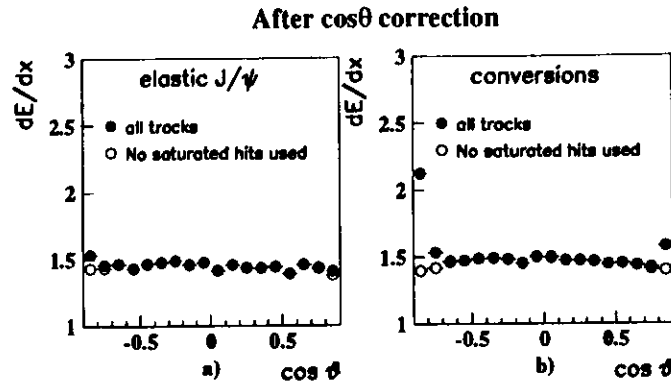


Figure A.8: Mean dE/dx after correction versus polar angle for electrons from a) elastic J/ψ and b) conversion candidates. The solid circles are for tracks with no restriction on the number of saturated hits. The open circles are for tracks with no saturated hits used in the calculation of the truncated mean.

function of N_t , the number of hits used in the truncated mean was determined by a fit to be $\sigma(dE/dx)/(dE/dx) = \sqrt{(0.36)^2/N_t + (0.07)^2}$.

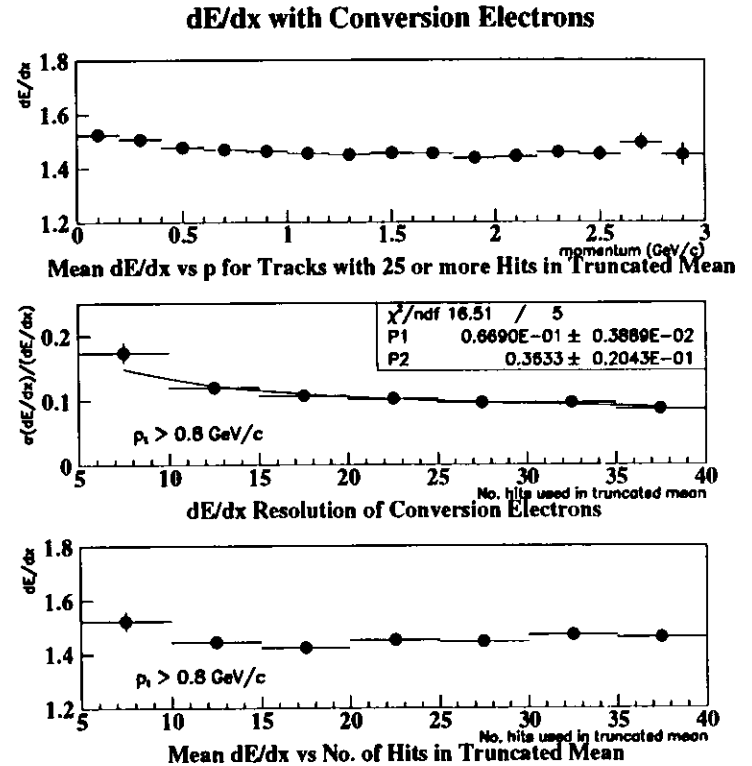


Figure A.9: Properties of conversion electrons.

Appendix B

Glossary

BCAL Barrel calorimeter

bremstrahlung Radiation of photons by accelerated charge particles

CFLT Calorimeter first level trigger

colour singlet model Model of quarkonium production where the spin and colour of the quark-antiquark pair from the hard interaction is constrained to match the spin and colour (i.e. no net colour) of the final state quarkonium

conversion The process whereby a photon converts into a e^+e^- pair in the presence of matter

CTD Central tracking detector

CZAR Simulation of the ZEUS trigger (FLT, SLT and TLT)

dE/dx Rate of energy loss (mostly ionization) of charged particles through matter. The amount is sensitive to the velocity of the particle, hence it can be used to identify the mass of the particle if the momentum is known.

EMC Electromagnetic section of the calorimeter

EPJPSI Monte Carlo event generator used to simulate inelastic J/ψ photoproduction and resolved photoproduction

EPSOFT Monte Carlo event generator used to simulate proton dissociative J/ψ production

η Pseudo-rapidity. It is defined as $-\ln(\tan\theta/2)$ where θ is the polar angle.

FCAL Forward calorimeter

FLT First level trigger

HERA ep collider at DESY, Hamburg

HERWIG Monte Carlo event generator used to simulate inelastic J/ψ production

island A group of contiguous calorimeter cells containing (one hopes) the energy deposition of a single particle

MC Monte Carlo (see below)

Monte Carlo Programs which simulate physics processes (i.e. electron-proton collisions) and (perhaps) the resultant response in the ZEUS detector through the use of random numbers and probability distributions.

MOZART Monte Carlo simulation of the ZEUS detector

proton dissociation A "soft" physics process where the proton is excited to a higher mass state through the exchange of a colourless object such as the pomeron

PMT Photomultiplier tube

QCD Quantum Chromodynamics: the theory of the strong interaction

QED Quantum Electrodynamics: the theory of the electromagnetic interaction

RCAL Rear calorimeter

resolved photoproduction Processes where the photon exhibits a partonic structure. One of the partons enters the hard interaction; the rest form a photon remnant which is sprayed into the rear section of detector.

RHES Rear hadron electron separator

SLT Second level trigger

SRTD Small angle rear track detector

TLT Third level trigger

VCTPAR Table of tracks which are associated with the event vertex

W Centre of mass of the γp system

z Inelasticity of the J/ψ : $z = P_p \cdot k_\psi / P_p \cdot k$,

Bibliography

- [1] S. Weinberg; *Phys. Rev. Lett.* **19**, 1264 (1967)
- [2] See for example F. Halzen and A. Martin; *Quarks & Leptons*; John Wiley & Sons (1984)
- [3] T. Sloan, G. Smadja, R. Voss; *Phys. Rep.* **162**, 45 (1988)
- [4] M. Glück, E. Reya and A. Vogt; *Z. Phys.* **C67**, 433 (1995)
- [5] A.D. Martin, R.G. Roberts and W.J. Stirling; *Phys. Lett.* **B306**, 145 (1993) and Erratum-ibid. **B309**, 492 (1993)
- [6] A.D. Martin, R.G. Roberts and W.J. Stirling; *Phys. Lett.* **B354**, 155 (1995)
- [7] CTEQ Collaboration, J. Botts et al.; *Phys. Lett.* **B304**, 159 (1993)
CTEQ Collaboration; MSUHEP-60426, CTEQ-604
- [8] E.D. Bloom et al.; *Phys. Rev. Lett.* **23**, 930 (1969)
- [9] J.J. Aubert et al.; *Phys. Rev. Lett.* **33**, 1404 (1974)
- [10] J.-E. Augustin et al.; *Phys. Rev. Lett.* **33**, 1406 (1974)
- [11] C. Bacci et al.; *Phys. Rev. Lett.* **33**, 1408 (1974)
- [12] J.D. Bjorken and S. Glashow; *Phys. Lett.* **11**, 255 (1964)
S. Glashow, J. Iliopoulos and L. Maiani; *Phys. Rev.* **D2**, 1285 (1970)
- [13] For a review of quarkonium production see G.A. Schuler; CERN-TH-7170/94, HEP-PH-9403387
- [14] A.D. Martin, C.K. Ng, W.J. Stirling; *Phys. Lett.* **B191**, 200 (1987)
- [15] H. Jung, G. A. Schuler and J. Terron; Proceedings of the workshop on physics at HERA, Hamburg, Oct. 1991, Eds. W. Buchmüller and G. Ingelman
- [16] M. Cacciari and M. Krämer; Proceedings of the workshop on future physics at HERA, Hamburg, Sept. 1996, Eds. G. Ingelman, A. De Roeck, R. Klanner
- [17] For a review see T.H. Bauer et al.; *Rev. Mod. Phys.* **50**, 261 (1978)

- [18] For a review see S. D. Holmes, W. Lee and J.E. Wiss; *Ann. Rev. Nucl. Part. Sci.* **35**, 397 (1985)
- [19] M. G. Ryskin; *Z. Phys.* **C37**, 89 (1993)
- [20] S.J. Brodsky et al.; *Phys. Rev.* **D50**, 3134 (1994)
- [21] M. G. Ryskin, R.G. Roberts, A. D. Martin and E. M. Levin; HEP-PH/9511228 (1996)
- [22] ZEUS Collaboration; *Phys. Lett.* **B350**, 120 (1995)
ZEUS and H1 collaborations; preliminary '94 data presented at the Durham workshop on HERA Physics, Sept. 1995, to be published.
- [23] E401 Collaboration, M. Binkley et al.; *Phys. Rev. Lett.* **48**, 73 (1982)
- [24] B.H. Denby et al.; *Phys. Rev. Lett.* **52**, 795 (1984)
- [25] H. Fritzsche; *Phys. Lett.* **B67**, 217 (1977)
- [26] R. Gavai et al.; *Int. J. Mod. Phys.* **A10**, 3043 (1995)
- [27] E.L. Berger and D. Jones; *Phys. Rev.* **D23**, 1521 (1981)
R. Baier and R. Rückl; *Phys. Lett.* **B102**, 364 (1981)
- [28] R. Barbieri, R. Gatto and E. Remiddi; *Phys. Lett.* **B106**, 497 (1981)
- [29] G.T. Bodwin, E. Braaten and G.P. Lepage; *Phys. Rev.* **D51**, 1125 (1995)
- [30] NA-14 Collaboration, R. Barate et al.; *Z. Phys.* **C33**, 505 (1987)
- [31] New Muon Collaboration, D. Allasia et al.; *Phys. Lett.* **B258**, 493 (1991)
- [32] European Muon Collaboration, J. Ashman et al.; *Z. Phys.* **C56**, 21 (1992)
- [33] M. Krämer; *Nucl. Phys.* **B459**, 3 (1996)
- [34] H. Jung, D. Krücker, C. Greub and D. Wyler; *Z. Phys.* **C60**, 721 (1993)
- [35] M. Cacciari and M. Krämer; *Phys. Rev. Lett.* **76**, 4128 (1996)
- [36] P. Ko, J. Lee and H.S. Song; *Phys. Rev.* **D54**, 4312 (1996)
- [37] P. Cho and A.K. Leibovich; *Phys. Rev.* **D53**, 150 (1996)
- [38] CDF Collaboration, F. Abe et al.; *Phys. Rev. Lett.* **69**, 3702 (1992), *Phys. Rev. Lett.* **71**, 2537 (1993)
- [39] W.E. Casell and G.P. Lepage; *Phys. Lett.* **B167**, 437 (1986)
- [40] W. Buchmüller and S.-H. H. Tye; *Phys. Rev.* **D24**, 132 (1981)

- [41] CDF Collaboration, F. Abe et al.; "J/ψ and ψ' Production at CDF" FERMILAB-Conf-96/156-E, in *28th International Conference on High Energy Physics (ICHEP96)*, Warsaw (1996)
- [42] ZEUS Collaboration; The ZEUS Detector, Status Report 1993 (1993)
- [43] C. Alvisi et al.; *Nucl. Instr. and Meth.* **A305**, 30 (1991)
- [44] ZEUS Collaboration, B. Foster et al.; *Nucl. Instr. and Meth.* **A338**, 254 (1994)
- [45] For a review on calorimetry see: R. Wigmans; *Ann. Rev. Nucl. Part. Sci.*, **41** (1991)
- [46] ZEUS Collaboration; *Nucl. Instr. and Meth.* **A309**, 101, (1991)
- [47] M. Derrick et al.; *Nucl. Instr. and Meth.* **A309**, 77 (1991)
- [48] G. Abbiendi et al.; *Nucl. Instr. and Meth.* **A333**, 342 (1993)
- [49] H. Bethe and W. Heitler; *Proc. Roy. Soc.* **A146**, 83 (1934)
- [50] G.F. Hartner et al.; ZEUS-Note 95-004 (1995)
- [51] Particle Data Group; *Phys. Rev.* **D50**, 1251 (1994)
- [52] D.H. Perkins; *Introduction to High Energy Physics*; Addison-Wesley (1987)
- [53] T. Doeker, A. Frey and M. Nakao; ZEUS-Note 94-123 (1994)
- [54] L.A.T. Bauerdick et al.; "The Physics Analysis Environment of the ZEUS Experiment", in *Proceedings of CHEP '95 Conference* (1995), DESY 95-236 (1995)
L.A.T. Bauerdick et al.; "ZARAH - The Central Computing Facility for the ZEUS Experiment", in *Proceedings of CHEP '95 Conference* (1995)
- [55] G. Altarelli and G. Parisi; *Nucl. Phys.* **B126**, 298 (1977)
- [56] T. Sjöstrand; *Comp. Phys. Commun.* **82**, 74 (1994)
- [57] G. Marchesini et al.; *Comp. Phys. Comm.* **67**, 465 (1992)
- [58] H. Jung; Proceedings of the workshop on physics at HERA, Hamburg, Oct. 1991, Eds. W. Buchmüller and G. Ingelman
- [59] M. Kasprzak; ZEUS-Note 95-069 (1995)
- [60] M. Glück, E. Reya and A. Vogt; *Phys. Rev.* **D45**, 3986 (1992)
- [61] CDF Collaboration, F. Abe et al.; *Phys. Rev.* **D50**, 5535 (1994),
- [62] GEANT - Detector Description and Simulation Tool; CERN W5013

- [63] B. Burow; "Funnel: Towards Comfortable Event Processing", in *Proceedings of CHEP '95 Conference* (1995)
- [64] W.H. Smith et al.; *Nucl. Instr. and Meth. A* **355**, 278 (1995)
S. Silverstein et al.; *Nucl. Instr. and Meth. A* **360**, 322 (1995)
- [65] F. Wilson; ZEUS-Note 95-002 (1995)
- [66] D. Bandyopadhyay; ZEUS-Note 93-013 (1993)
- [67] F. Jacquet and A. Blondel; DESY 79-48, 391 (1979)
- [68] A. Mass; PhD thesis: *Nachweis von J/ψ -Mesonen mit Hilfe neuronaler Netze in Photoproduktionsereignissen an HERA*, Bonn University (1995)
- [69] MINUIT - Function Minimization and Error Analysis; CERN D506
- [70] ZEUS Collaboration; Measurement of Elastic J/ψ Photoproduction at HERA, to be published (1997)
- [71] K. Piotrkowski, M. Zachara; ZEUS-Note 95-138 (1995)
- [72] M. Arneodo, L. Lamberti and M. Ryskin; DESY-96-149, HEP-PH/9610286 (1996)
- [73] V. M. Budnev et al.; *Phys. Rep.* **C15**, 181 (1975)
- [74] H1 Collaboration, S. Aid et al.; *Nucl. Phys.* **B472**, 3 (1996)
- [75] ZEUS Collaboration; publication in preparation (1997)
- [76] K. Homma; PhD thesis, Tokyo Metropolitan University (1997)